AEDC-TR-88-32

C #2

PARC Code Validation for Propulsion Flows

G. K. Cooper, G. D. Garrard, and W. J. Phares
Sverdrup Technology, Inc.

January 1989

Final Report for Period October 1, 1987 – September 30, 1988

Approved for public release; distribution is unlimited.

ARNOLD ENGINEERING DEVELOPMENT CENTER
ARNOLD AIR FORCE BASE, TENNESSEE
AIR FORCE SYSTEMS COMMAND
UNITED STATES AIR FORCE

NOTICES

When U. S. Government drawings, specifications, or other data are used for any purpose other than a definitely related Government procurement operation, the Government thereby incurs no responsibility nor any obligation whatsoever, and the fact that the Government may have formulated, furnished, or in any way supplied the said drawings, specifications, or other data, is not to be regarded by implication or otherwise, or in any manner licensing the holder or any other person or corporation, or conveying any rights or permission to manufacture, use, or sell any patented invention that may in any way be related thereto.

Qualified users may obtain copies of this report from the Defense Technical Information Center.

References to named commercial products in this report are not to be considered in any sense as an endorsement of the product by the United States Air Force or the Government.

DESTRUCTION NOTICE

For classified documents, follow the procedures in DoD 5220.22-M, Industrial Security Manual, Section II-19 or DoD 5200.1-R, Information Security Program Regulation, Chapter IX. For unclassified, limited documents, destroy by any method that will prevent disclosure or reconstruction of the document.

APPROVAL STATEMENT

This report has been reviewed and approved.

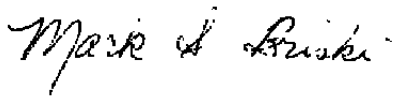

MARK S. BRISKI, Capt, USAF
Chief, Aeromechanics Branch
Facility Technology Division
Directorate of Technology
Deputy for Operations

Approved for publication:

FOR THE COMMANDER

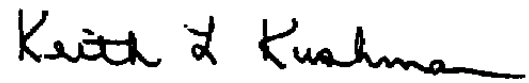

KEITH L. KUSHMAN
Technical Director
Directorate of Technology
Deputy for Operations

UNCLASSIFIED

SECURITY CLASSIFICATION OF THIS PAGE

REPORT DOCUMENTATION PAGE

Form Approved OMB No 0704-0188

1a REPORT SECURITY CLASSIFICATION UNCLASSIFIED	1b RESTRICTIVE MARKINGS
2a. SECURITY CLASSIFICATION AUTHORITY	3. DISTRIBUTION/AVAILABILITY OF REPORT Approved for public release; distribution is unlimited.
2b. DECLASSIFICATION/DOWNGRADING SCHEDULE	
4. PERFORMING ORGANIZATION REPORT NUMBER(S) AEDC-TR-88-32	5. MONITORING ORGANIZATION REPORT NUMBER(S)
6a. NAME OF PERFORMING ORGANIZATION Arnold Engineering Development Center 6b. OFFICE SYMBOL (If applicable) DOT	7a. NAME OF MONITORING ORGANIZATION
6c. ADDRESS (City, State, and ZIP Code) Air Force Systems Command Arnold Air Force Base, TN 37389-5000	7b ADDRESS (City, State, and ZIP Code)
8a. NAME OF FUNDING/SPONSORING ORGANIZATION Arnold Engineering Development Center 8b. OFFICE SYMBOL (If applicable) DO	9 PROCUREMENT INSTRUMENT IDENTIFICATION NUMBER
8c. ADDRESS (City, State, and ZIP Code) Air Force Systems Command Arnold Air Force Base, TN 37389-5000	10 SOURCE OF FUNDING NUMBERS PROGRAM ELEMENT NO. 65807F; PROJECT NO.; TASK NO; WORK UNIT ACCESSION NO
11. TITLE (Include Security Classification) PARC Code Validation for Propulsion Flows	
12. PERSONAL AUTHOR(S) Cooper, G. K., Garrard, G. D., Phares, W. J., Sverdrup Technology, Inc., AEDC Group	
13a. TYPE OF REPORT Final 13b. TIME COVERED FROM 10/1/87 TO 9/30/88	14. DATE OF REPORT (Year, Month, Day) January 1989 15. PAGE COUNT 118
16. SUPPLEMENTARY NOTATION Available in Defense Technical Information Center (DTIC).	

17. COSATI CODES			18 SUBJECT TERMS (Continue on reverse if necessary and identify by block number)
FIELD	GROUP	SUB-GROUP	Navier-Stokes code, free jet, program validation, backstep, flat-plate flow
12	01		
09	02		

19. ABSTRACT (Continue on reverse if necessary and identify by block number)

Validation/calibration of the PARC Navier-Stokes computer program for flows typical of turbine engine and rocket motor testing at the Arnold Engineering Development Center has been performed for a number of fundamental test cases. Laminar and turbulent flow simulations for a flat plate with zero pressure gradient have been compared with solutions of the boundary-layer equations with good-to-excellent results. These test cases examined effects of grid spacing in both the streamwise and cross-stream directions, compressibility, and heat transfer. The laminar flow simulations with a new artificial viscosity model were in excellent agreement with the boundary-layer code results; the turbulent simulations with a Baldwin- and Lomax-style turbulence model compared less favorably with some cases showing a 10-percent error in skin friction. The near wake of turbulent supersonic jet was also simulated and compared very well with experimental data. Results for the far wake for the same test case were poor, since the turbulence model failed to allow for the differences in near- and far-wake flows. The low-supersonic Stanford (Cont)

20. DISTRIBUTION/AVAILABILITY OF ABSTRACT ☐ UNCLASSIFIED/UNLIMITED ☒ SAME AS RPT ☐ DTIC USERS	21. ABSTRACT SECURITY CLASSIFICATION UNCLASSIFIED
22a. NAME OF RESPONSIBLE INDIVIDUAL C. L. Garner	22b TELEPHONE (Include Area Code) (615) 454-7813 22c. OFFICE SYMBOL DOCS

DD Form 1473, JUN 86 *Previous editions are obsolete.* SECURITY CLASSIFICATION OF THIS PAGE

UNCLASSIFIED

19. ABSTRACT (Concluded)

backstep flow was also simulated for the case with heat transfer. Although the reattachment length was well predicted, and redevelopment of the flow downstream of attachment compared favorably with the experimental data, the flow in the recirculation zone showed the familiar defects of algebraic turbulence models that are not optimized to this flow. Overall, the performance of the PARC code was such that would lend confidence to its usage in propulsion flow simulations.

PREFACE

The work reported herein was conducted by the Arnold Engineering Development Center (AEDC), Air Force Systems Command (AFSC). The results of the research were obtained by Sverdrup Technology, Inc., AEDC Group, operating contractor for the engine test facilities at the AEDC, AFSC, Arnold Air Force Base, Tennessee, under Project DB84EW. The Air Force Project Manager was Capt. Mark Briski/DOT. The data analysis was completed on July 31, 1988, and the manuscript was submitted for publication on November 10, 1988.

TABLE OF CONTENTS

ILLUSTRATIONS

Figure Page

TABLES

Table Page

APPENDIXES

1.0 INTRODUCTION

As with other types of aerospace engineering, turbine and rocket testing requirements are making enormous demands on computational fluid dynamics (CFD) as a means to reduce the cost and risks involved in propulsion system testing. Within the Engine Test Facility (ETF) at the Arnold Engineering Development Center (AEDC), a general purpose CFD tool, the PARC code, which is at least qualitatively applicable to the bulk of propulsion system testing problems, has begun to fill that need. Detailed aerodynamic simulations produced by the PARC code, an Euler/Navier-Stokes code, have assisted in the solution of a variety of the propulsion testing problems encountered at the AEDC, including thrust-reverser-collector design, inlet/free-jet feasibility studies and rocket diffuser performance analysis. However, it has often been necessary to provide code validation (calibration of the PARC code to the type of flow being simulated) concurrently with the application. Because of schedule and cost constraints, much of this calibration has been of a qualitative nature. Quantitative prior validation of the PARC code will be required if this technology is to provide timely and cost-effective assistance in the solution of anticipated testing problems in the ETF's turbine and rocket testing programs.

The overall objective of this effort is to establish the level of confidence that can be placed in PARC code simulations of typical engine testing problems. Before the PARC code can be used with a high degree of confidence, a systematic and comprehensive assessment of the PARC code's ability to accurately simulate basic fluid dynamic phenomena must be established. Also, since the entire CFD technology base is still rapidly developing, the PARC code is continuously evolving and changing; a means for economical and timely revalidation of new versions of this code must be developed. Thus, the approach was divided into three phases, (1) assemble a set of good test cases representative of the fluid dynamics problems encountered in engine testing and incorporate them into a permanent CFD code validation system; (2) assess the validity of PARC code simulations for basic fluid flows possessing features encountered in most engine test problems; and (3) calibrate the PARC code to generic classes of turbine engine and rocket motor testing applications.

At this point in this effort, the PARC code has been validated for the following fundamental flow cases: (1) flat plate with no pressure gradients, (2) a matched expansion supersonic free-jet wake, and (3) very low subsonic flow over a backstep. These cases will be revisited as new models or modifications are integrated into the PARC code. In the near future, in addition to expanding on these cases, appropriate data sets will be assembled and contrasted with the PARC code solutions for the following cases: (1) nozzles, (2) propulsion system test diffusers, and (3) nozzle/exhaust/diffuser/test cell interactions. They will be documented in a subsequent report. Results for laminar and turbulent flat-plate flow cases will be presented in Section 2.0. Section 3.0 documents results for the supersonic free-jet

wake with turbulent mixing. Section 4.0 compares the PARC code results with experimental data for a flow over a backstep.

2.0 FLAT PLATE

2.1 MOTIVATION

Most ETF propulsion test problems are viscous by nature and involve the development of wakes and boundary layers. Flat-plate flows are simple in nature, yet possess all the fundamental physics of more general boundary-layer flows. The physics of the flat-plate flow has been extensively studied over many decades and is felt to be well understood. Thus, the flat plate makes an ideal test case for determining the fundamental validity of the PARC code's viscous simulations.

2.2 TEST CASES

Pertinent parameters from the 17 flat-plate test cases that were used in this study are shown in Tables 1 and 2. The flat-plate test matrix for laminar flows are presented in Table 1, and the test matrix for turbulent flows are presented in Table 2. Free-stream properties and grid characteristics, such as Mach number, inflow and outflow Reynolds numbers (based on axial distance from the plate's leading edge), plate-wall thermal boundary conditions, and grid packing in both the normal and tangential directions are outlined in the tables.

All of the grids were constructed by the same technique that produced nearly orthogonal grid lines with one set approximately parallel to the plate and the other set normal to it. The grid lines were stretched from the plate surface and were uniformly spaced in the streamwise direction. A compressible Blasius coordinate transformation was done on the coordinate running away from the plate (Fig. 1); all grid characteristics are given in terms of this transformed coordinate (eta). Wall-conforming grid properties shown in the tables are initial spacing (Deta), stretching factor (alpha), maximum eta (value of eta on furthest grid line from the plate), approximate number of points in boundary layer, and total number of points in cross-flow direction. Streamwise grid properties are step-size Dx (constant), and total number of points in streamwise direction. Note that all lengths have been nondimensionalized by the total plate length.

A study of grid spacing effects was an important part of this effort. In particular the following cases were examined:

Cross-Stream Grid Spacing

1. Dense (Cases 4 and 12)—These cases were intended to give the PARC algorithm its best chance at providing accurate simulations. This grid density and degree of stretching is typical of that used in many boundary-layer codes.

2. Moderate (Cases 1 through 3 and 9 through 11)—These cases are typical of current, recommended PARC usage for two-dimensional (2-D) and axisymmetric simulations.

3. Sparse (Cases 5 and 13)—These cases were used to test the limits of the PARC code for the less-than-adequate grid distributions typical of those encountered in practice for some complex 2-D and axisymmetric simulations and most three-dimensional (3-D) simulations.

Streamwise Spacing

1. Fine (Cases 1 and 9)—Analogous with the dense cases discussed before, this griding was intended to get the best possible results, even though this spacing is typically too fine to be used in actual applications.

2. Sparse (Cases 2 and 10)—Intended to be the primary streamwise griding option, these cases are typical of practical PARC code usage for 2-D and axisymmetric simulations.

3. Coarse (Cases 3 and 11)—These cases were used to determine the error introduced by current griding practices in complex problems (especially 3-D applications).

It is of particular interest to study the heat-transfer capabilities of the PARC code for laminar and turbulent flows. Cases were limited to either constant wall temperature or adiabatic conditions. These conditions were to be representative of those encountered in propulsion system testing. All cases were treated with wall adiabatic conditions except Cases 6, 14, and 15.

For this investigation, the Mach numbers were high enough to avoid convergence problems and low enough to avoid the dissociative effects of hypersonic flow. Cases 1 through 6 and 9 through 15 were conducted with a transonic Mach number of 0.75, which is typically encountered in some region of most engine testing flows. Mach number variations were investigated in Cases 7 and 16 (Mach number of 0.1), and Cases 8 and 17 (Mach number of 2.5). Although very much of interest, pressure gradients were not investigated because of schedule limitations.

For convenience, a validated boundary-layer computer code, based on the Falkner-Skan equations (Refs. 1 and 2), was used for comparison with PARC code computations. The quality of data from the boundary-layer code was determined by comparison with data from an integral boundary-layer code (Ref. 3) and experimental data. Comparison between the codes for surface heat transfer, displacement thickness, and boundary-layer velocity and temperature profiles are in good agreement.

The inlet-plane flow conditions were obtained from the boundary-layer code and were fixed at a plate length of X/L = 0.25 for the laminar flow cases (1 through 8) and at X/L = 0.5 for the turbulent flow cases (9 through 17). This provided initial flow conditions well downstream of any leading edge effects. Selection of the plate lengths were based on anticipated boundary-layer growth (doubling of the boundary-layer thickness was allowed for).

2.3 RESULTS

Overall comparisons between the boundary-layer code validation data and the PARC code were good to excellent for the flat-plate cases. During the course of this effort, a new artificial viscosity model and a new algebraic turbulence model were incorporated into the PARC code; the older version of the PARC code did not produce as good results with the comparisons ranging from poor to excellent, depending on the nature of the flow. Appendixes A and B sketch out the basic formulation of these new features of the PARC code.

2.3.1 Laminar Cases

As would be expected, the PARC code simulations of the laminar flow cases (Table 1, Cases 1 through 8) compared very well with the boundary-layer code results. Even the old version of the code with the original artificial dissipation model did very well, except for skin friction on the transonic case. Surprisingly enough, even the coarsest grid cases (3 and 5) produced comparisons little different from the finest grid cases (1 and 4). The plots of PARC code solution versus boundary-layer code solution for Case 2 (Fig. 2) are typical of all the results; (1) velocity profiles match to plotting accuracy; (2) temperature profiles are nearly as good with very minor deviations; (3) shape factors (H) and skin friction (Cf) display the same trends, but are slightly offset (0.1 to 1.0 percent) because of an adverse interaction of the PARC code calculations with the inflow conditions.

2.3.1.1 Grid Spacing Results

The three streamwise grid variation cases (1, 2, and 3) produced results that were so nearly identical with each other that only the comparisons for Case 2 are presented (Fig. 2). This result is as good as could have been hoped for, since even the coarsest spacing (Case 3) is

finer than would be feasible for most 3-D simulations of any complexity. More differences showed up with cross-stream variations in the grid (Cases 2, 4, and 5), but were still rather minor. There were no discernible differences in the velocity profiles and hardly noticeable deviations in the temperature profiles. This can be clearly seen in Fig. 3 where the PARC solutions for these three cases are contrasted. The important thing to note from these results is that (1) even for the coarsest grid (*only 12 points in the boundary layer*) the largest error is on the order of 1 percent in shape factor and much less for all other quantities examined; (2) the error introduced at the inflow boundary is progressively reduced with increasing grid density across the boundary layer and not noticeably reduced with increasing density in the streamwise direction.

2.3.1.2 Thermal Property Results

The cooled wall Test Case 6, with a constant wall temperature one-half of the free-stream static temperature, demonstrated the PARC codes heat-transfer capability for laminar flows. As can be seen from an examination of Fig. 4, good comparisons with the boundary-layer code were obtained on all parameters including Stanton number (St), with the largest deviation being on the order of 1 percent. This error can again be largely attributed to the previously noted problem with the inflow boundary.

2.3.1.3 Mach Number Variation Results

The subsonic Test Case 7 results (Fig. 5) are as good as, if not better than, the comparable transonic Case 3, with the maximum error again occurring in shape factor (approximately 0.1 percent). Comparisons for the supersonic Test Case 8 (Fig. 6) are not quite as good as the comparable transonic Case 3 (nearly a 5-percent error in shape factor). This disagreement is thought to be caused by the creation of a weak oblique shock from the disturbance caused by the ubiquitous inflow boundary error.

2.3.1.4 Code Improvements Results

One of the two important improvements to the PARC code to be investigated as part of this effort was the enhancement of the artificial dissipation model. The original model had the unfortunate tendency to overwhelm the laminar viscosity as will be shown. Comparing Test Case 2 skin friction results obtained with the updated version of the PARC code (Fig. 2d) with results from application of the original version (Fig. 7a), a definite improvement is apparent with the new artificial viscosity model. However, all of the other boundary-layer parameters examined displayed less noticeable differences between the current version and the original version of the PARC code. For the subsonic Test Case 7, the situation is much clearer; comparing Figs. 5a, b, and d (new version results) with Figs. 7b, c, and d (old version

results), a significant difference is seen, especially in skin friction. This result is consistent with the fact that the magnitude of the artificial dissipation error is inversely proportional to the cell Reynolds number; and that, all others things equal, the lower Mach number test case has a smaller cell Reynolds number.

2.3.2 Turbulent Cases

The turbulent test cases (Table 2, Cases 9 through 17) show good agreement between the PARC code simulations and the boundary-layer code results. Of course it cannot be expected that the comparisons be as excellent as for the laminar cases since both programs require the use of semi-empirical turbulence models for turbulent flows. The biggest deviations are in skin friction and Stanton number (approximately a 5- to 10-percent error). Case 10, shown in Fig. 8, is typical of these results. It can be seen from Fig. 8 that, although the agreement is quite good qualitatively, there are minor deviations for all the parameters examined. Once again, as for the laminar test cases, the principal error seems to be introduced by an unfavorable interaction of the PARC solution algorithm with the fixed condition inflow boundary. However, for most engineering purposes these results would be more than adequate.

2.3.2.1 Grid Spacing Results

The results for the study of various streamwise grid spacings (Cases 9, 10, and 11) essentially produced the same results as was encountered with the laminar flow cases. Thus, the same conclusion holds that streamwise grid spacing on the order of several boundary-layer thicknesses produces as good results as finer grid distributions. Although the comparisons for the test cases with cross-stream variation in grid density (Cases 10, 12, and 13) were not as insensitive as for the similar laminar flow cases, examination of Fig. 9 shows that the densest grid produced only slightly better comparisons than the sparser grids. This is quite encouraging for the utilization of the PARC code in 3-D problems, since the coarsest grid is usually the best that can be economically allowed for these problems.

2.3.2.2 Thermal Properties Results

The results for the cooled wall test Case 14, for which the plate was held at a constant wall temperature one-half of the free-stream static temperature, show good comparisons on all parameters including Stanton number (Fig. 10). As can be readily seen by comparing Case 14 with the similar adiabatic Test Case 10 (Fig. 8), the agreement with the boundary-layer code results are unaffected. Comparisons for the heated wall Test Case 15 (Fig. 11) with a constant wall temperature that is double that of the free-stream, display results nearly as good as the cooled wall case (Fig. 10). On a percentage basis, the Stanton number results are actually better. Both cases are strongly affected by the inflow boundary error and should show much better comparisons if this could be eliminated.

2.3.2.3 Mach Number Variation Results

Variation of the Mach number (Test Cases 10, 16, and 17 for Mach numbers of 0.75, 0.1, and 2.5, respectively) showed little or no effect on the comparisons with the boundary-layer code (Contrast Figs. 8, 12, and 13).

2.3.2.4 Code Improvement Results

Test Case 9 was also simulated using the original PARC code algebraic turbulence model. When comparing Figs. 14 and 8, it is apparent that much better results were obtained with the current updated version of the PARC code. Although both turbulence model improvements as well as artificial viscosity improvements contributed to the enhanced comparison with the boundary-layer program's results, most of the change is attributable to the turbulence model. The old turbulence model should definitely not be used if the prediction of boundary-layer parameters is of importance, though note that the boundary-layer thickness is not greatly in error.

2.4 FLAT-PLATE VALIDATION PACKAGE

One of the primary objectives of this effort was to establish a body of appropriate data and computer codes to not only aid in current validation of the PARC code, but in future evaluation of PARC enhancements. A partitioned file was established for the codes required for flat-plate validation for both laminar and turbulent flows. This partitioned data set contains the following codes:

1. Boundary-layer code (Refs. 1 and 2) that produces
   a. the grid both for its own use, but also for use by the PARC code;
   b. flat-plate flow-field solution, which is used for
      (1) the PARC initial condition restart file, and
      (2) the plot program data file;
2. Interpolation code that interpolates the solution from the boundary-layer code any other grid;
3. PARC code execution file that
   a. includes required job control statements for file handling;
   b. includes boundary conditions and initial setup parameters; and
   c. executes PARC code;
4. Plot codes that
   a. plot solutions from boundary-layer code versus PARC code for all parameters indicated in the figures; and
   b. plot comparisons from three PARC restart files.

3.0 SUPERSONIC FREE JET

3.1 MOTIVATION

The choice of the supersonic free-jet wake as a fundamental validation case was motivated by the type of testing performed in the ETF. Whether the propulsion system is a turbine engine or a rocket motor, the exhaust gases are removed from the test article by exhausting through a nozzle into the test cell environment and, thence, into an exhaust collector (diffuser). Since the exhaust collection hardware cannot be directly connected to the test article (because it would directly influence the thrust measurements), the exhaust gases flow as a free jet for some distance. The testing of turbine engine/inlet systems in a free jet, where the engine/inlet system is located just downstream of a nozzle, is also routinely practiced in the ETF.

3.2 TEST CASE

The supersonic free-jet flow validation was conducted with the jet originating from a converging/diverging nozzle with nearly uniform Mach 2.22 flow at the nozzle exit. The flow exhausted into quiescent air with the flow total temperature equal to the ambient temperature. In addition to comparisons with experimental data, a comparison between the original version of the PARC code and the latest version was made for the near-field supersonic flow, and a comparison between two different mixing coefficients in the algebraic turbulence model was made for the far-field supersonic flow. The near-field comparison was made to ensure that the changes made to the PARC code did not influence the free-jet wake results (which they did not), and the far-field comparison was made to study the influence of the turbulence model mixing coefficient on the free-jet mixing region spread rate. The grids used in this effort were moderate (as defined in Section 2.2) in both the cross-flow and streamwise directions, and were not varied in the analysis. Close to the nozzle exit, there were approximately 25 grid points spread across the free shear layer. This number increased as the distance from the nozzle increased because of the spreading of the jet. The validation effort for the free-jet flow has been limited to this one case by the available time allotted for this investigation. Additional cases will be studied in FY89.

Validation data for the free-jet case has been taken from Ref. 4. The Ref. 4 report provides a thorough and complete set of data for supersonic free-jet flow, both in the core region (near field) and in the developed region (far field). The supersonic free-jet data reported in Ref. 4 were obtained in a carefully controlled test environment and are believed to be of high quality. The uncertainties of the velocity data are reported to be ± 0.75 percent on the centerline, with the uncertainty increasing to ± 1.0 percent where U/Umax = 0.3 and ± 15 percent for U/Umax = 0.1.

3.3 SUPERSONIC FLOW—NEAR FIELD

The Ref. 4 report defined the near field as being the region upstream of where the core collapses and only the mixing region is present (See Fig. 15 for sketch of basic configuration and definition of terms). To simulate the supersonic near-field flow, the grid geometry shown in Fig. 16 was used. The nozzle was modeled starting upstream of the throat to provide the proper boundary-layer thickness at the nozzle exit. The results of the CFD analysis, depicted as Mach number contours, are shown in Fig. 17. To compare the PARC results to those of Ref. 4, X-velocity profiles were generated at the locations downstream of the nozzle exit where the data were taken. These comparisons are shown in Fig. 18. The PARC code does extremely well predicting the flow velocity in the near field.

A comparison was also made to the location of where the X-velocity is equal to one-half the centerline velocity at a given axial location. This is shown in Fig. 19 for both the new version and the old version of the code. Note that the raggedness of the PARC results is attributable to poor interpolation techniques. It is concluded that both versions of the PARC code do an excellent job of simulating the near-field flow out of a supersonic circular jet. This was expected, of course, since the changes to the PARC code algebraic turbulence model were directed at flow along a solid boundary, not a free-mixing boundary.

3.4 SUPERSONIC FLOW—FAR FIELD

The grid used to generate the far-field supersonic flow results is shown in Fig. 20. To provide the correct inflow boundary conditions at the nozzle exit, the values generated in the near-field solution were transferred to this grid and fixed. This was performed only to save the time of having to resolve the internal nozzle flow field. The results of the analysis are shown in Fig. 21 as Mach number contours. The results were generated using the new version of the code. As with the near-field case, the PARC results were compared to the X-velocity profiles obtained from Ref. 4. These comparisons are shown in Fig. 22. As can be seen, as the flow travels farther downstream of the nozzle, the results get worse. Both the spreading rate and the centerline velocity are off by as much as 100 percent at the locations greater than 100 nozzle radii downstream of the nozzle exit.

The radial location of the point where the velocity equals one-half the centerline velocity for the far-field case is shown in Fig. 23. As previously stated, the Ref. 4 data show a more severe level of mixing than the results from the PARC code. The value of 0.09 for the mixing coefficient in the turbulence model was tried in order to see if any improvement could be obtained with a higher rate of mixing. The most apparent effect was to cause the velocity profiles close to the nozzle to spread too quickly, while simply putting off the divergence from the data to a location farther downstream of the nozzle. It is unlikely that further increases

would have given better results than those reported here. It is interesting to note that the near-field region agrees closely with the referenced data with a 0.07 mixing coefficient (as discussed in the previous section). When the flow enters the far-field region, the actual flow increases its angle of divergence. The PARC code does not recognize this phenomena, maintaining a constant spread rate from near field to far field.

4.0 BACKWARD-FACING STEP

4.1 MOTIVATION

Backward-facing steps are ideal for a study of the PARC code's ability to handle flow recirculation zones and plate impingement heat-transfer problems. Recirculations and wall-impingement heat transfer are of concern in almost all propulsion testing problems and, in particular, in test facility problems with adverse nozzle exhaust/diffuser interactions.

4.2 TEST CASE

Validation data for the backward-facing step was taken from data gathered as a result of the Stanford conference. Stanford University researchers collected the data to set a standard for code validation data, and the data were used as the baseline case in this study. The validation data (Ref. 5) represents a complete set of fluid dynamic and heat-transfer data for the backward-facing step with low Mach number flow. The dimensions of the configuration are shown in Fig. 24, which also presents the initial flow and boundary conditions. The reference data were taken with an upstream boundary-layer thickness of 1.1-step heights, except for skin friction that was taken over a range of boundary-layer thicknesses. This data was taken at a reference Reynolds number of 28,000, based on step height.

4.3 PARC CODE SETUP

The computational grid used in this check case has dimensions of 125 by 101 and is shown in Fig. 25. The inflow plane upstream of the backstep was fixed at the experimentally measured flow values, and the outflow plane was computed as a constant static pressure-free boundary. The outer boundary, away from the wall, was treated as a no-slip adiabatic surface, and the wall surface upstream of the backstep is also treated as a no-slip adiabatic surface. The wall surface downstream of the step is treated as no-slip with a prescribed wall heat-transfer rate per unit area as a boundary condition.

4.4 RESULTS

Comparisons of validation data (Ref. 5) and PARC code results for the backward-facing step were surprisingly good considering the known problems that algebraic turbulence models have with massively separated flows. Figure 26 shows comparisons of validation data and PARC code calculated values for the axial velocity component (U/Uref) versus distance from the lower wall (Y/H) at different axial locations (X/H). For this parameter, comparisons are generally quite good, except for the peak backflow velocities, which are much too high. After impingement, which is predicted rather well, the profiles near the wall compare favorably with the data. Comparison of validation data and PARC code calculated values for temperature (T – Tinf) versus distance from the lower wall (Y/H) at different axial locations (X/H) are shown in Fig. 27. As with the velocity profiles, the temperature profile comparisons with data improved downstream of the impingement point. The vortex region proved the most difficult to correlate, which is not surprising for an algebraic turbulence model. Comparisons of lower wall temperature versus axial location (X/H) are shown in Fig. 28. As expected, the comparisons agree much better downstream of the impingement point (X/H = 6.7, for the experimental data). A comparison of skin friction (Cf) from experimental values and PARC code computations is shown in Fig. 29. The recirculation zone shows the poorest comparison between the data and PARC solutions, consistent with the PARC code results overshooting in backflow velocities. Once the flow reattaches, the comparisons improve considerably.

5.0 SUMMARY

A significant step towards meeting the objectives of this effort has been made. The PARC Navier-Stokes computer program has been used to simulate some fundametal flows typically encountered in the testing of turbine engines and rocket motors at the Arnold Engineering Development Center. These simulations have been compared with experimental data and/or other CFD code simulations, and the quality of the comparison evaluated. Laminar and turbulent flow simulations for a flat plate with zero pressure gradient have been compared with solutions of the boundary-layer equations with good-to-excellent results. These test cases examined effects of grid spacing in both the streamwise and cross-stream directions, compressibility, and heat transfer. The laminar flow simulations with a new artificial viscosity model were in excellent agreement with the boundary-layer code results; the turbulent simulations with a new Baldwin- and Lomax-style turbulence model compared less favorably with some cases showing a 10-percent error in skin friction. Results obtained with the older version of the PARC code without either of these improvements had considerably poorer comparisons with the boundary-layer code simulations, especially the turbulent cases. Both of these improvements have been incoporated into the 1988 version of the PARC code (See Appendixes A and B for an overview of these upgrades). The near wake of turbulent supersonic

jet was also simulated, comparing very well with experimental data. Results for the far wake for the same test case were poor, since the turbulence model failed to allow for the differences in near- and far-wake flows. The low-subsonic Standford backstep flow was also simulated for the case with heat transfer. Although the reattachment length was well predicted, and redevelopment of the flow downstream of attachment compared favorably with the experimental data, the flow in the recirculation zone showed the familiar defects of algebraic turbulence models, which are not optimized to this flow (e.g., reversed flow velocity overshoots). Overall, the performance of the PARC code was such that would lend confidence to its usage in propulsion flow simulations.

REFERENCES

1. Adams, J.C., Jr. "Eddy Viscosity-Intermittency Factor Approach to Numerical Calculation of Transitional Heating on Sharp Cones in Hypersonic Flow." AEDC-TR-70-210 (AD-714058), November 1970.

2. Adams, J.C., Jr. "Implicit Finite-Difference Analysis of Compressible Laminar, Transitional, and Turbulent Boundary Layers Along The Windward Streamline of a Sharp Cone at Incidence." AEDC-TR-71-235 (AD-734535), December 1971.

3. Whitfield, D.L. "Integral Solutions of Compressible Turburlent Boundary Layers Using Improved Velocity Profiles." AEDC-TR-78-42 (AD-A062946), December 1978.

4. Eggers, James M. "Velocity Profiles and Eddy Viscosity Distributions Downstream of a Mach 2.22 Nozzle Exhausting to Quiescent Air." NASA TN D-3601, September 1966.

5. Vogel, J.C. and Eaton, J.K. "Heat Transfer and Fluid Mechanics Measurements in the Turbulent Reattaching Flow Behind a Backward Facing Step." MD-44, Stanford University, August 1984.

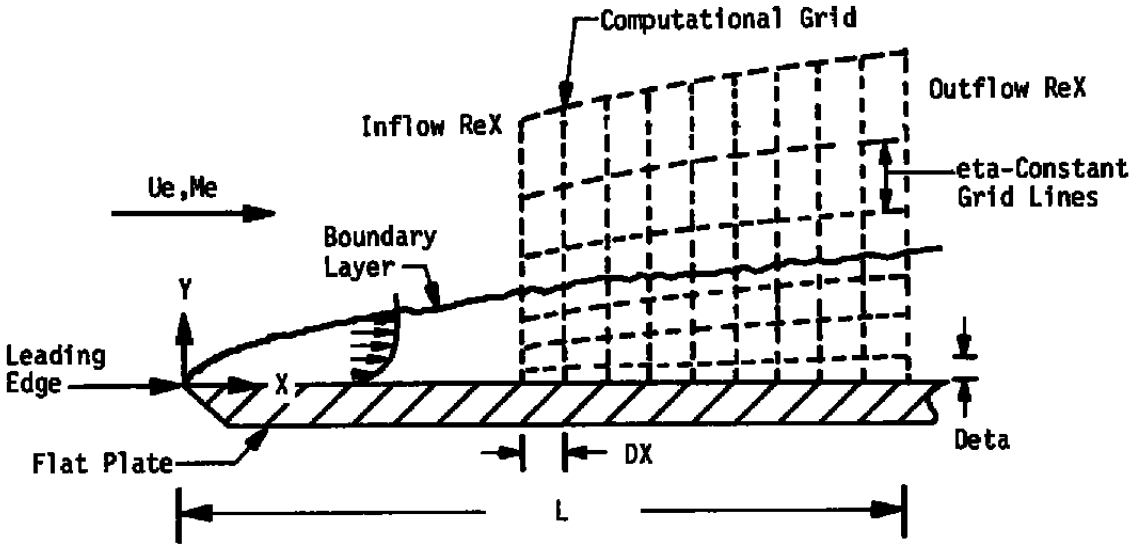

$$ReX = \rho e Ue X/\mu e$$

$$Y(eta) = \frac{X}{\sqrt{ReX}} \int_0^{eta} \frac{\rho e}{\rho(Z)} dZ$$

$$eta(K) = eta\,(K-1) + alpha \times [(eta\,(K-1) - eta\,(K-2)]$$

where eta (2) = Deta

eta (1) = 0

Figure 1. Basic formulation of flat-plate test cases.

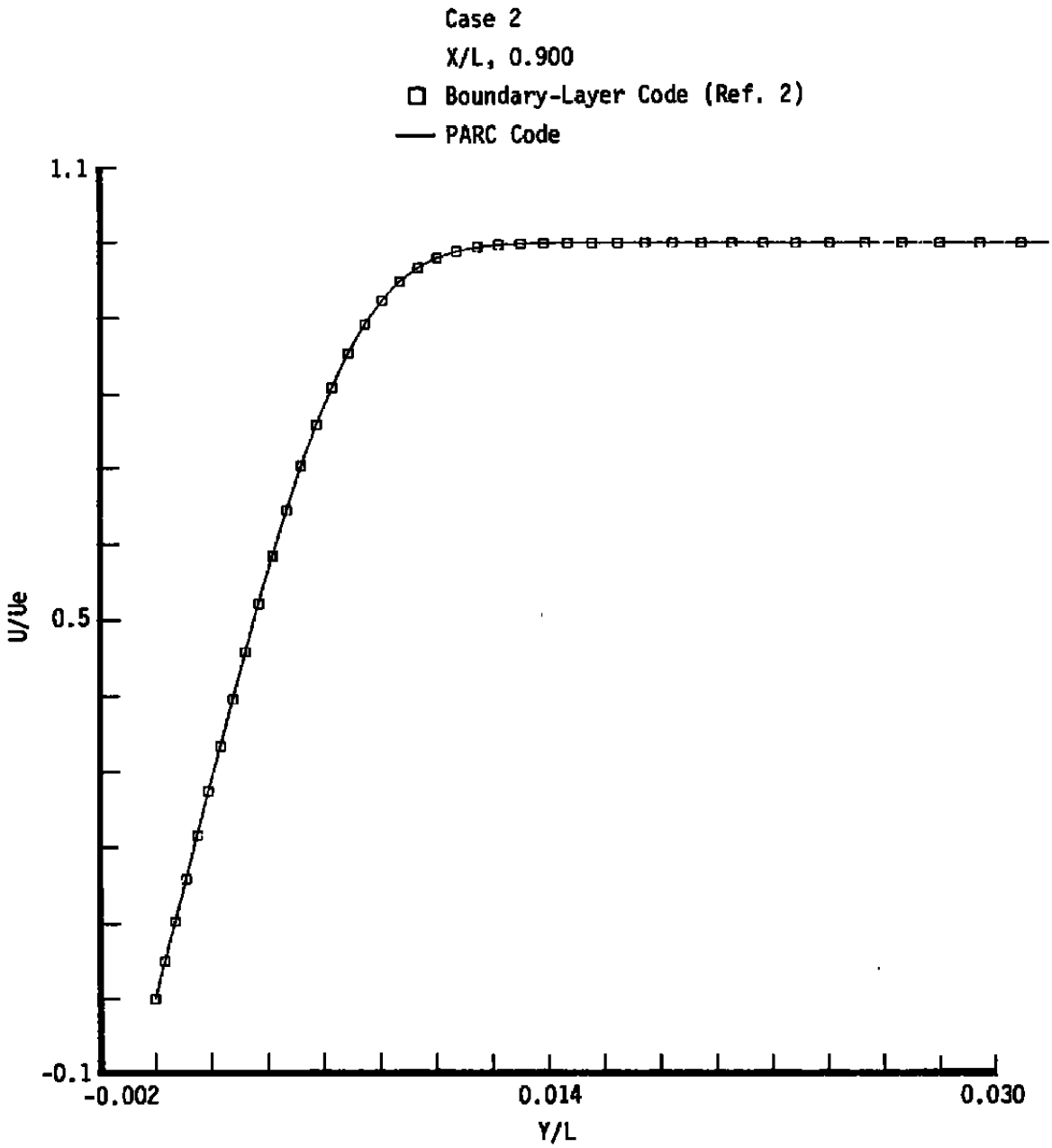

a. Velocity profile

Figure 2. Transonic laminar flat-plate flow comparisons.

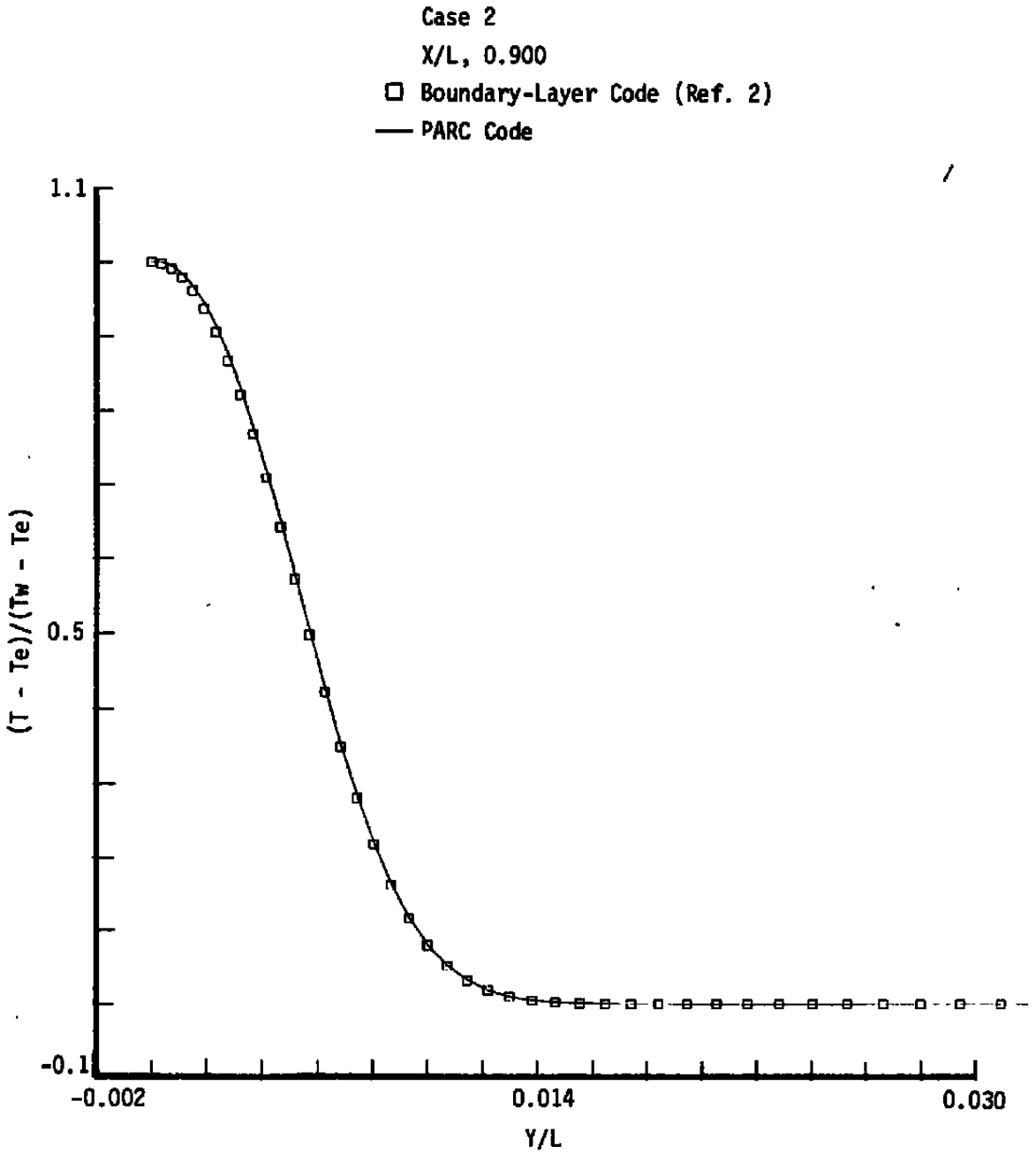

b. Temperature profile
Figure 2. Continued.

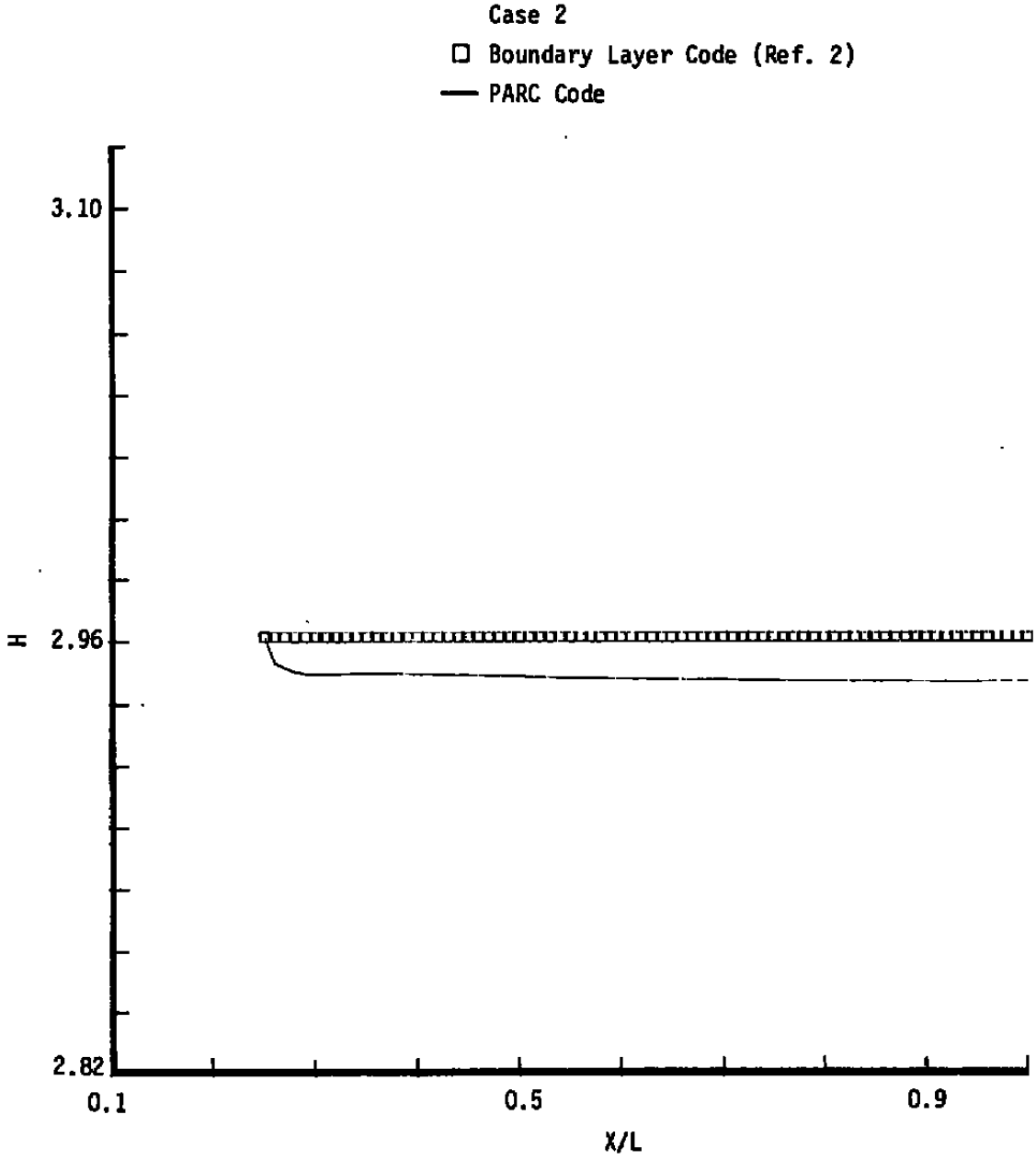

c. Shape factor streamwise variation
Figure 2. Continued.

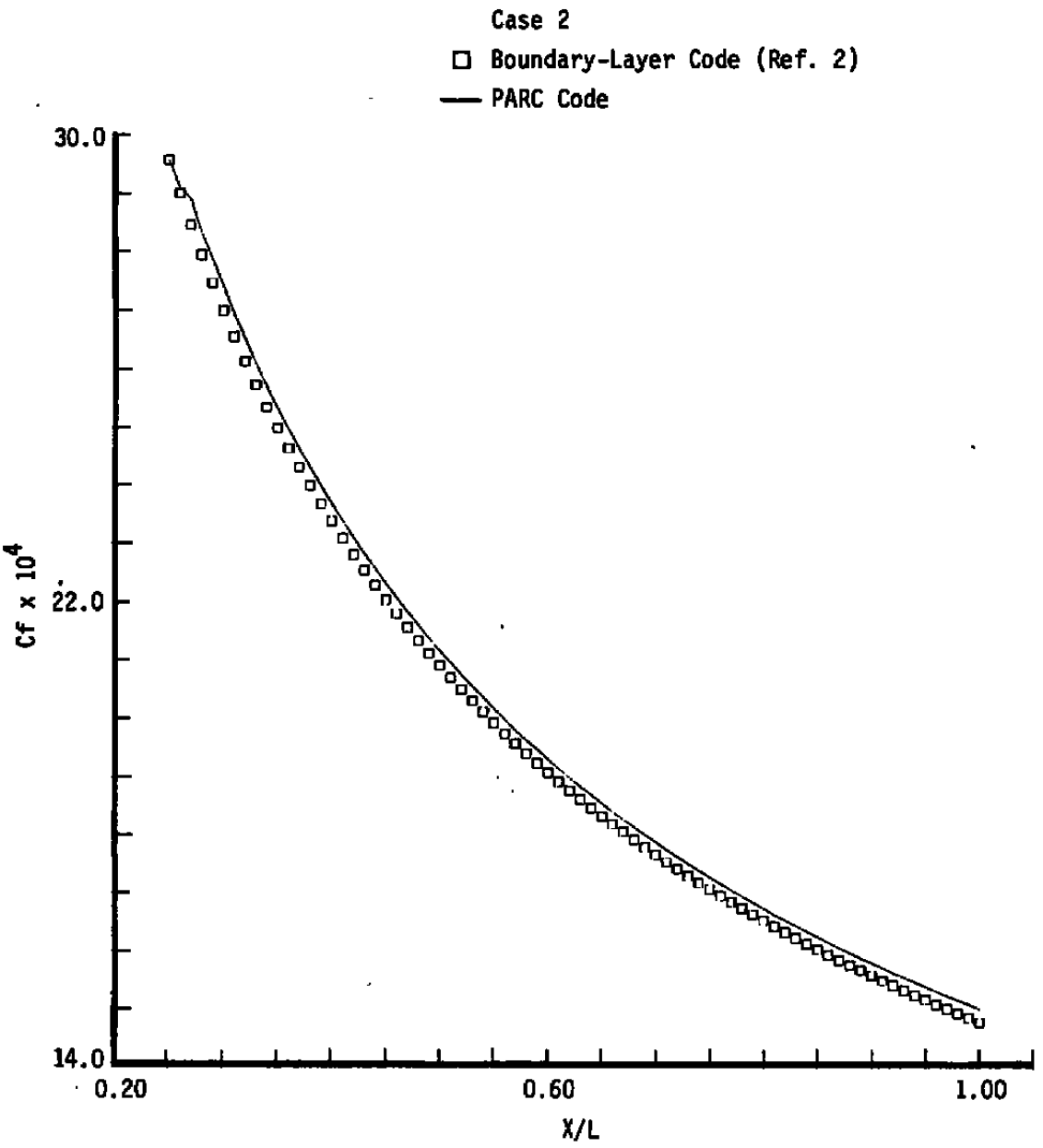

d. Skin friction streamwise variation

Figure 2. Concluded.

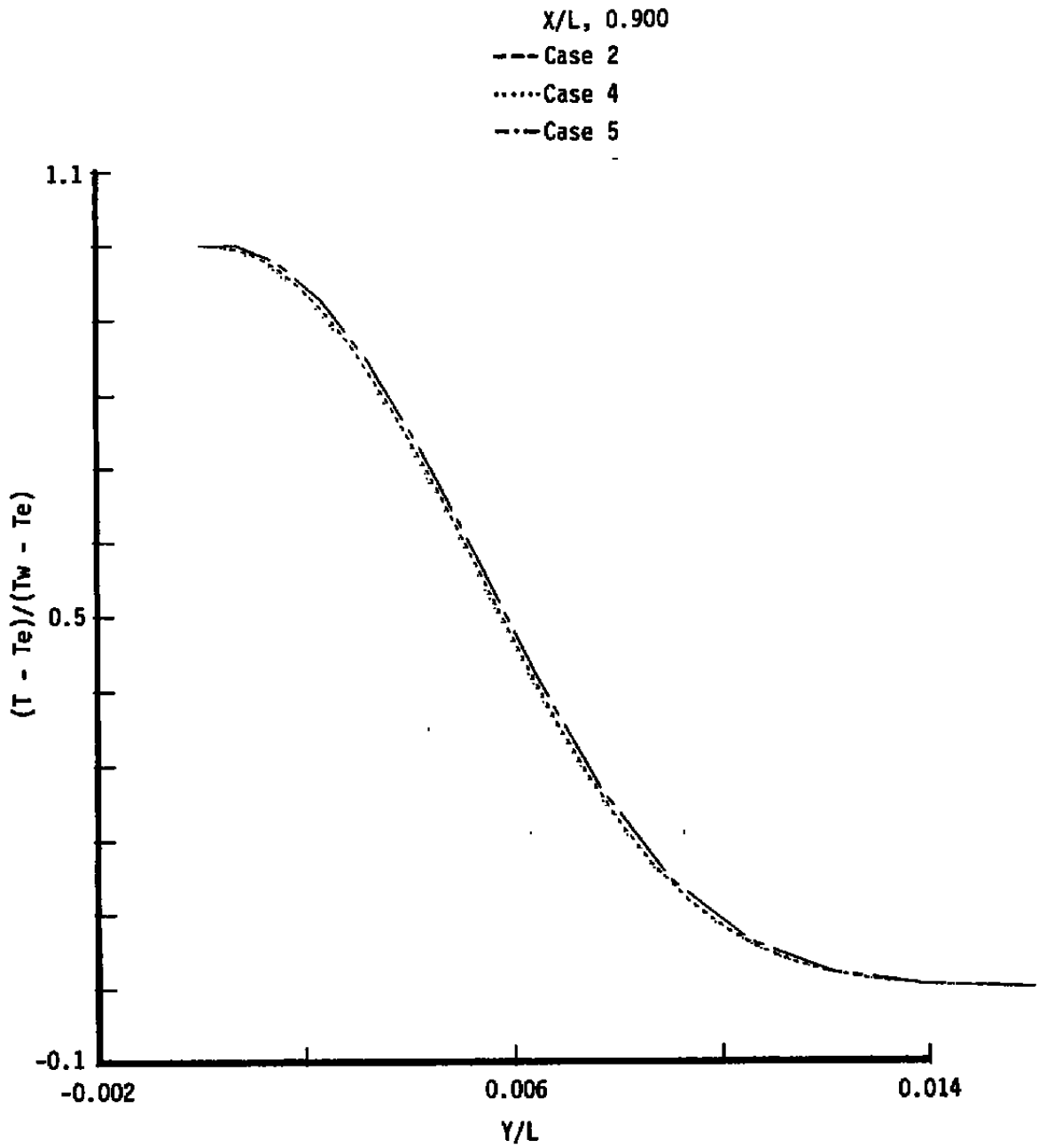

a. Temperature profiles (Cases 2, 4, and 5)

Figure 3. Grid density effects on laminar flat-plate comparisons.

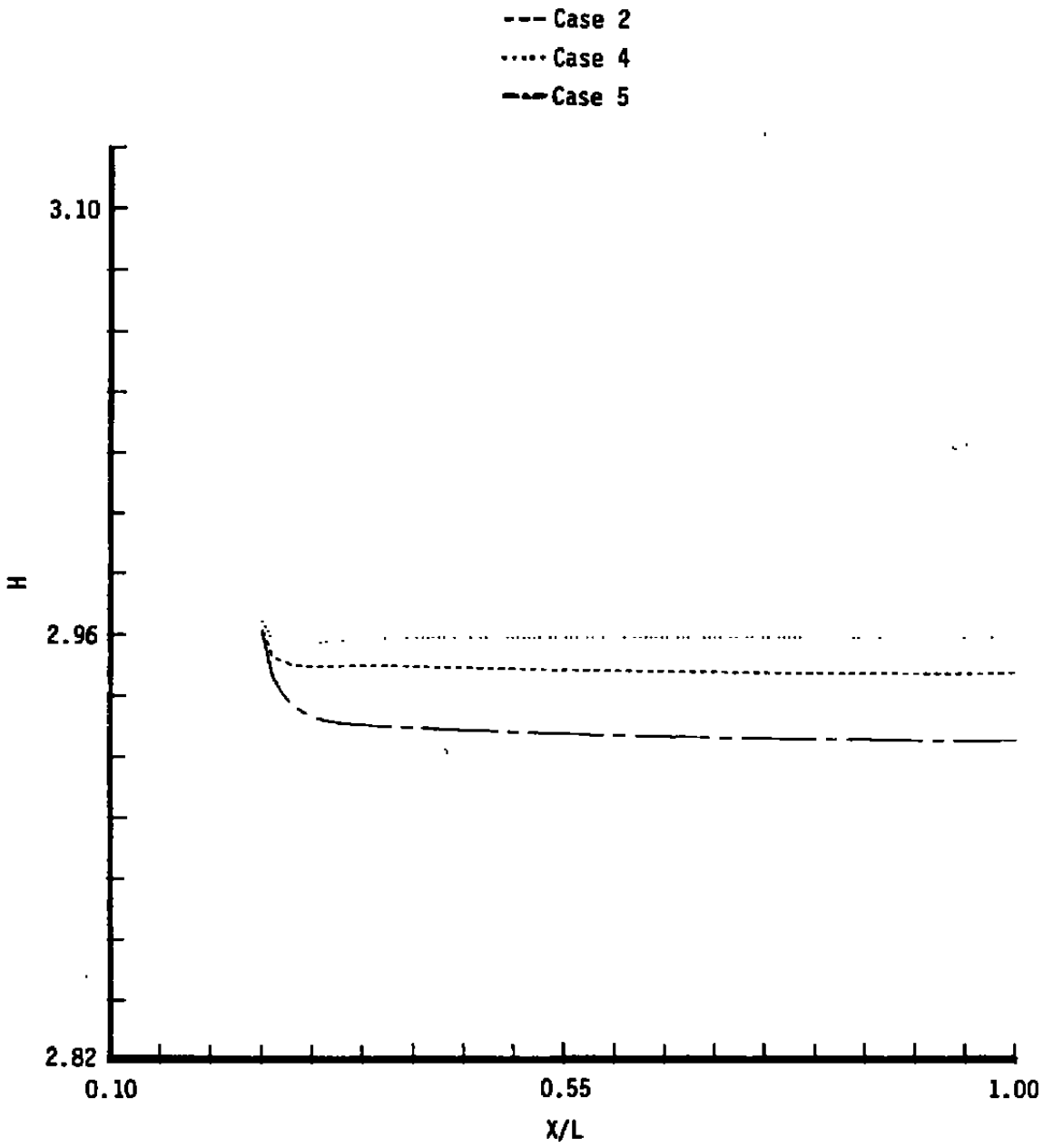

b. Shape factor variation (Cases 2, 4, and 5)
Figure 3. Continued.

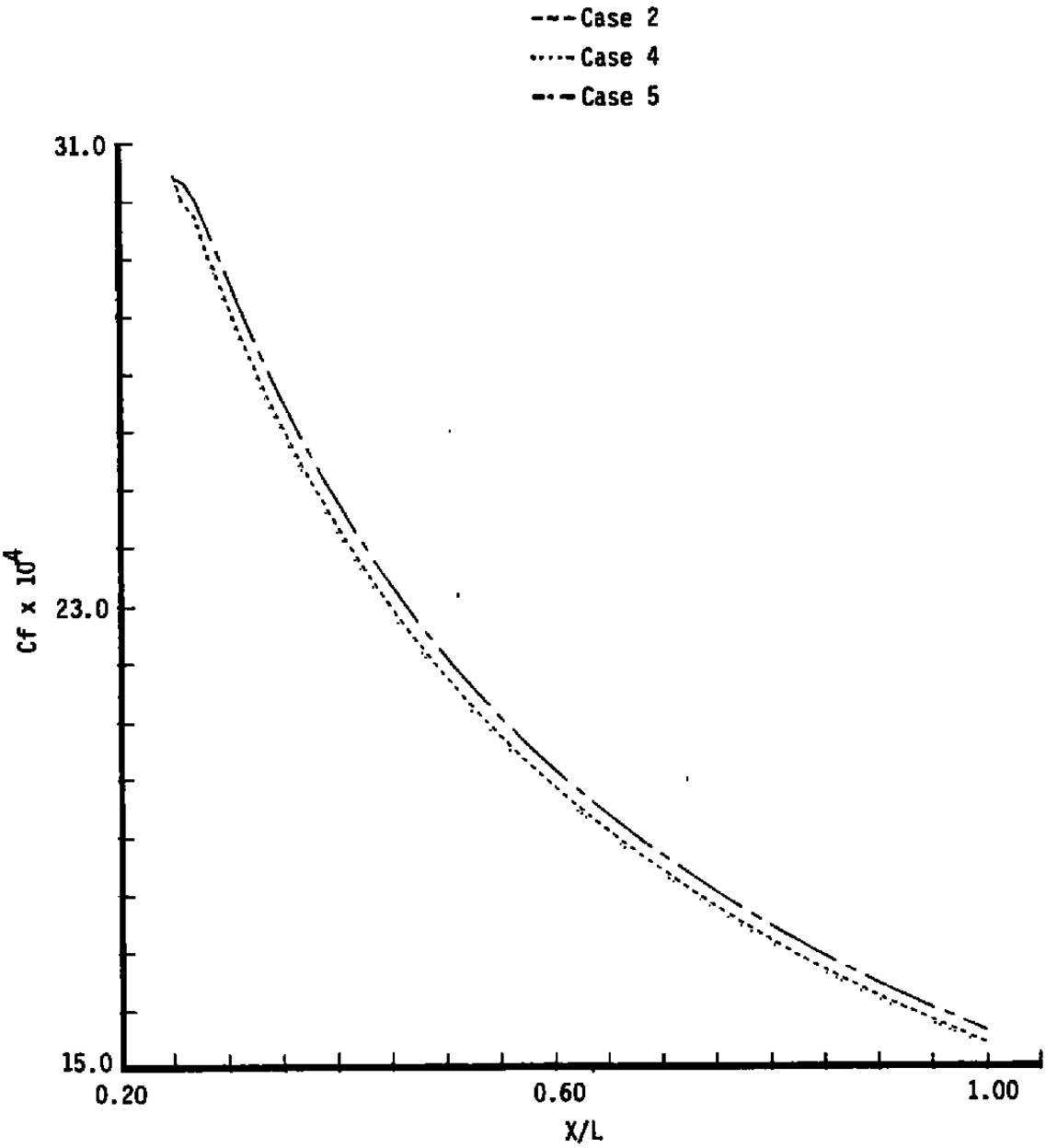

c. Skin friction variation (Cases 2, 4, and 5)
Figure 3. Concluded.

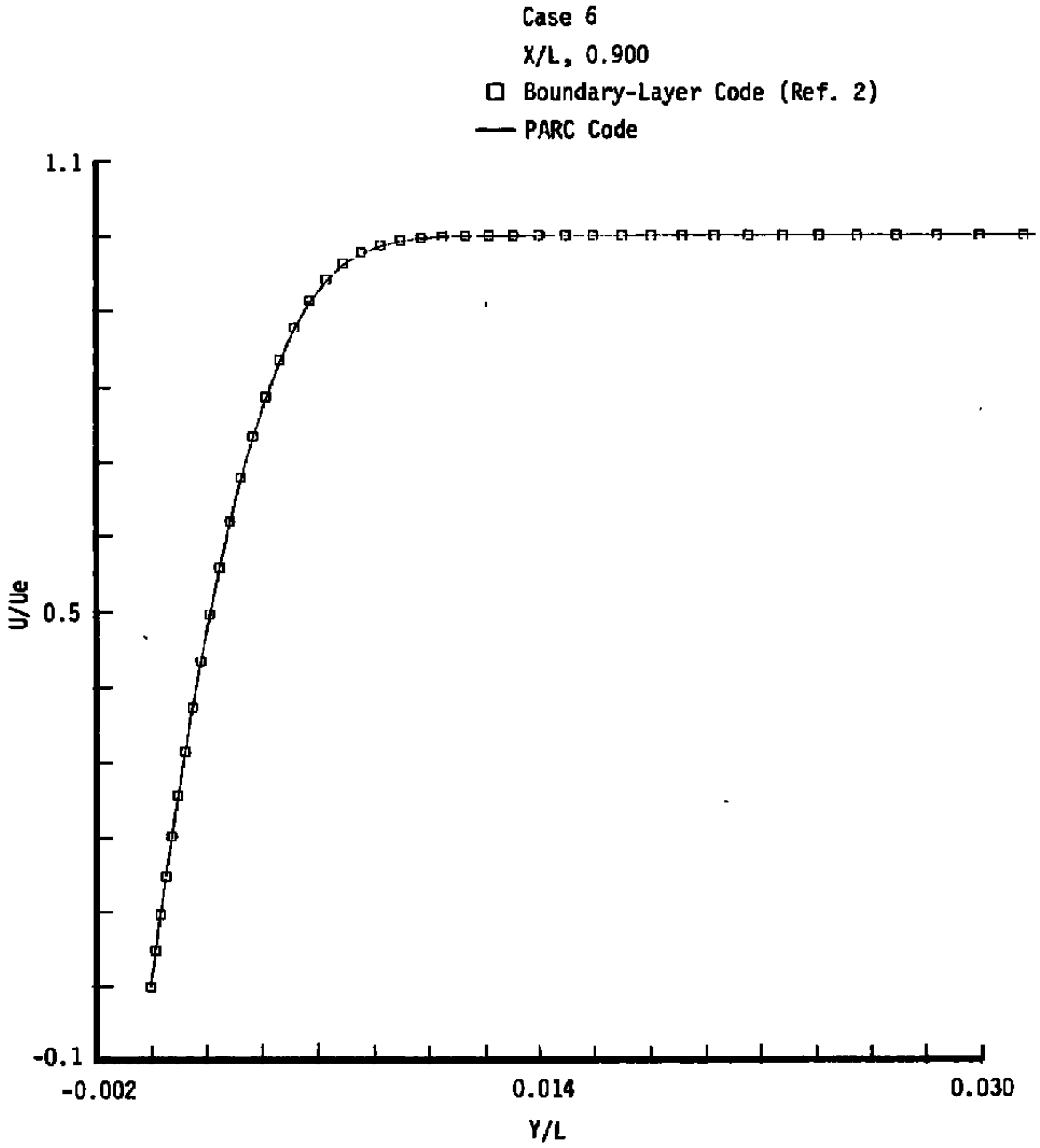

a. Velocity profile

Figure 4. Cold-wall comparisons for laminar flat-plate flow.

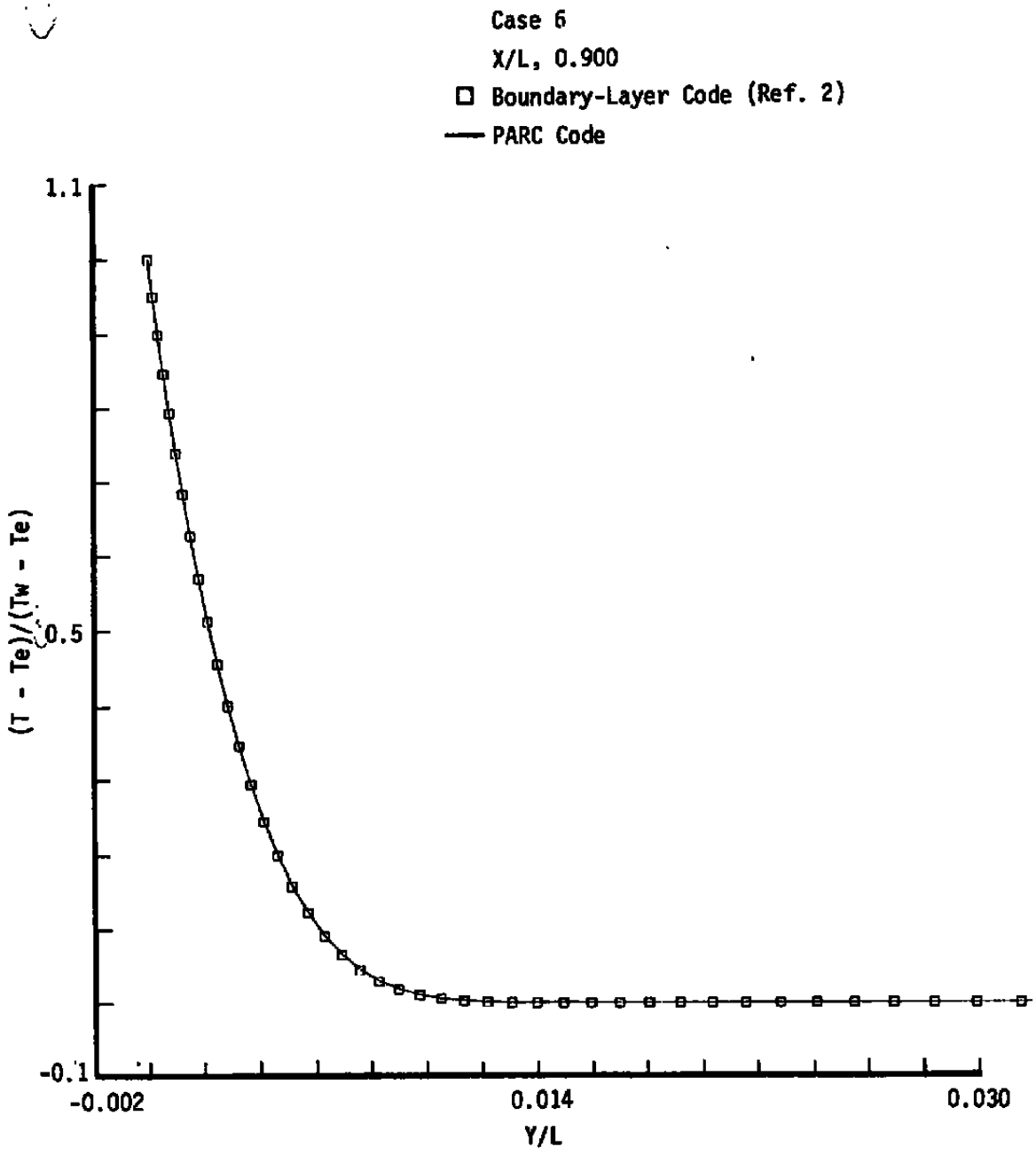

b. Temperature profile
Figure 4. Continued.

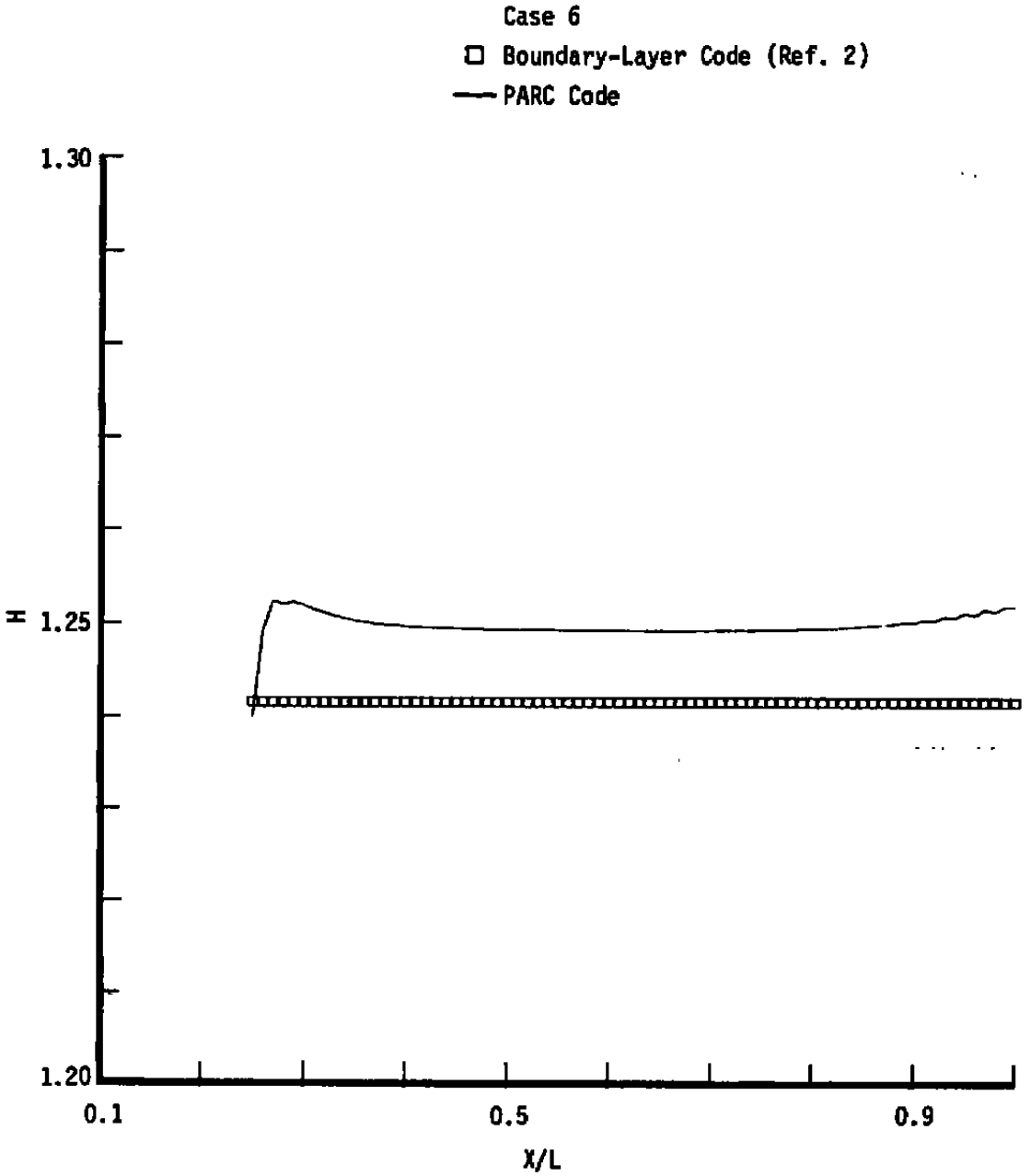

c. Shape factor streamwise variation
Figure 4. Continued.

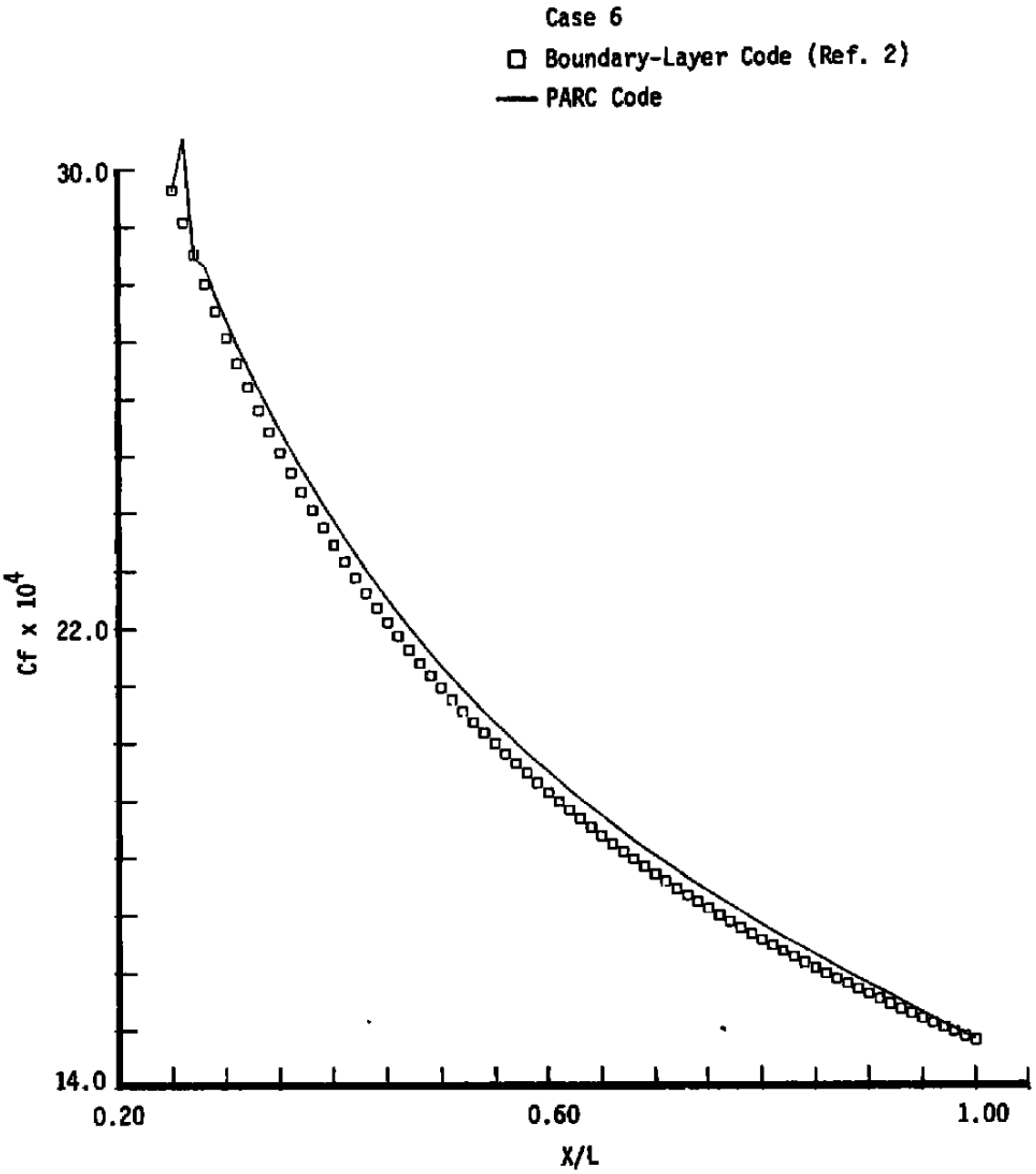

d. Skin friction streamwise variation
Figure 4. Continued.

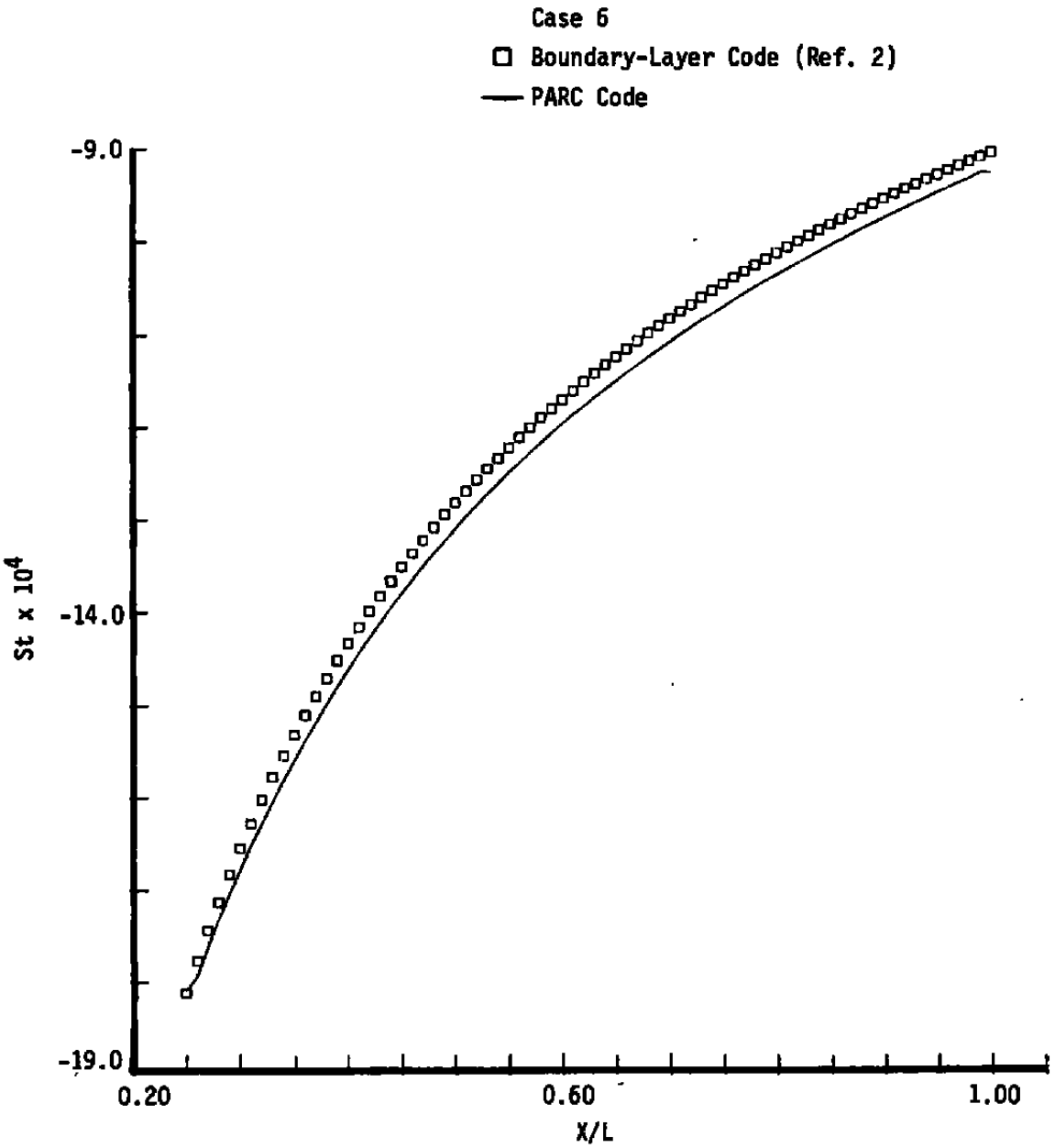

e. Stanton number streamwise variation

Figure 4. Concluded.

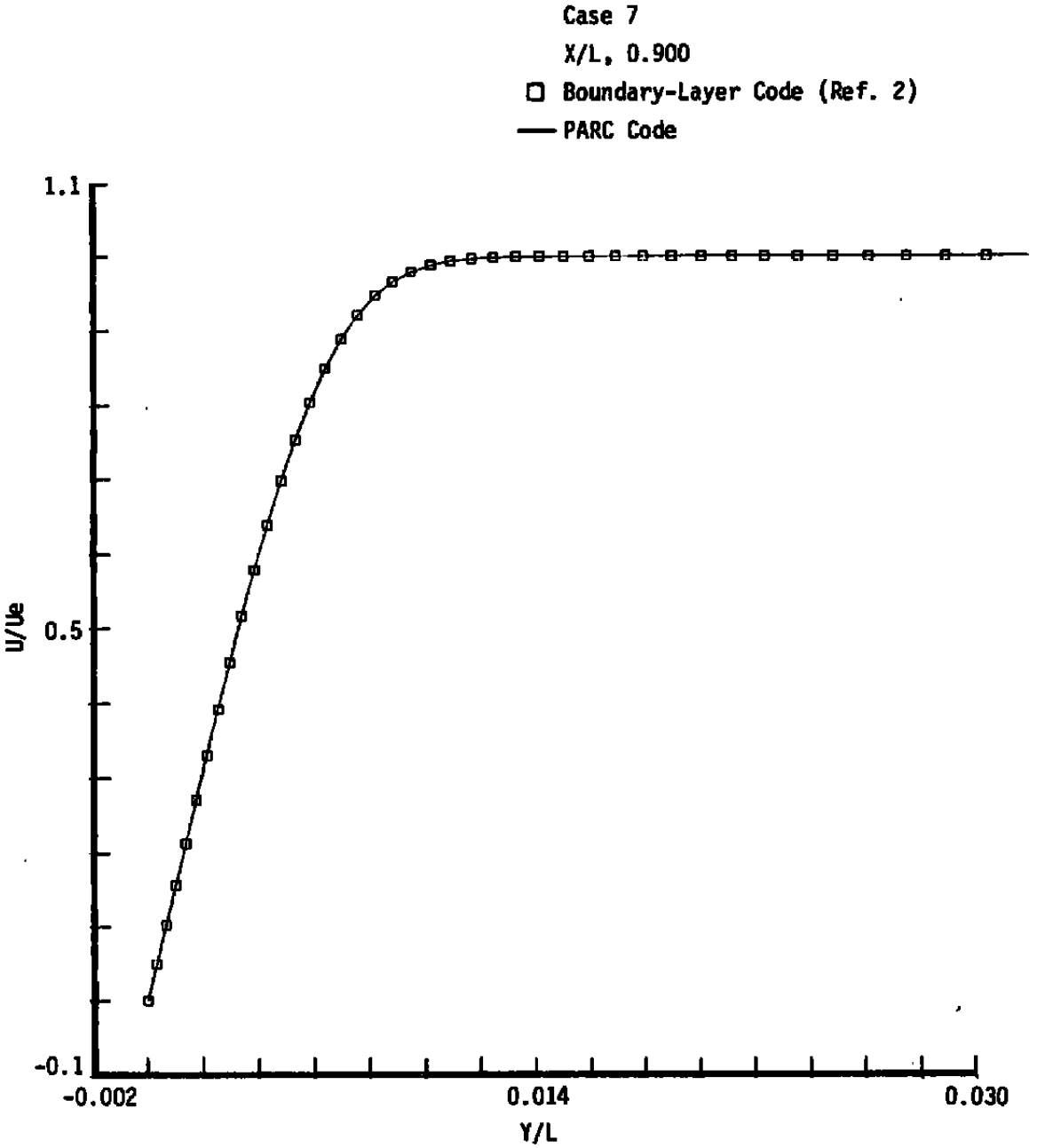

a. Velocity profile

Figure 5. Subsonic laminar flat-plate flow comparisons.

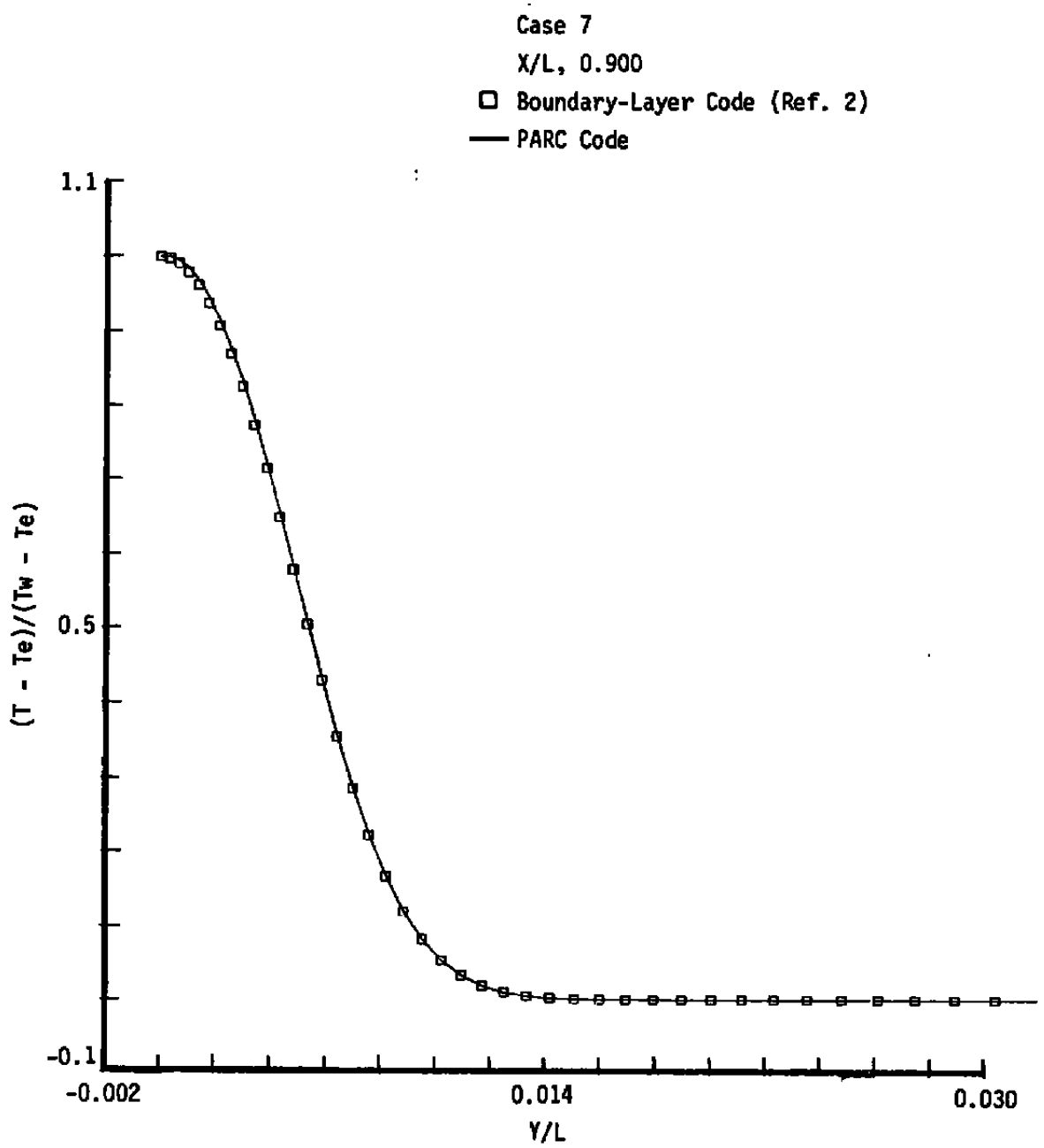

b. Temperature profile
Figure 5. Continued.

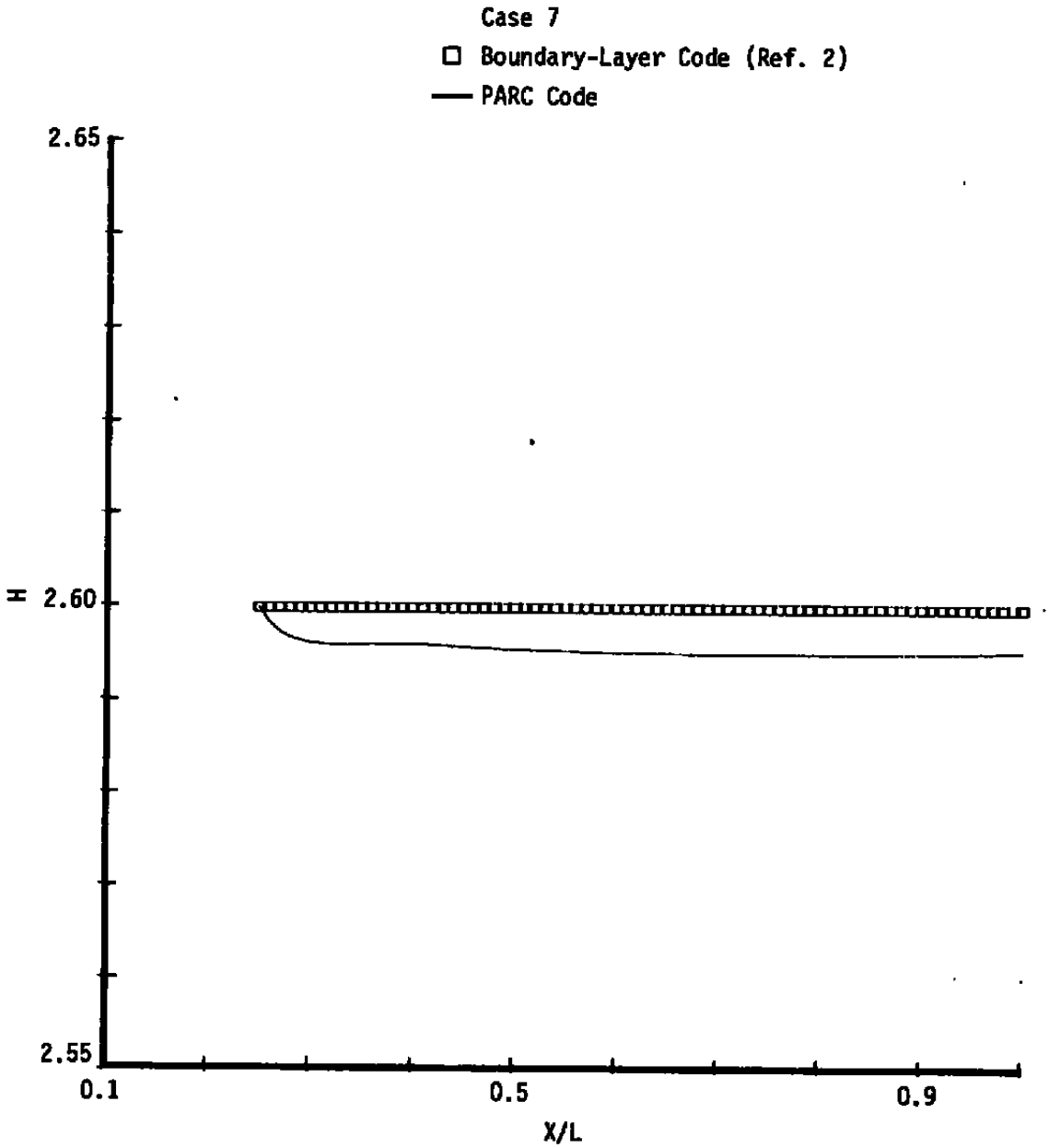

c. Shape factor streamwise variation

Figure 5. Continued.

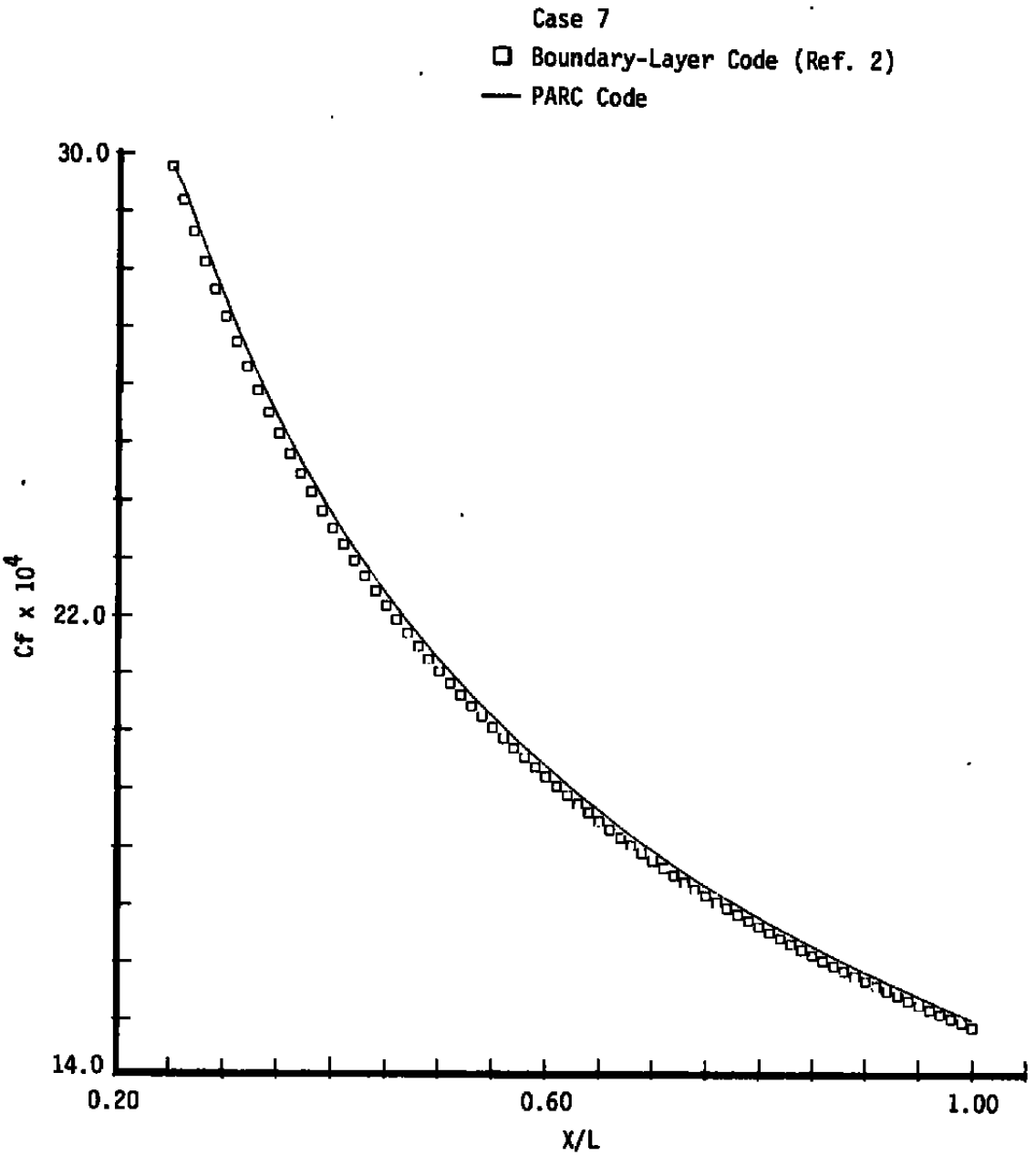

d. Skin friction streamwise variation

Figure 5. Concluded.

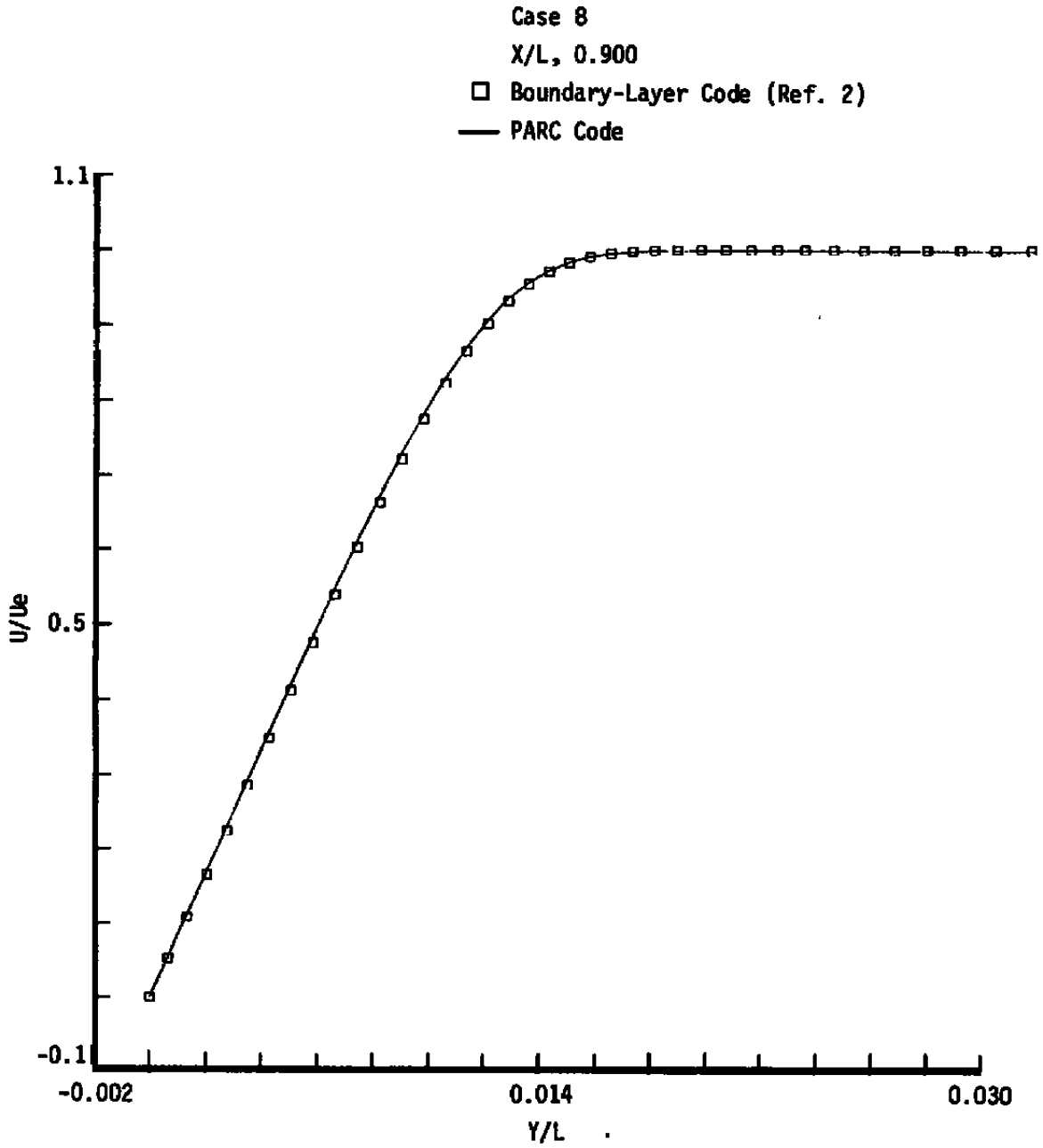

a. Velocity profile

Figure 6. Supersonic laminar flat-plat flow comparisons.

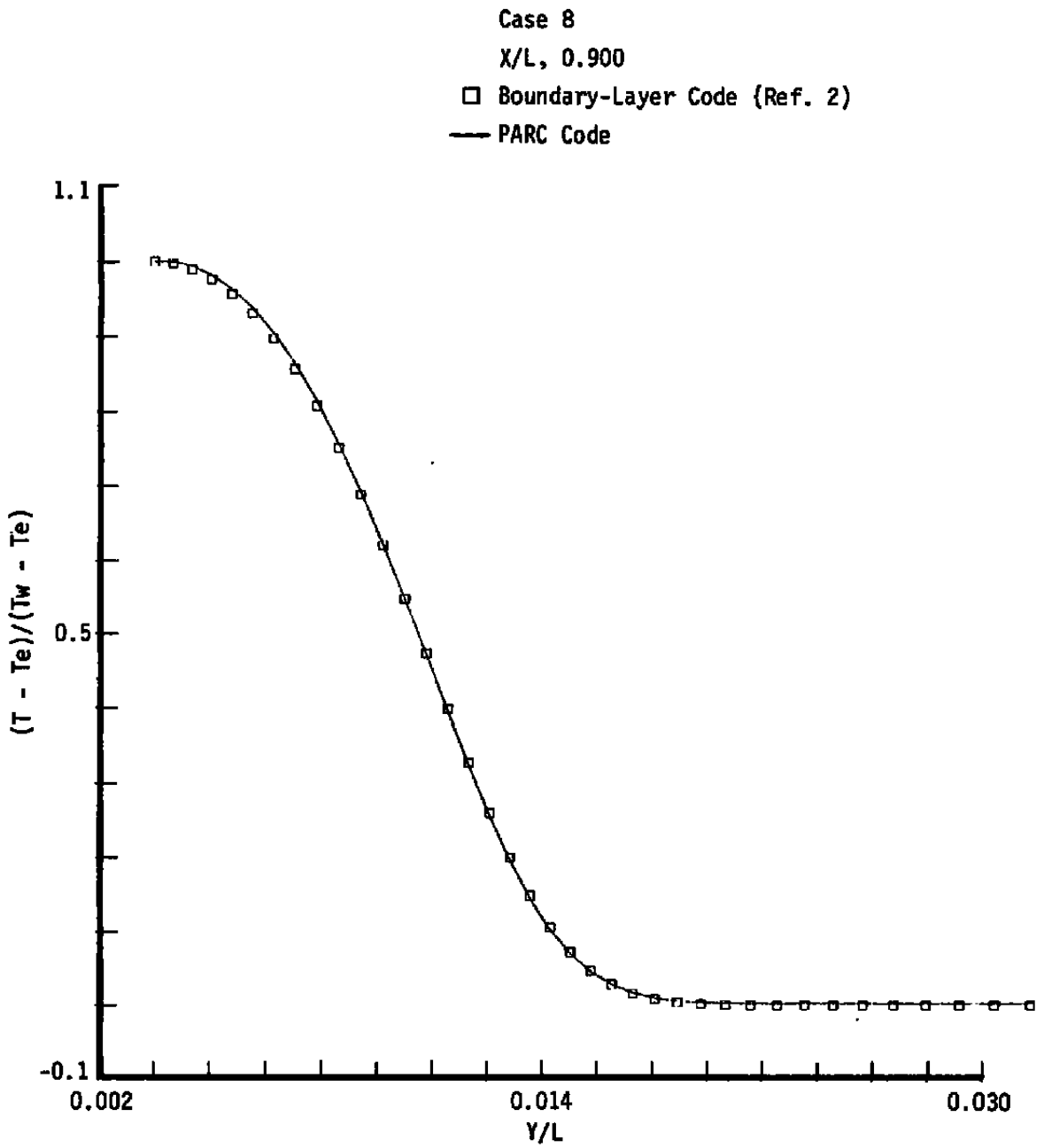

b. Temperature profile
Figure 6. Continued.

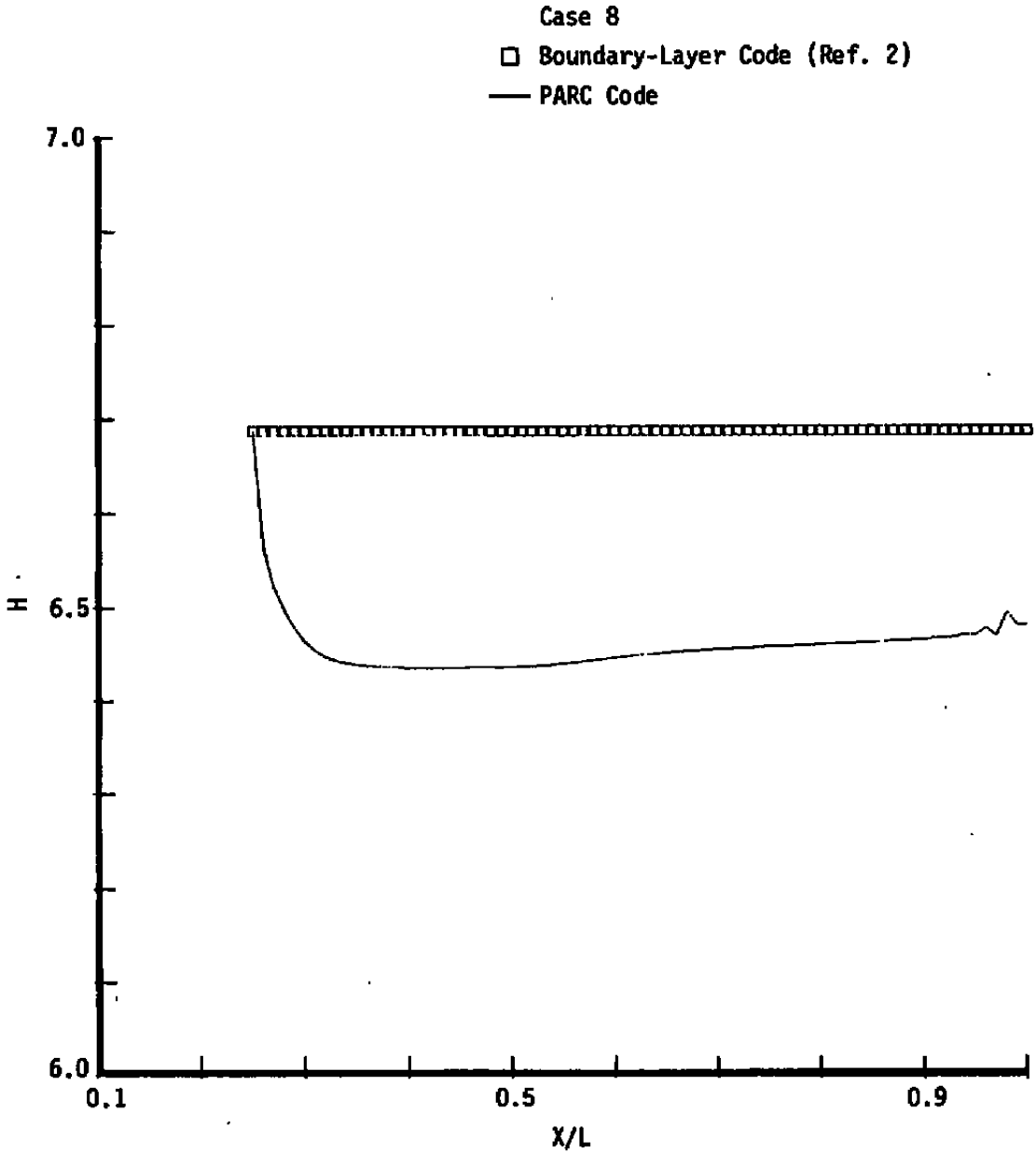

c. Shape factor streamwise variation
Figure 6. Continued.

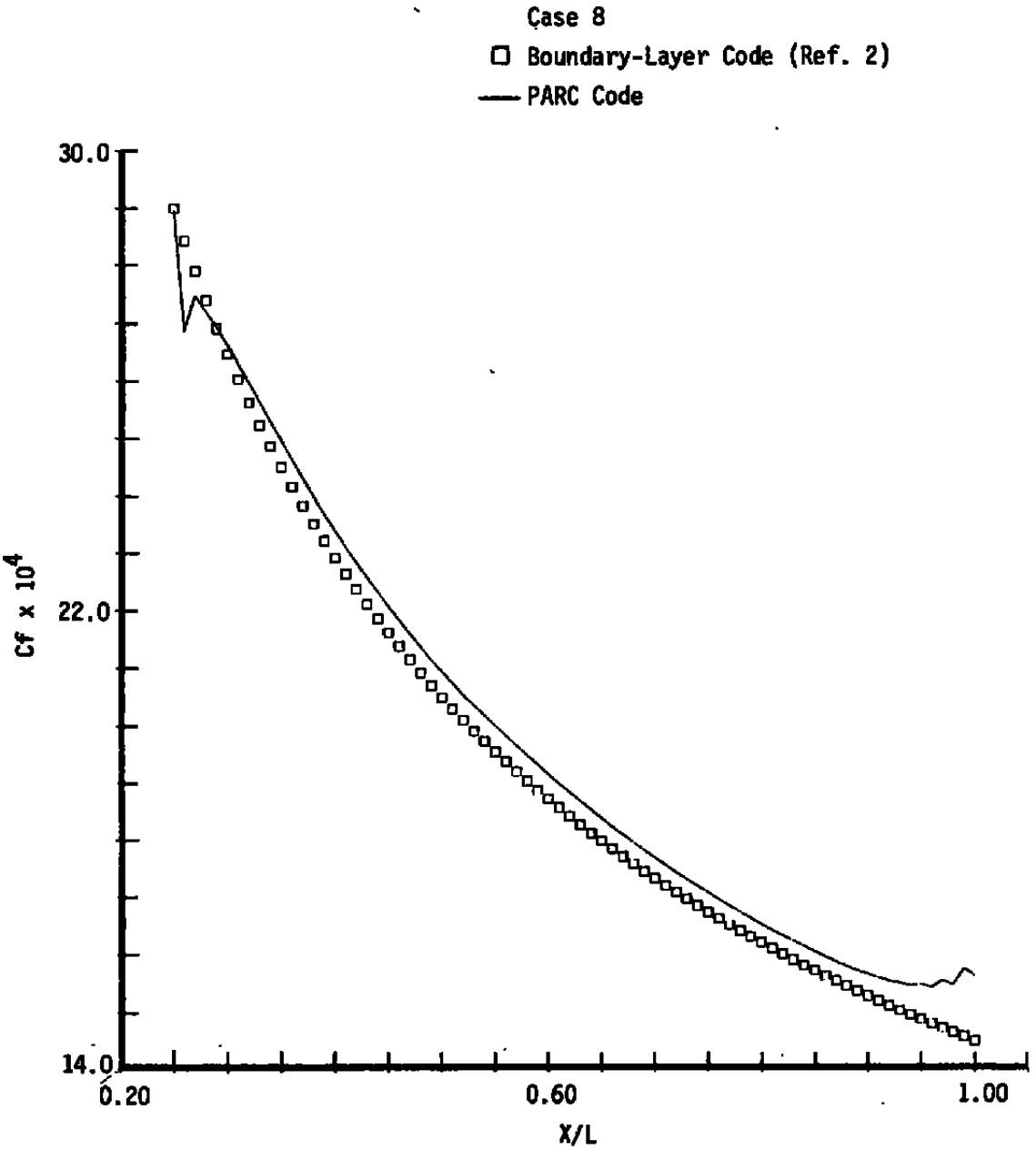

d. Skin friction streamwise variation

Figure 6. Concluded.

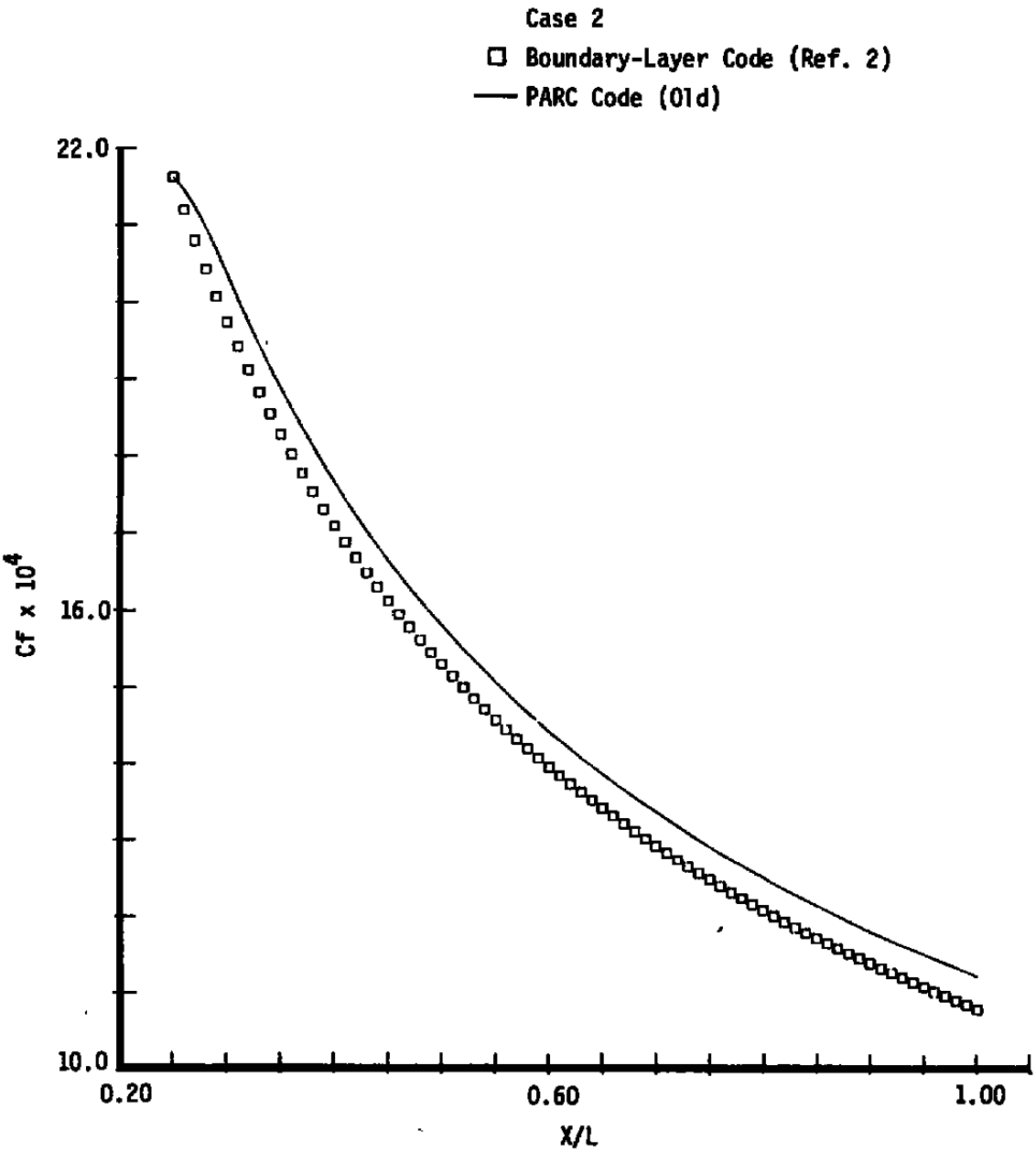

a. Skin friction variation (old model, Case 2)

Figure 7. Artificial viscosity model effects on laminar flat-plate flow.

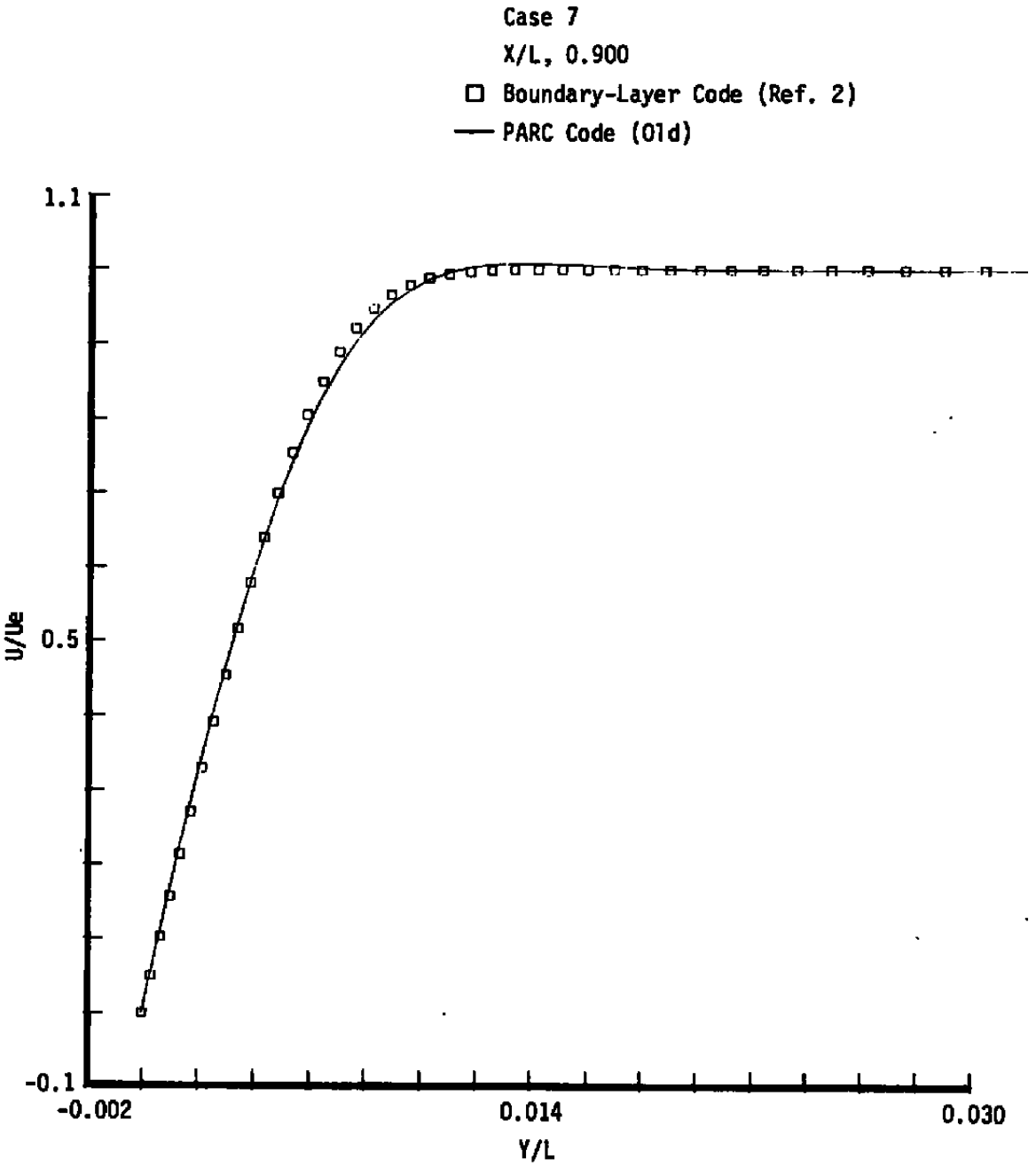

b. Velocity profile (old model, Case 7)
Figure 7. Continued.

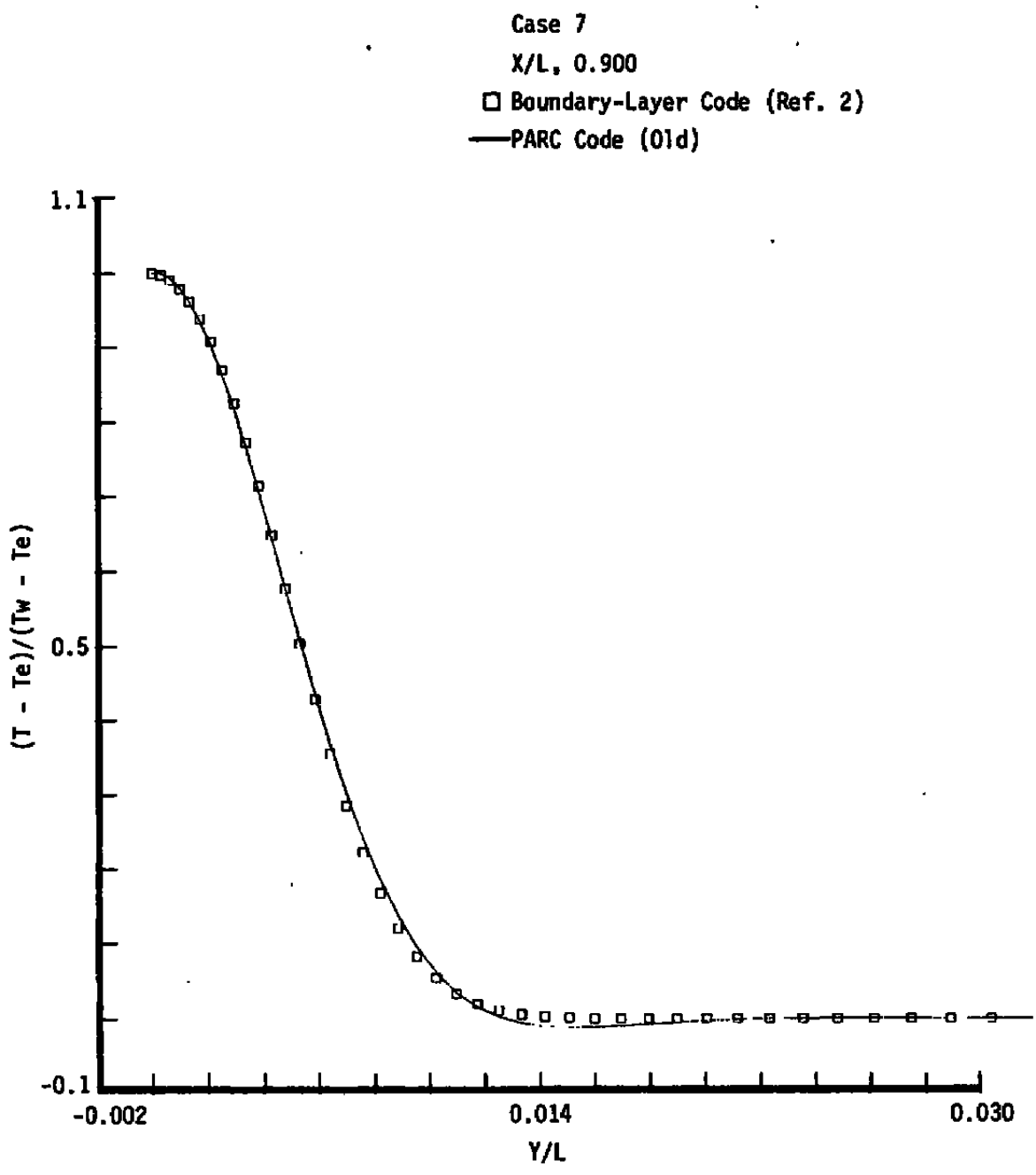

c. Temperature profile (old model, Case 7)
Figure 7. Continued.

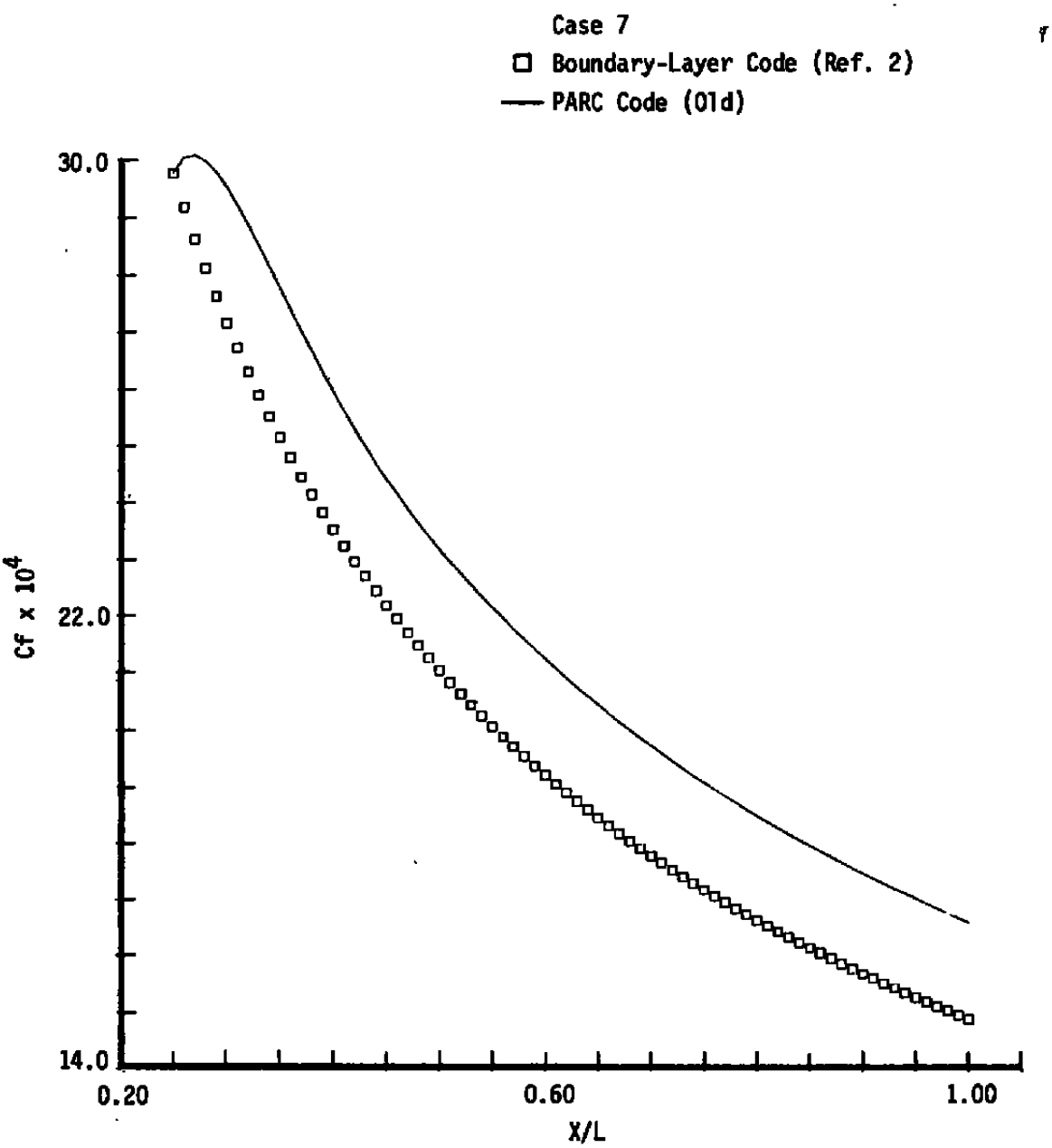

d. Skin friction variation (old model, Case 7)
Figure 7. Concluded.

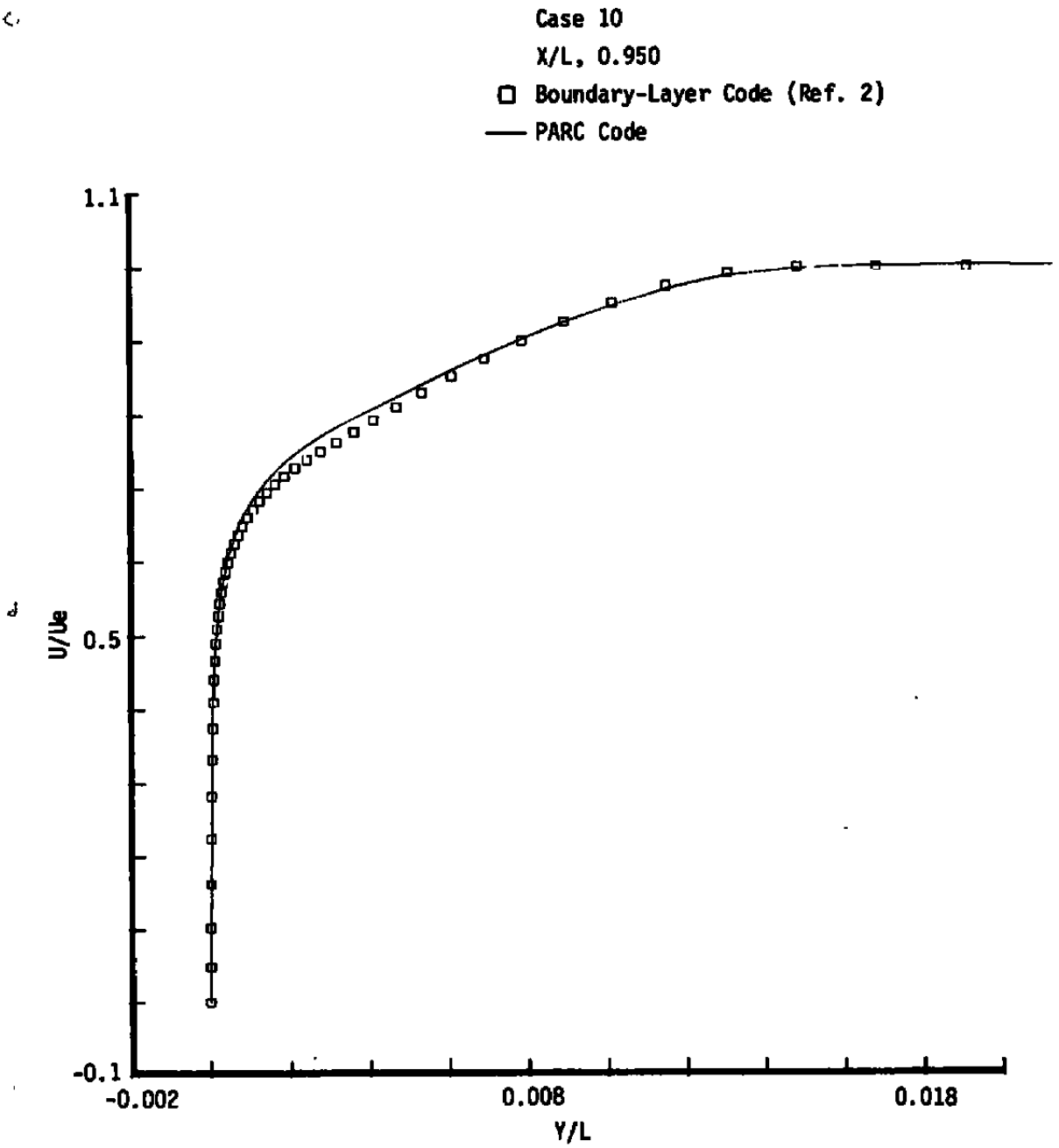

a. Velocity profile (edge scaling)

Figure 8. Transonic turbulent flat-plate flow comparisons.

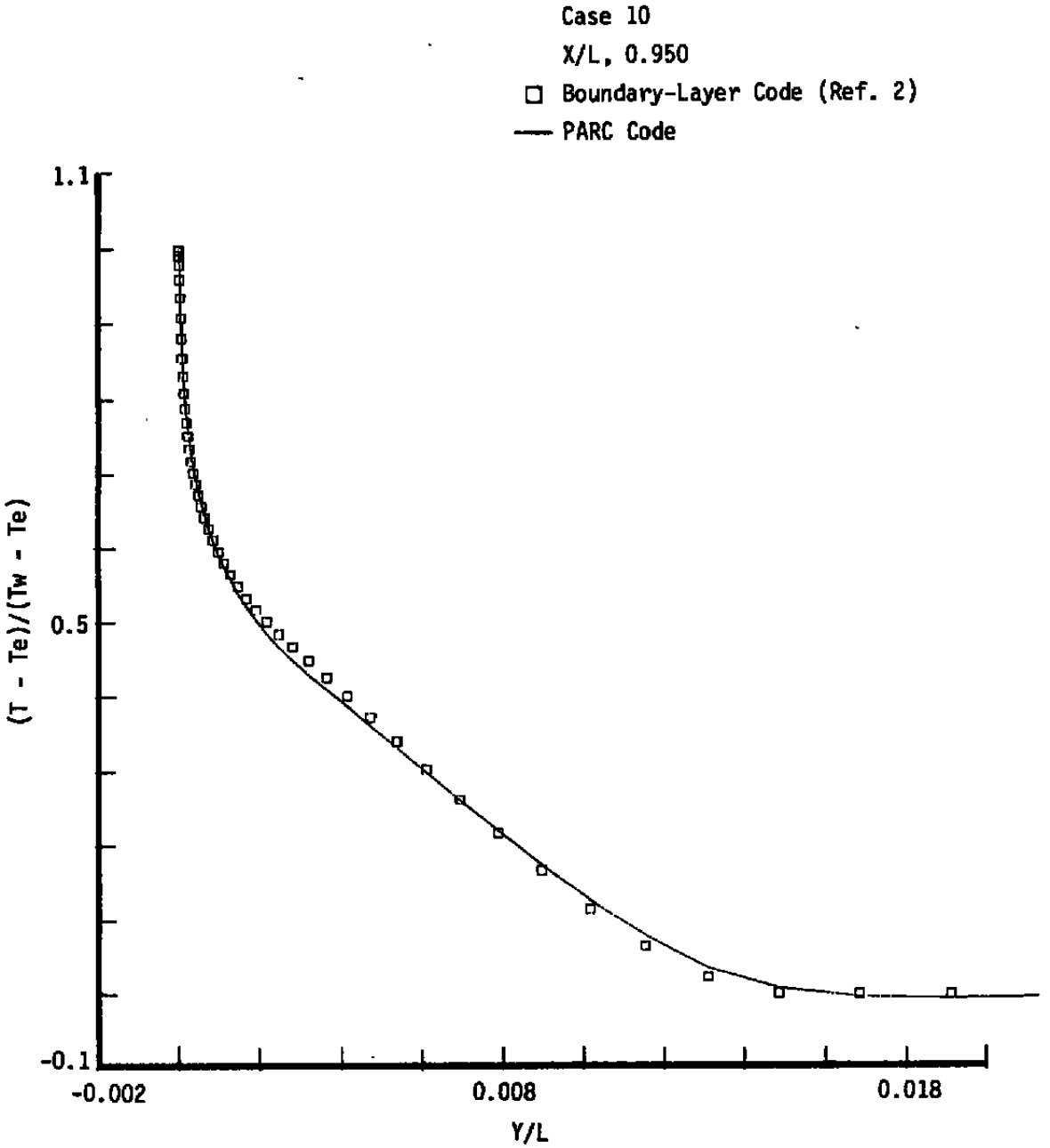

b. Temperature profile (edge scaling)
Figure 8. Continued.

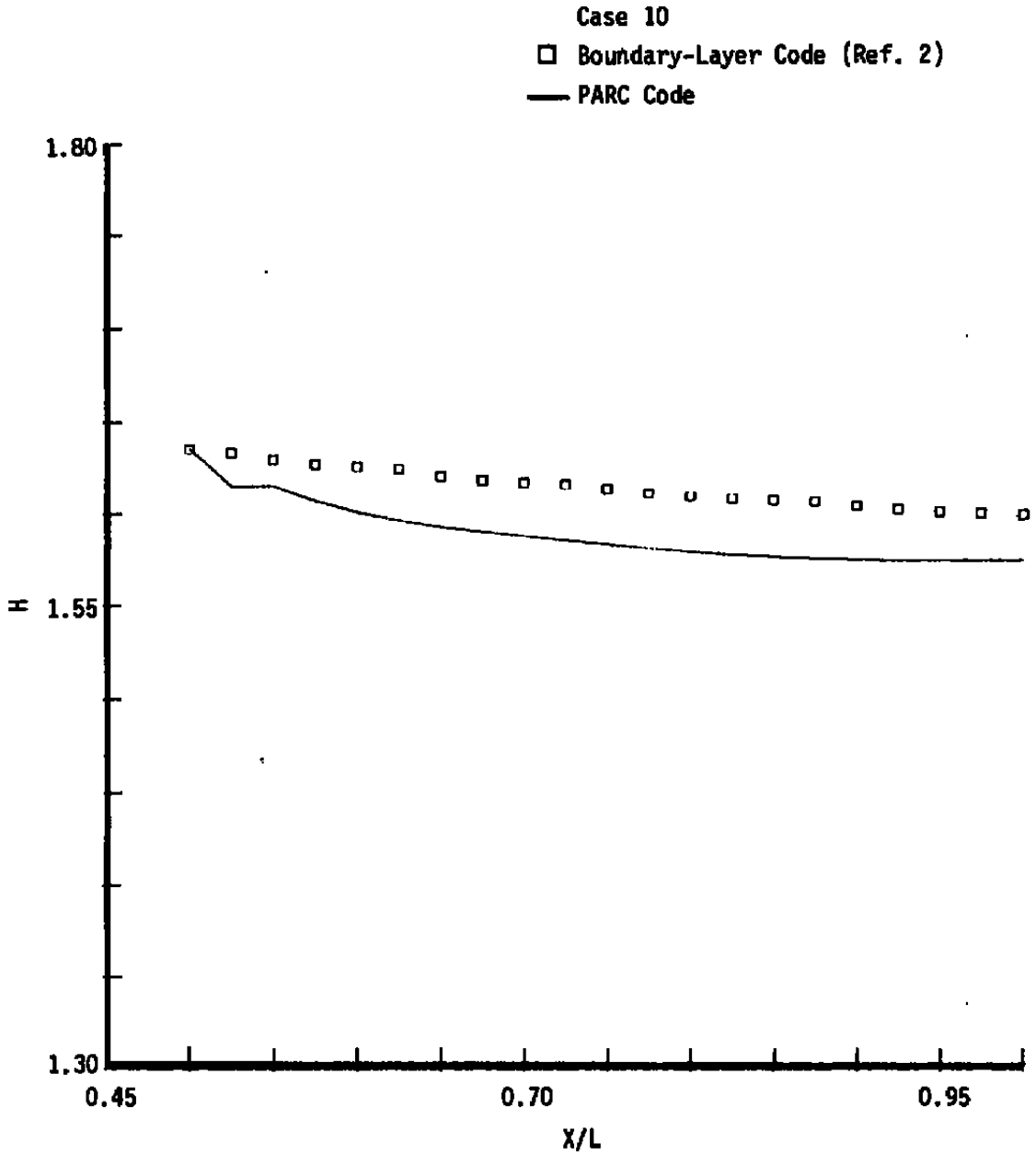

c. Shape factor streamwise variation
Figure 8. Continued.

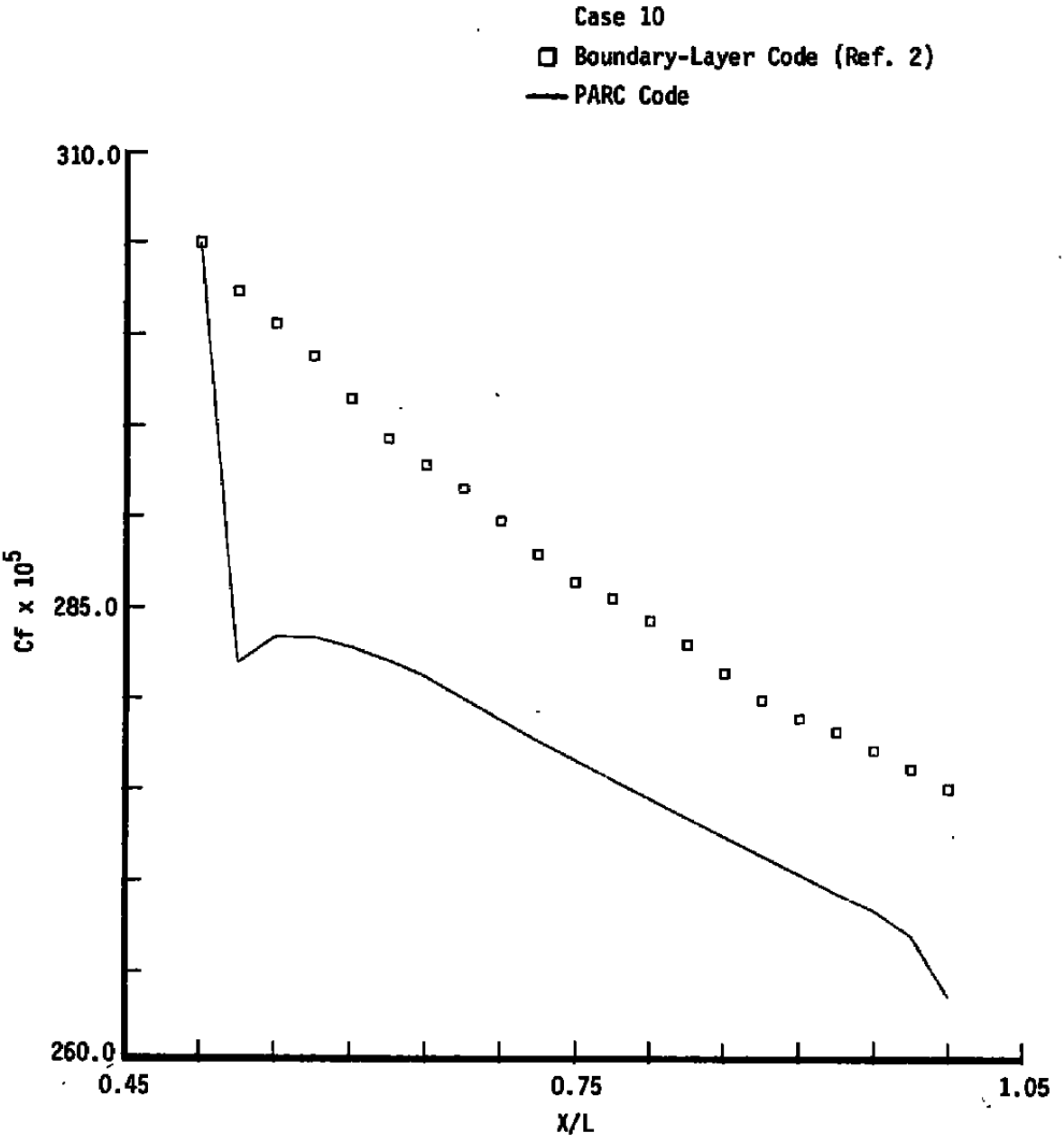

d. Skin friction streamwise variation
Figure 8. Continued.

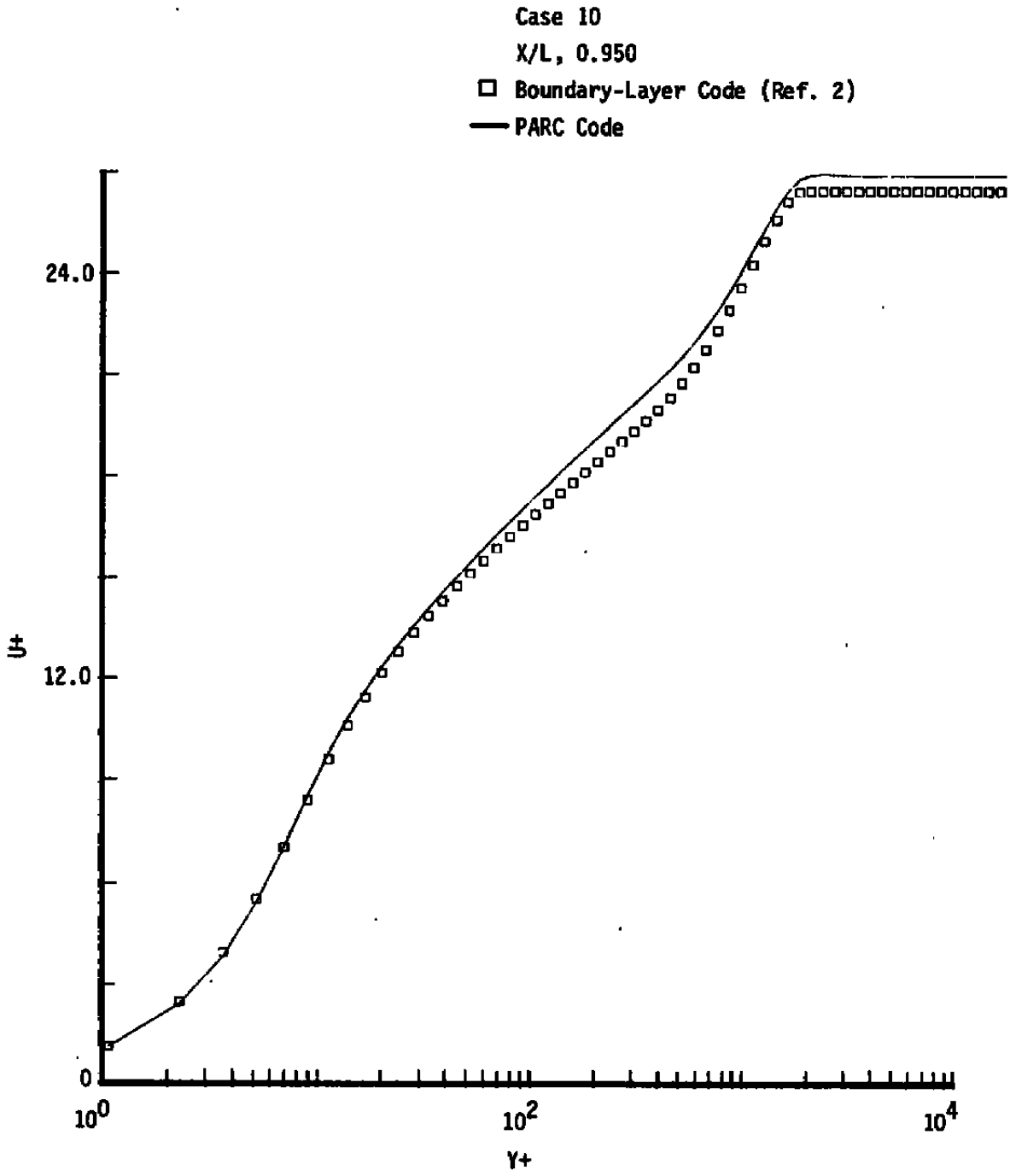

e. Velocity profile (wall scaling)
Figure 8. Concluded.

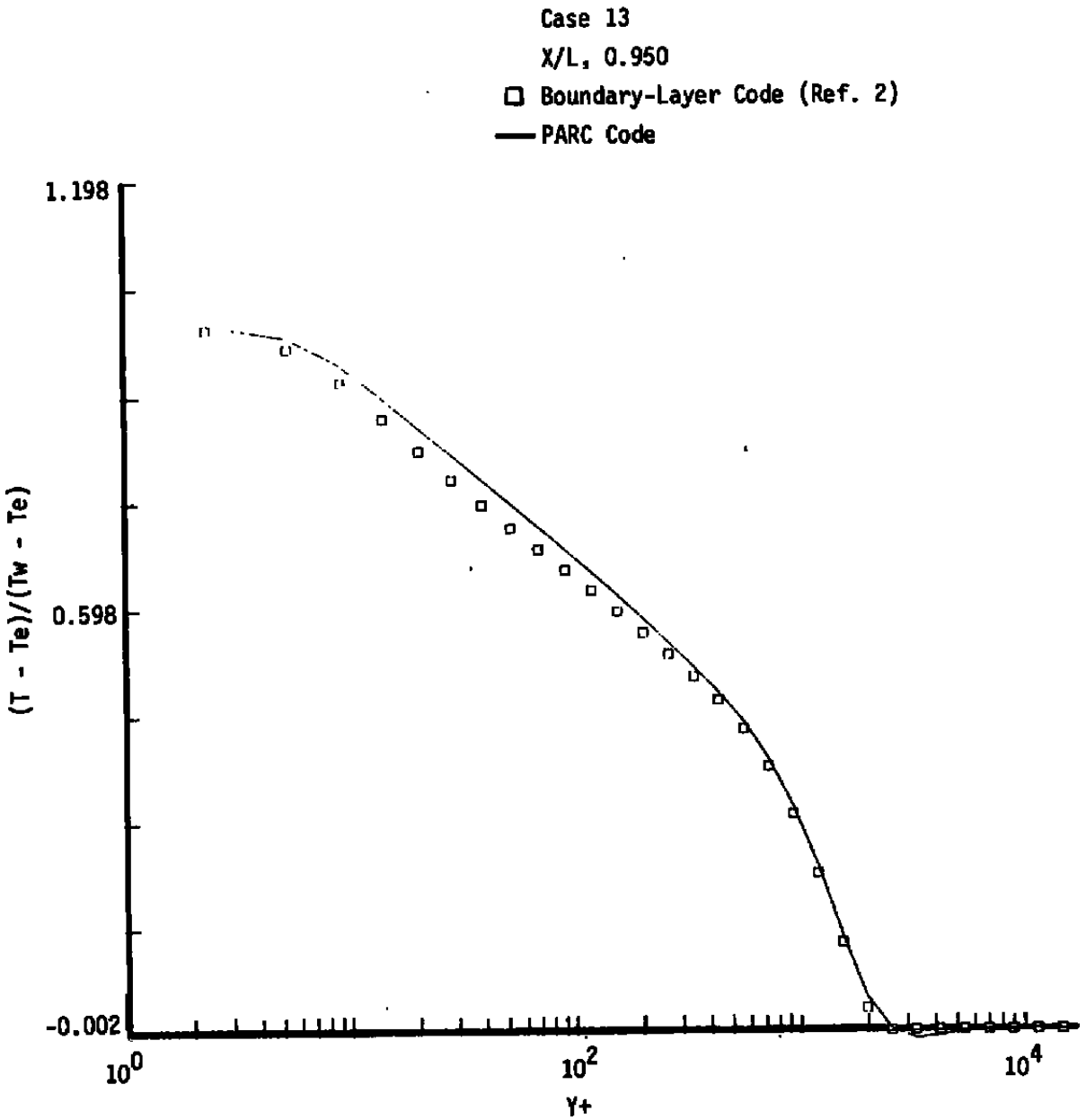

a. Sparse grid temperature profile (wall scaling, Case 13)

Figure 9. Grid density effects on turbulent flat-plate comparisons.

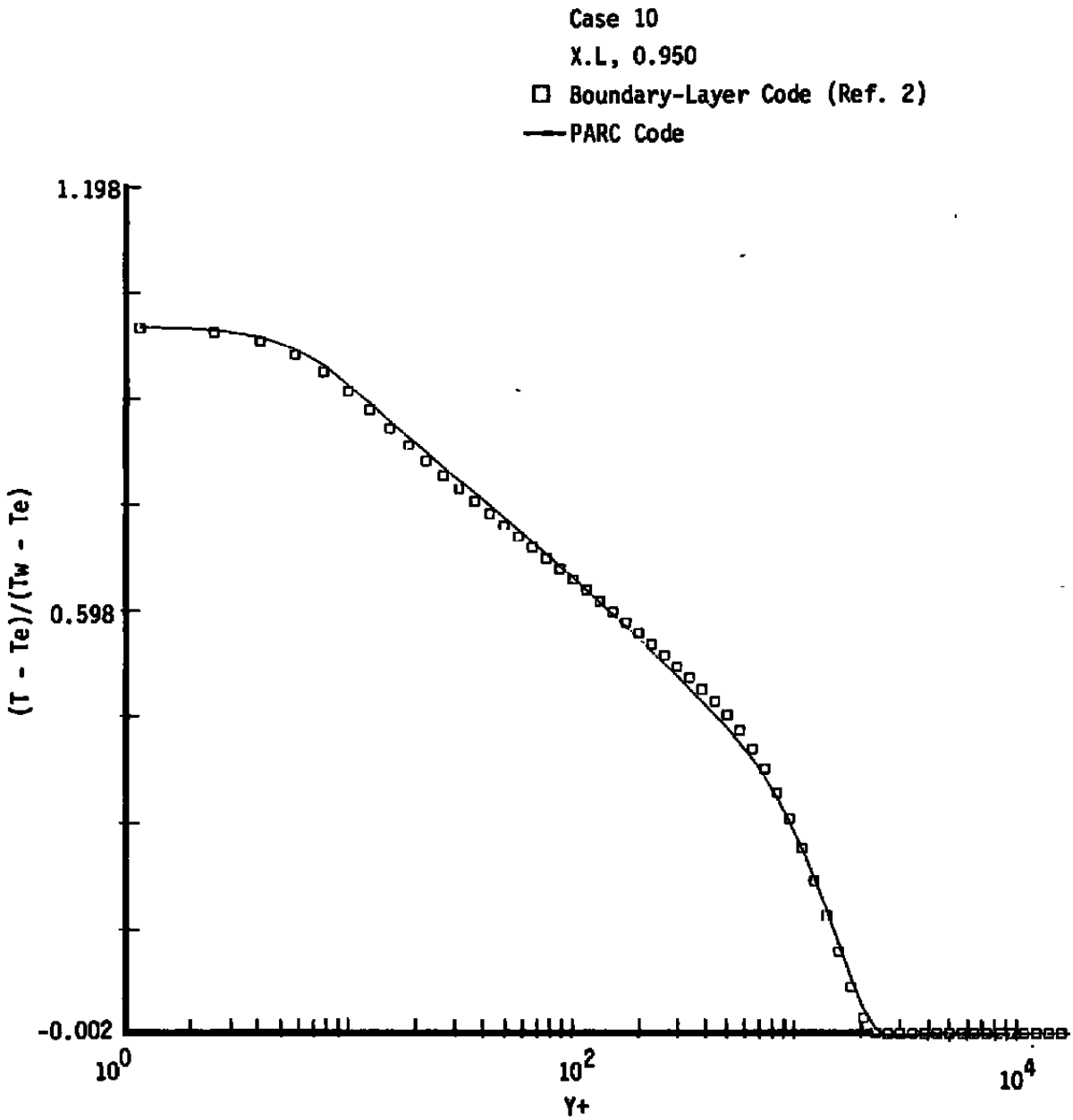

b. Medium grid temperature profile (wall scaling, Case 10)
Figure 9. Continued.

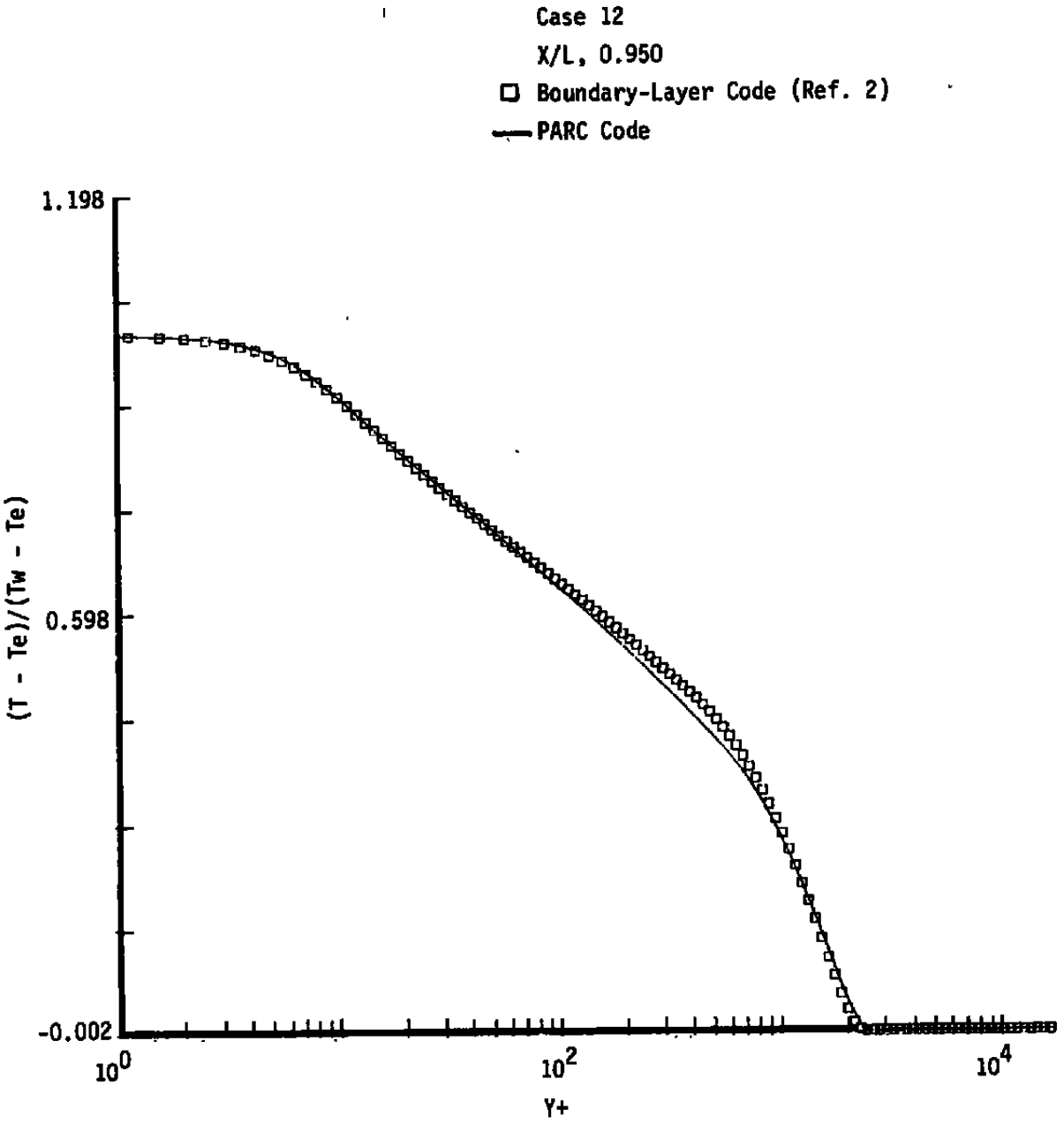

c. Dense grid temperature profile (wall scaling, Case 12)
Figure 9. Concluded.

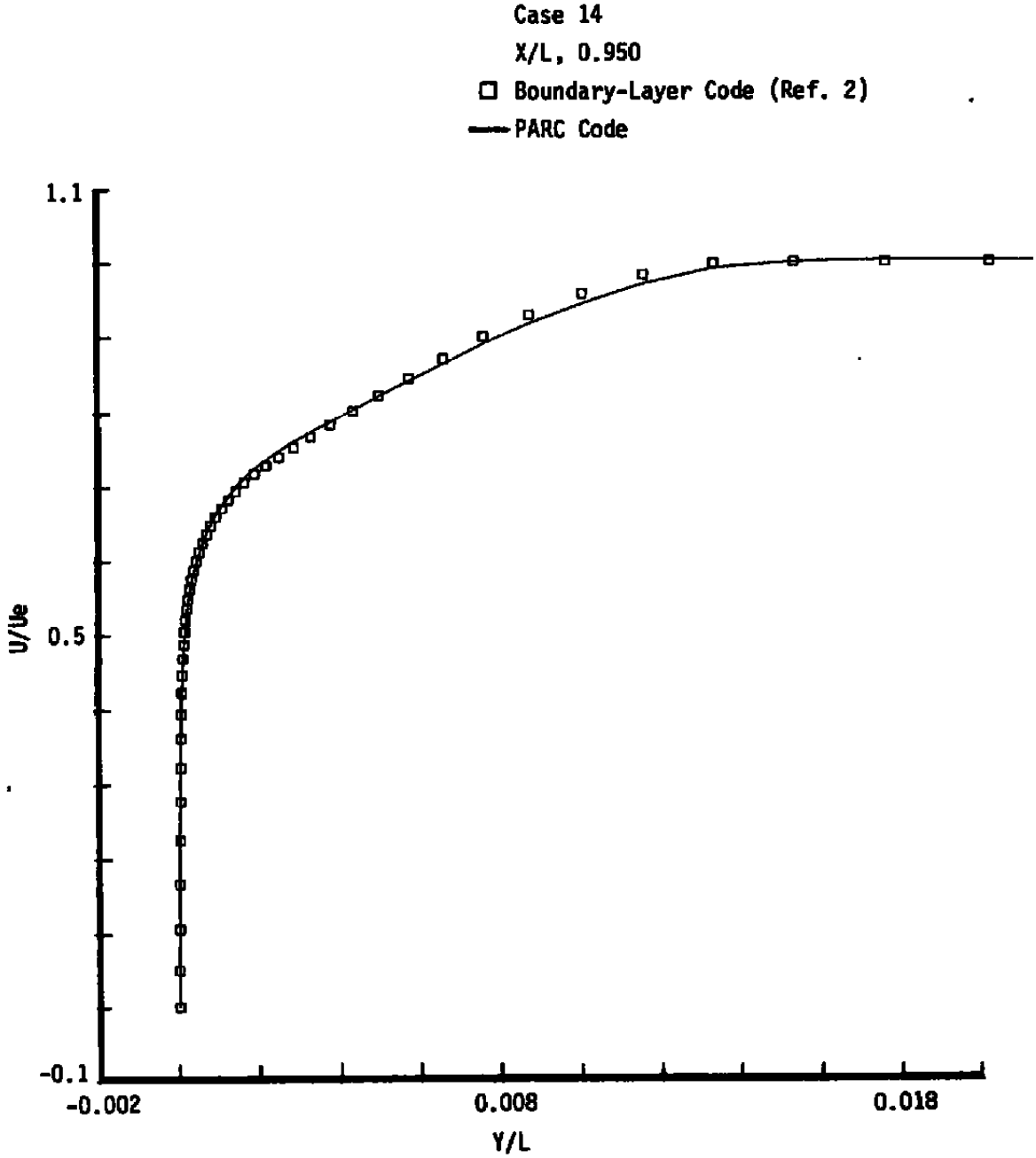

a. Velocity profile (edge scaling)

Figure 10. Cold-Wall comparisons for turbulent flat-plate flow.

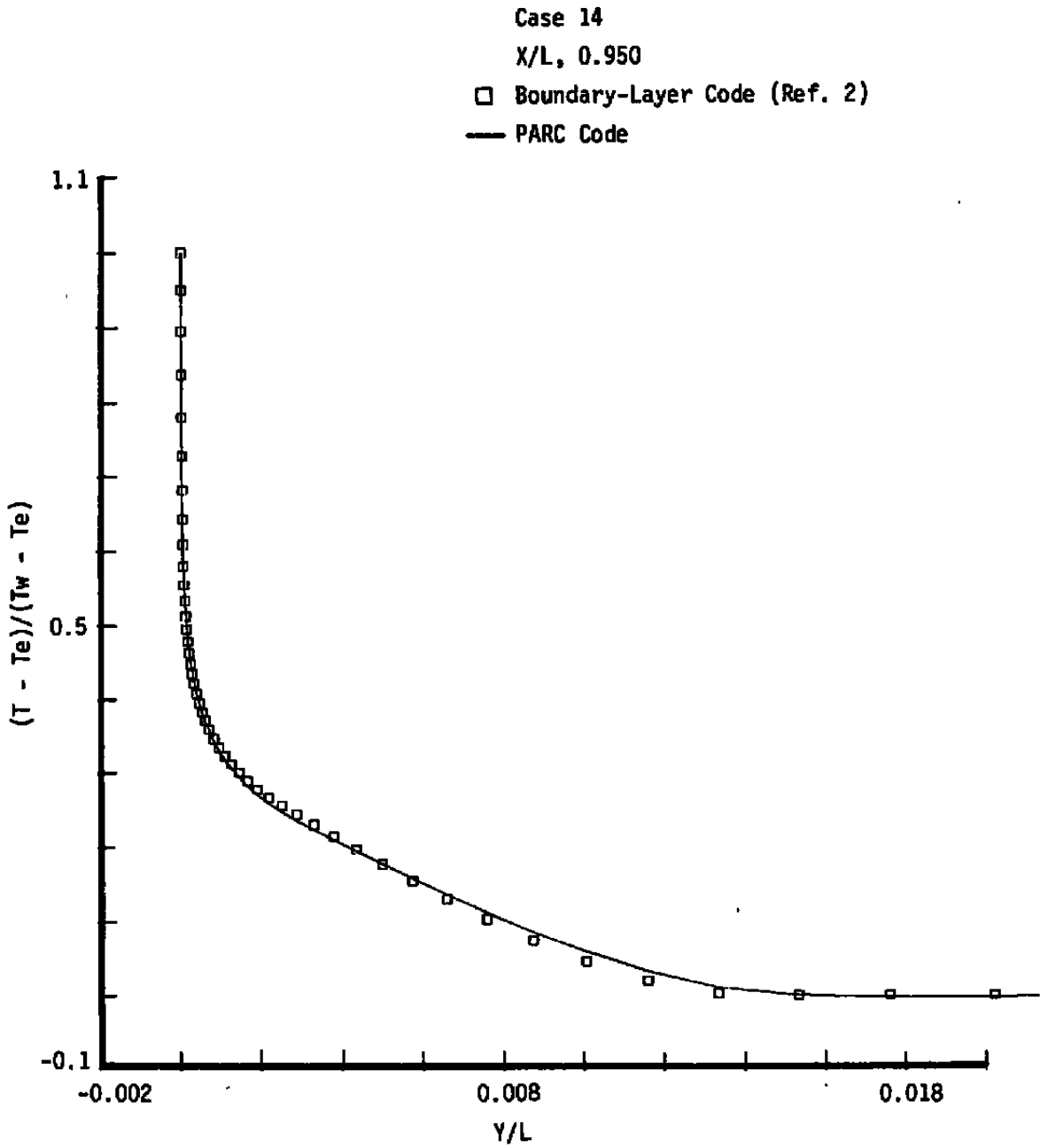

b. Temperature profile (edge scaling)
Figure 10. Continued.

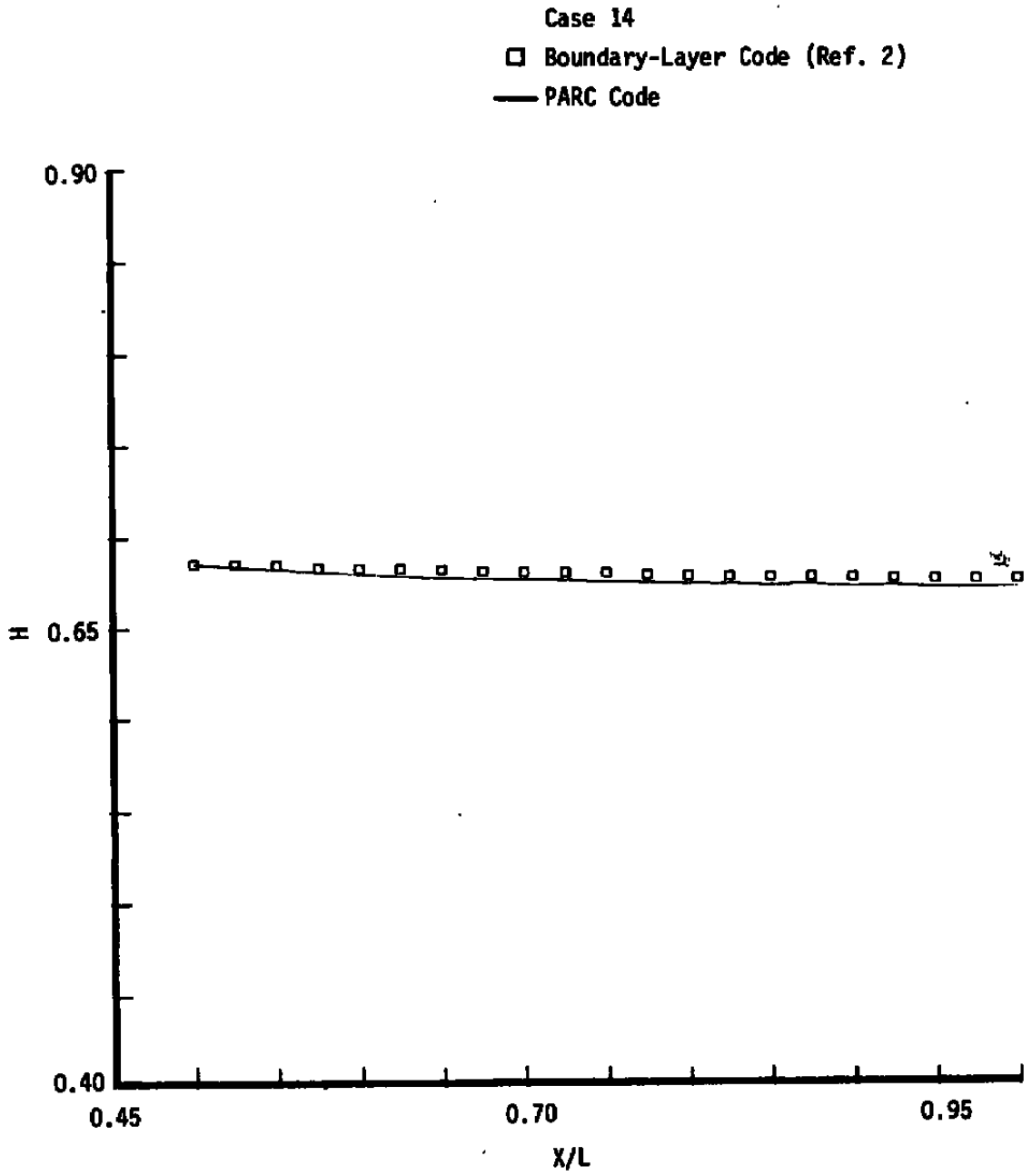

c. Shape factor streamwise variation
Figure 10. Continued.

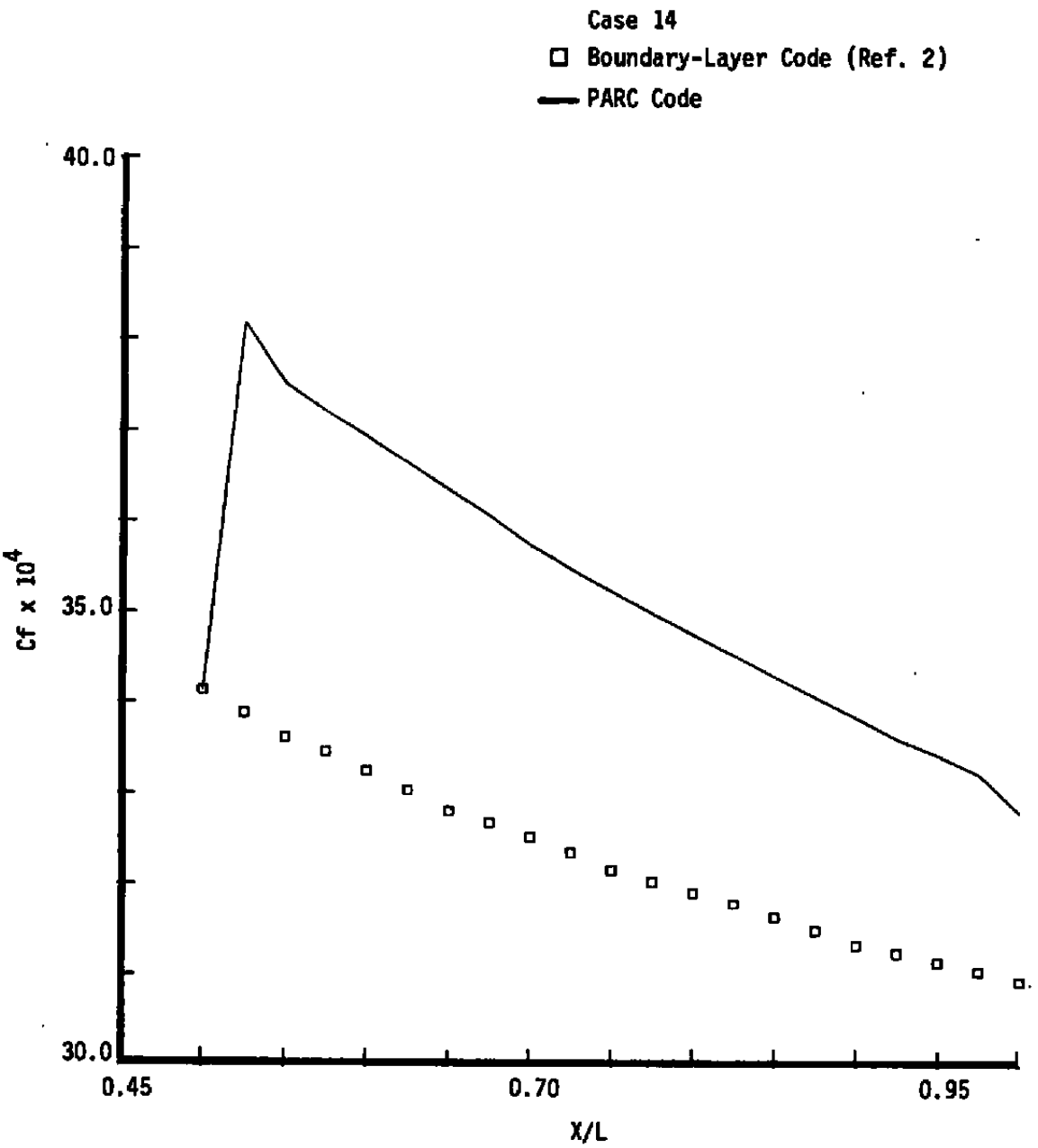

d. Skin friction streamwise variation
Figure 10. Continued.

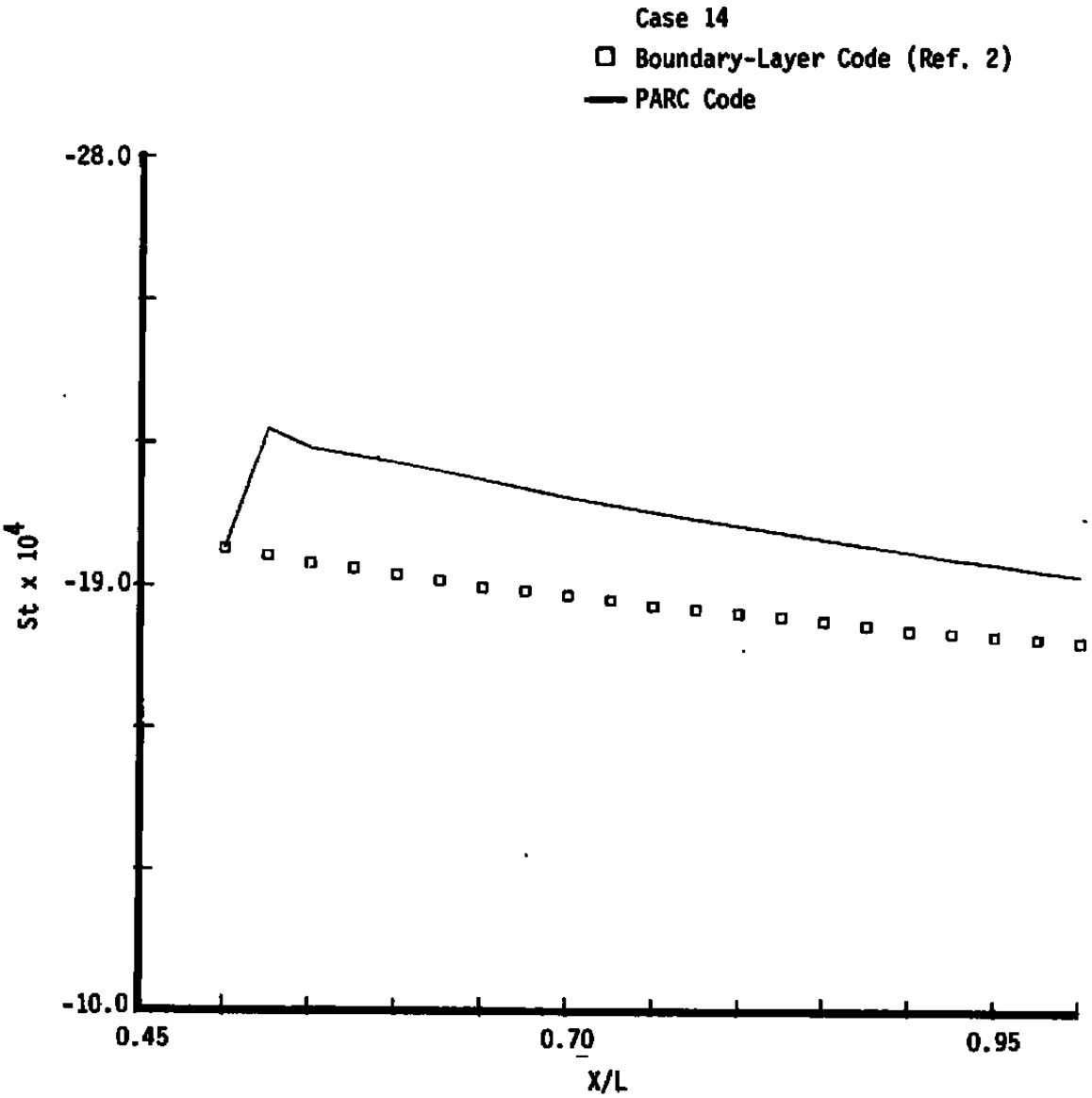

e. Stanton number streamwise variation

Figure 10. Continued.

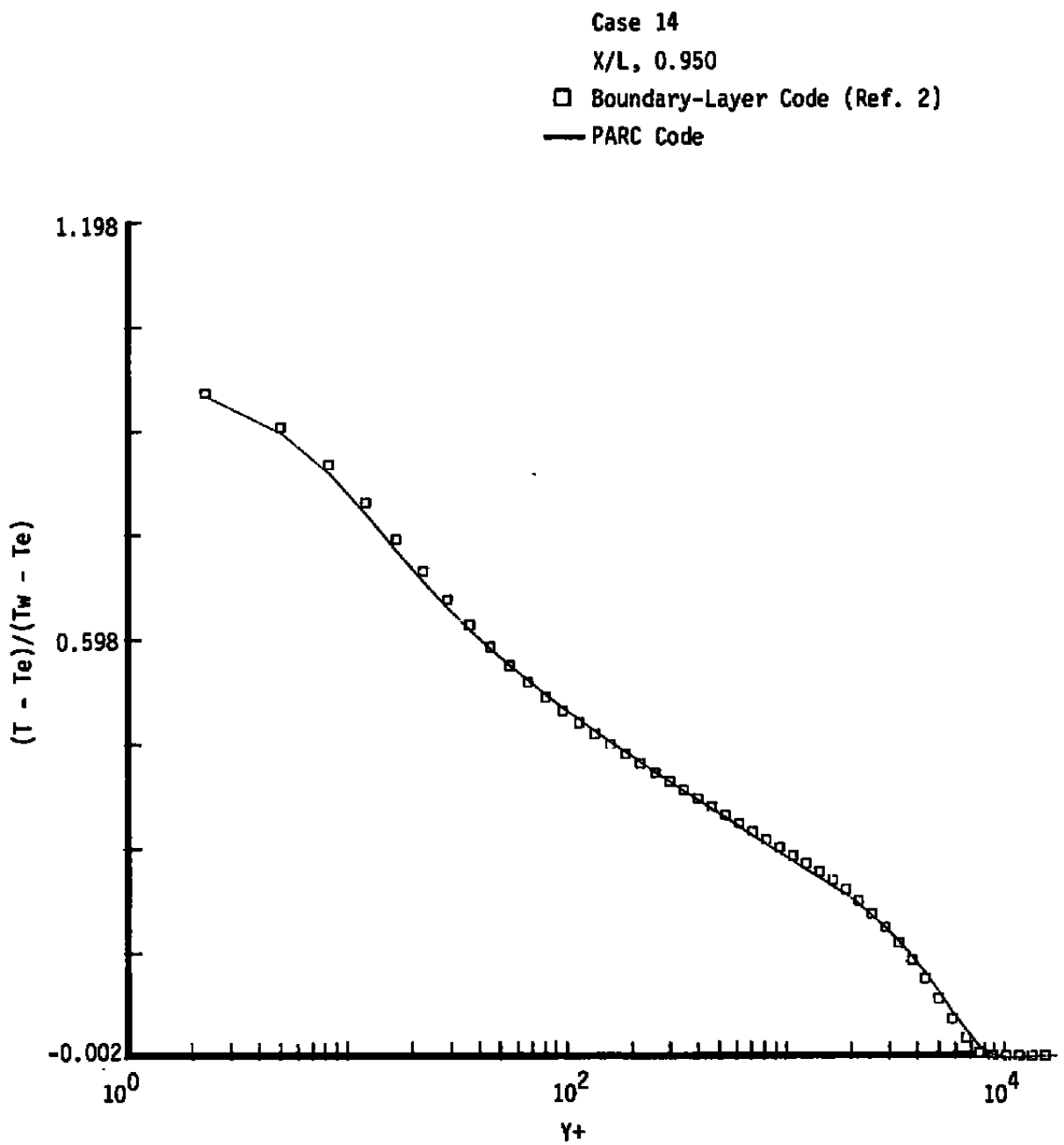

f. Temperature profile (wall scaling)
Figure 10. Concluded.

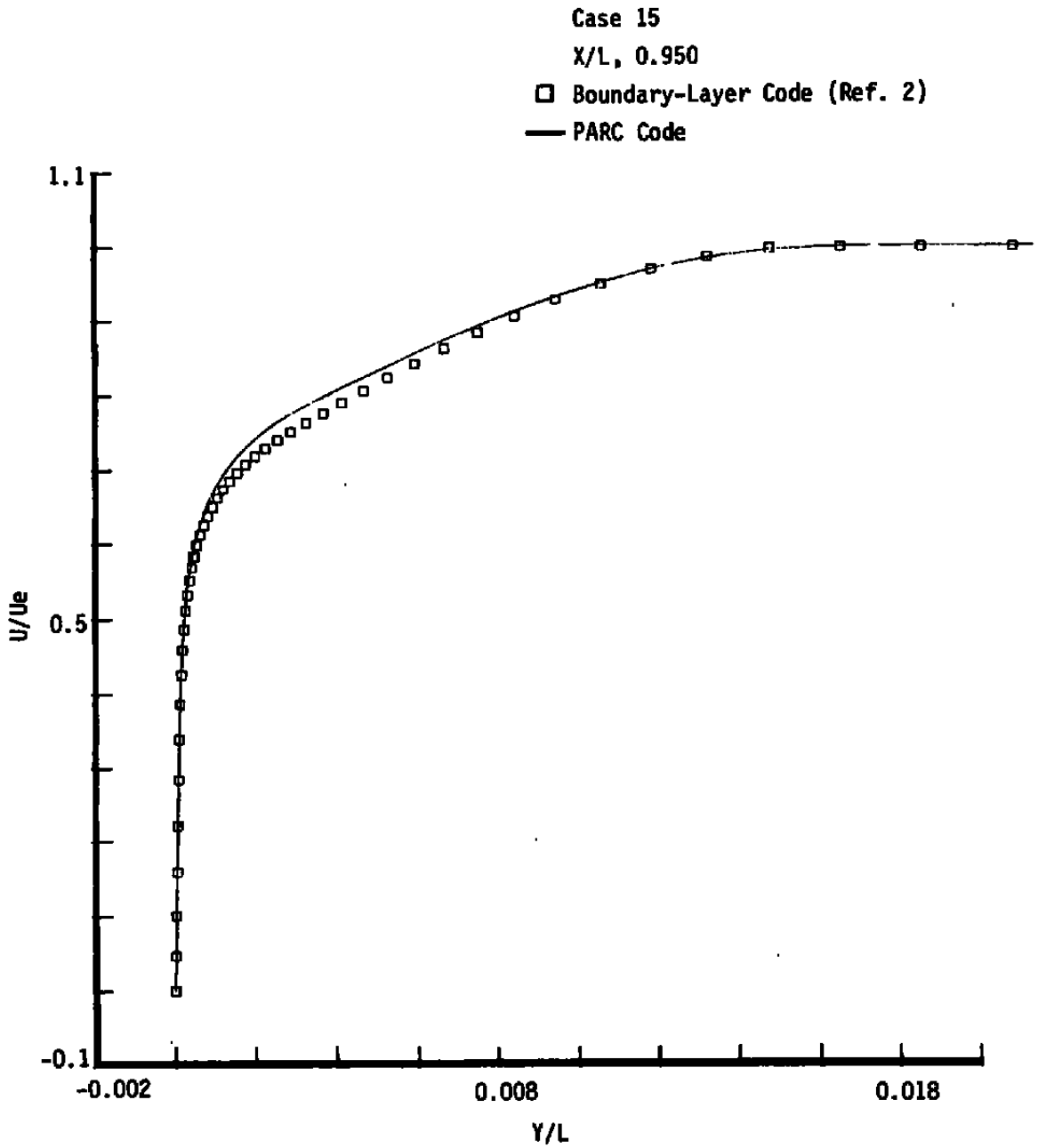

a. Velocity profile (edge scaling)

Figure 11. Hot-wall comparisons for turbulent flat-plate flow.

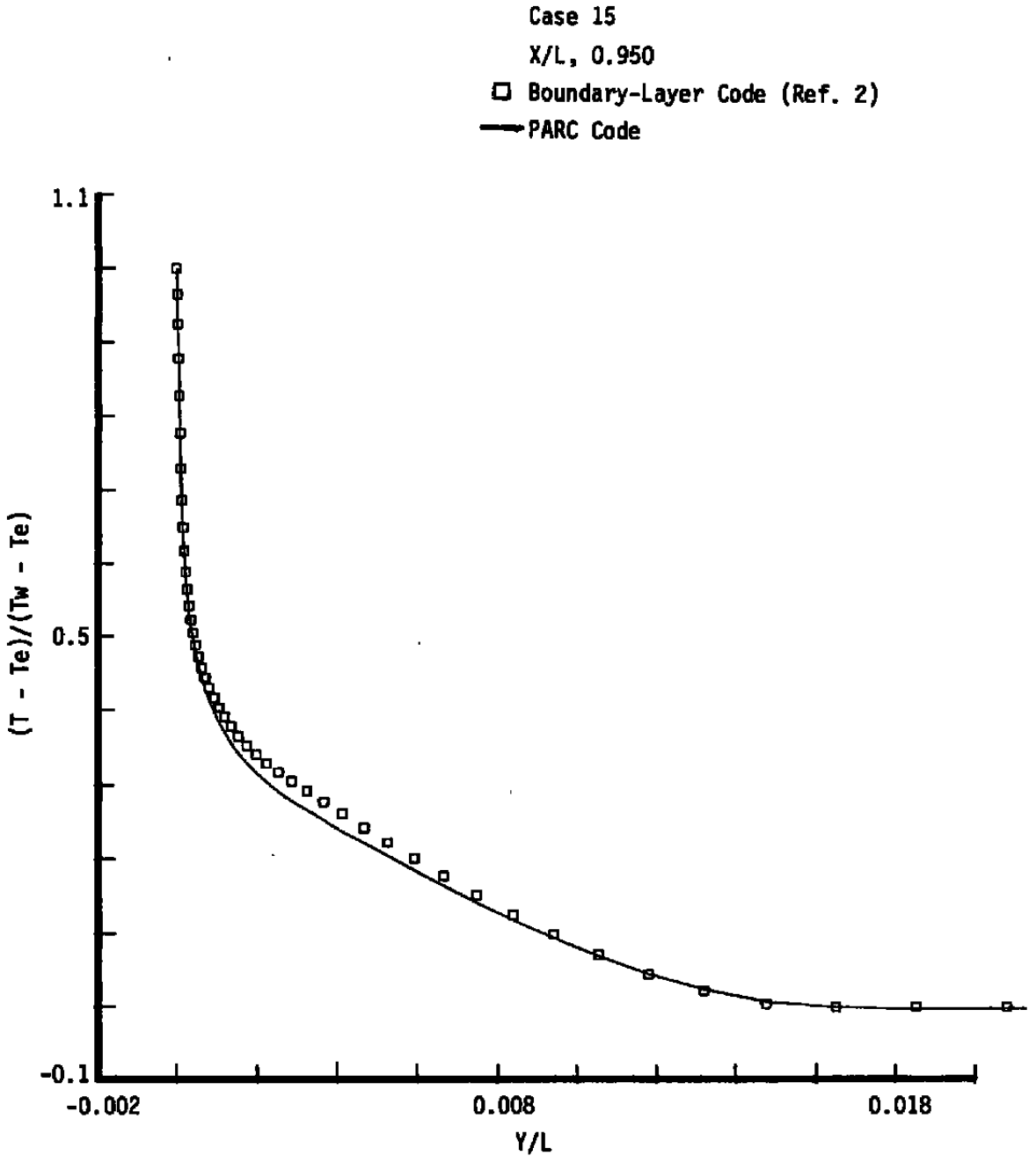

b. Temperature profile (edge scaling)
Figure 11. Continued.

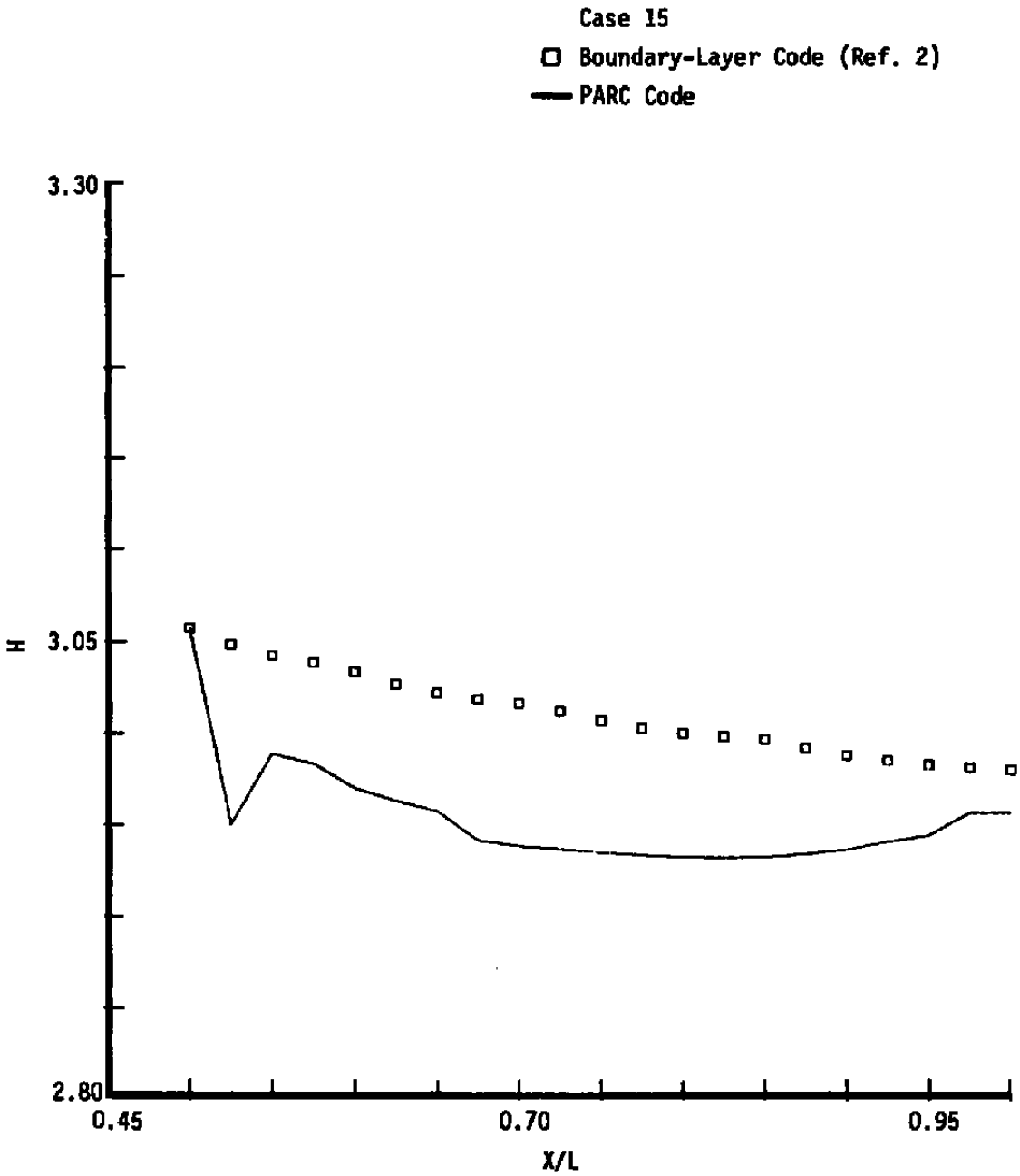

c. Shape factor streamwise variaiton
Figure 11. Continued.

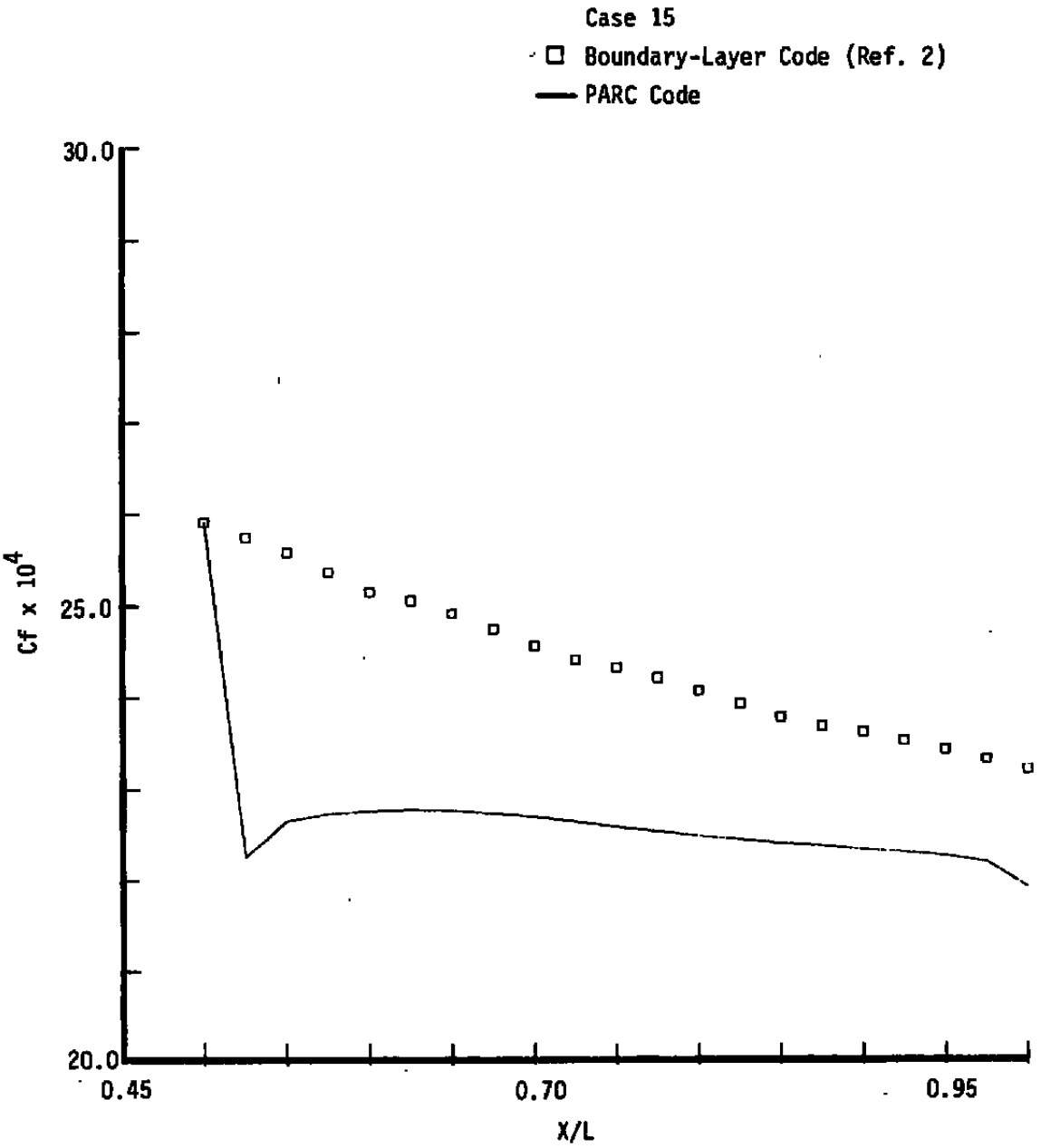

d. Skin friction streamwise variaiton
Figure 11. Continued.

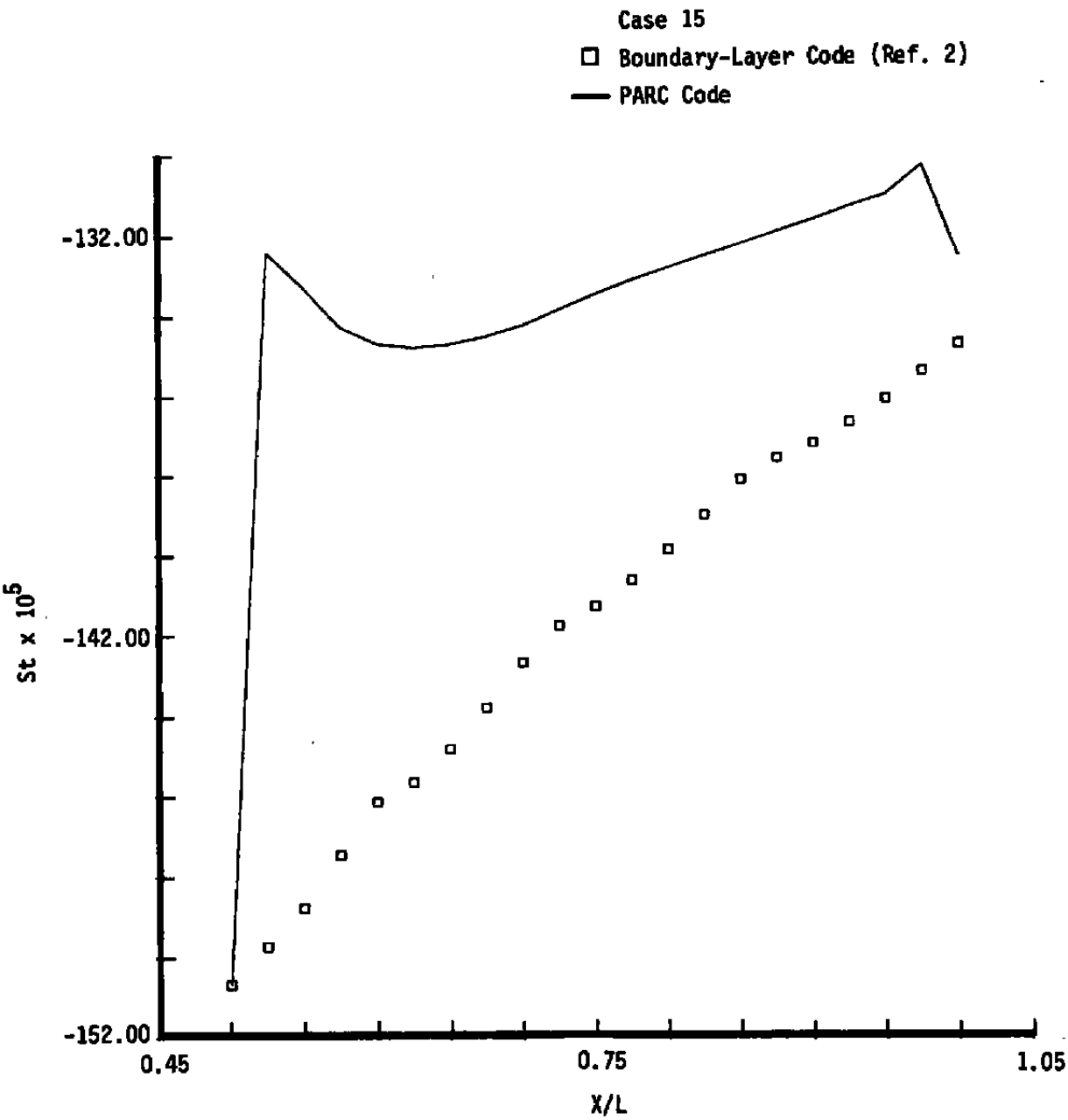

e. Stanton number streamwise variation

Figure 11. Continued.

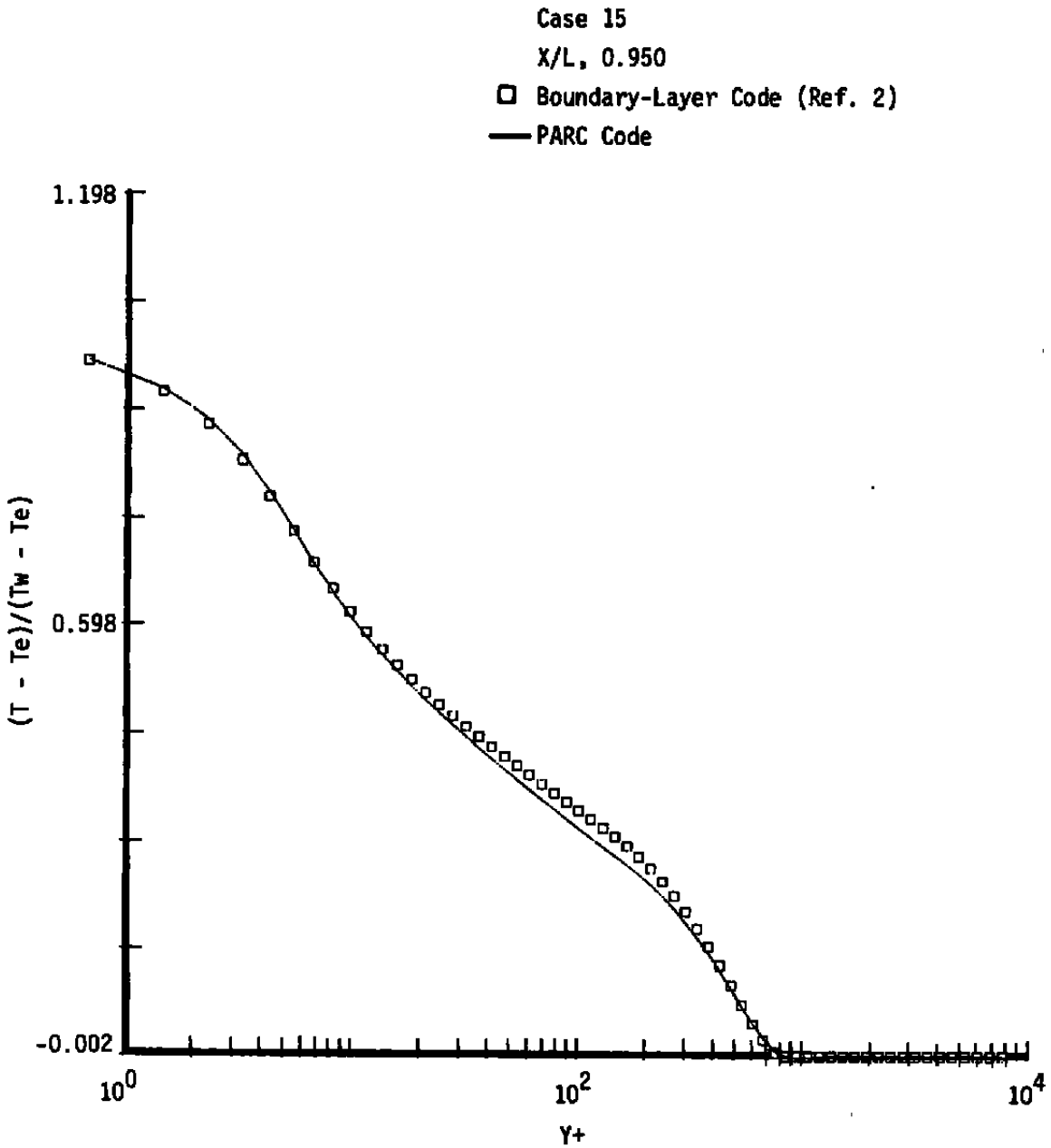

f. Temperature profile (wall scaling)
Figure 11. Concluded.

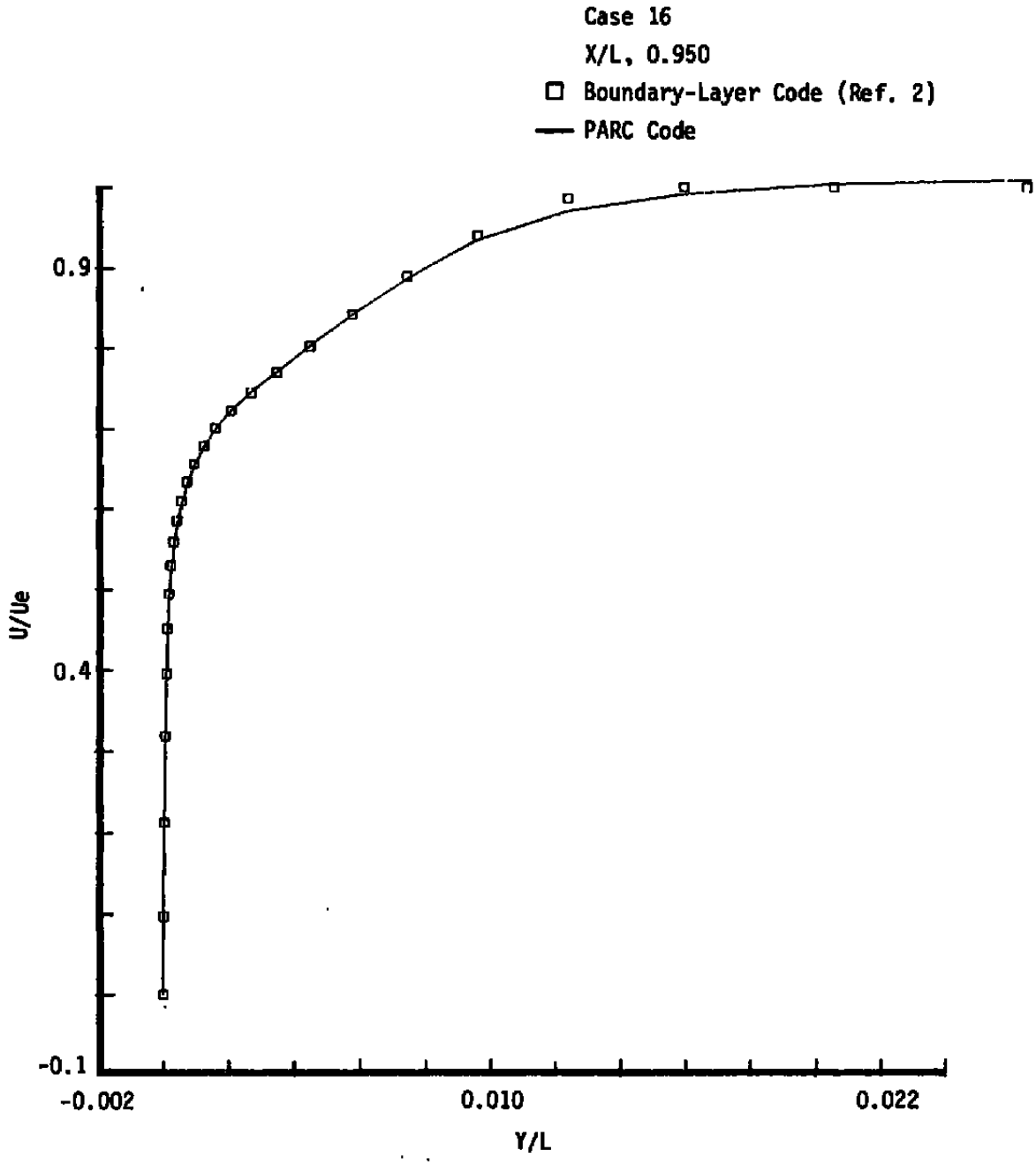

a. Velocity profile (edge scaling)

Figure 12. Subsonic turbulent flat-plate flow comparisons.

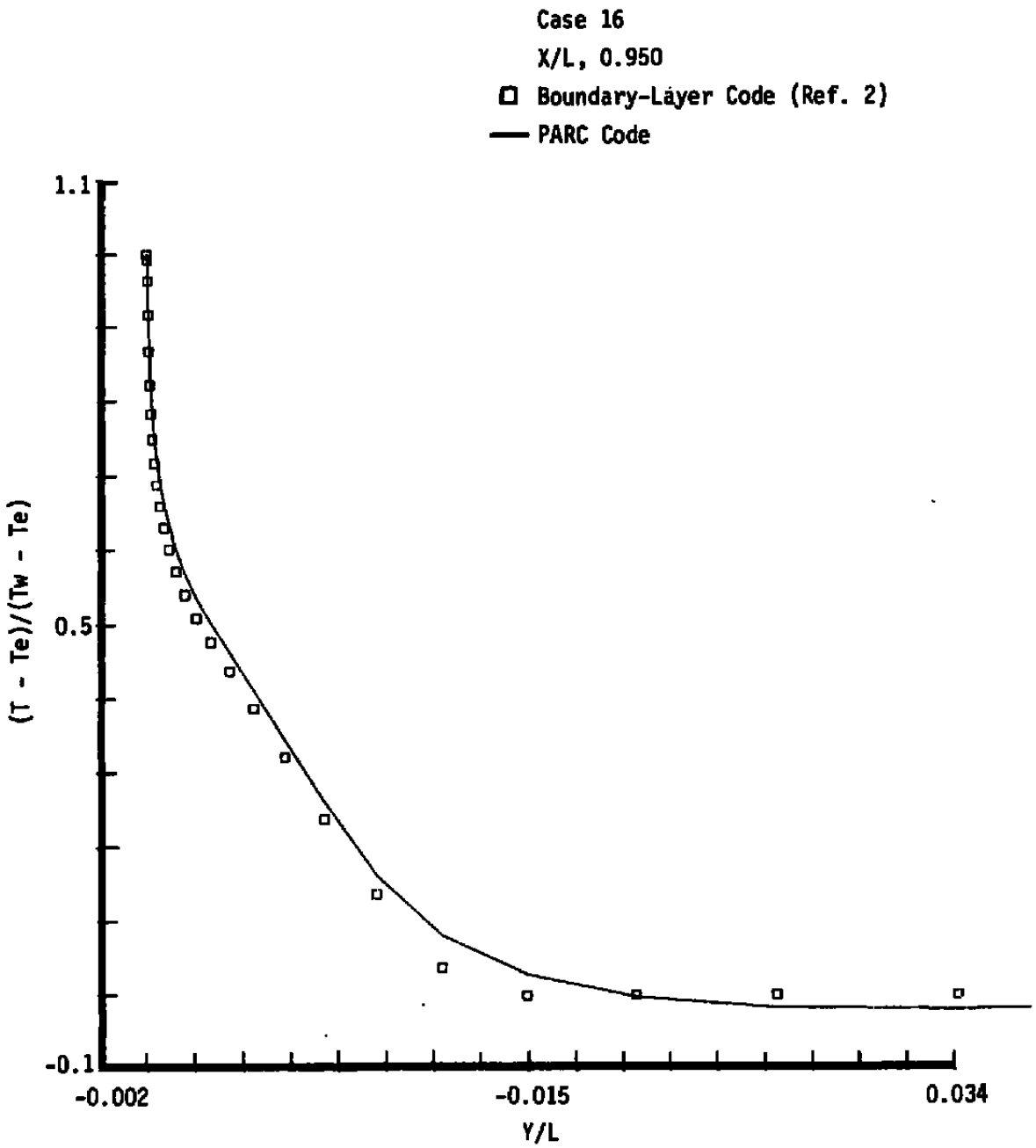

b. Temeprature profile (edge scaling)
Figure 12. Continued.

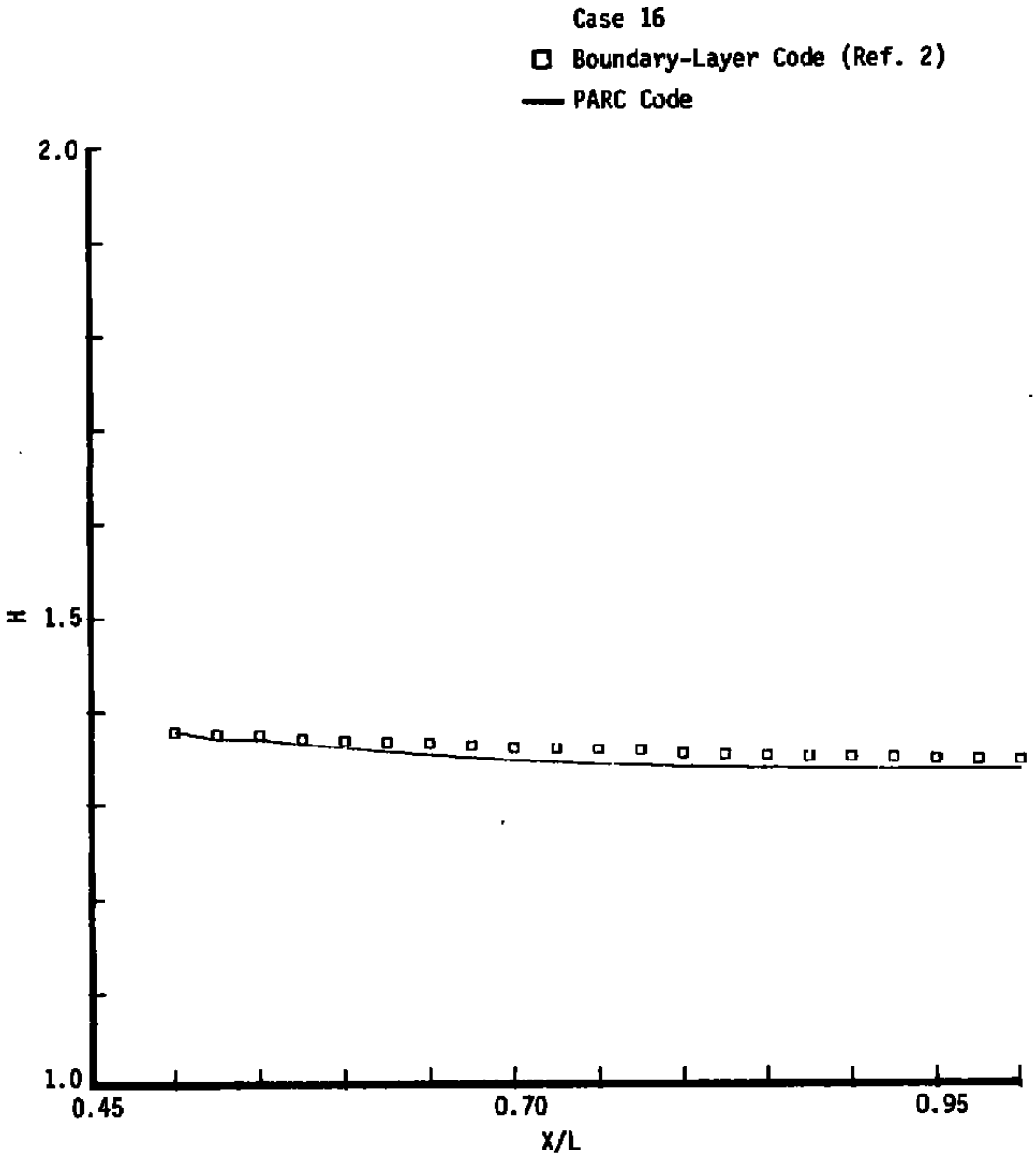

c. Shape factor streamwise variaiton
Figure 12. Continued.

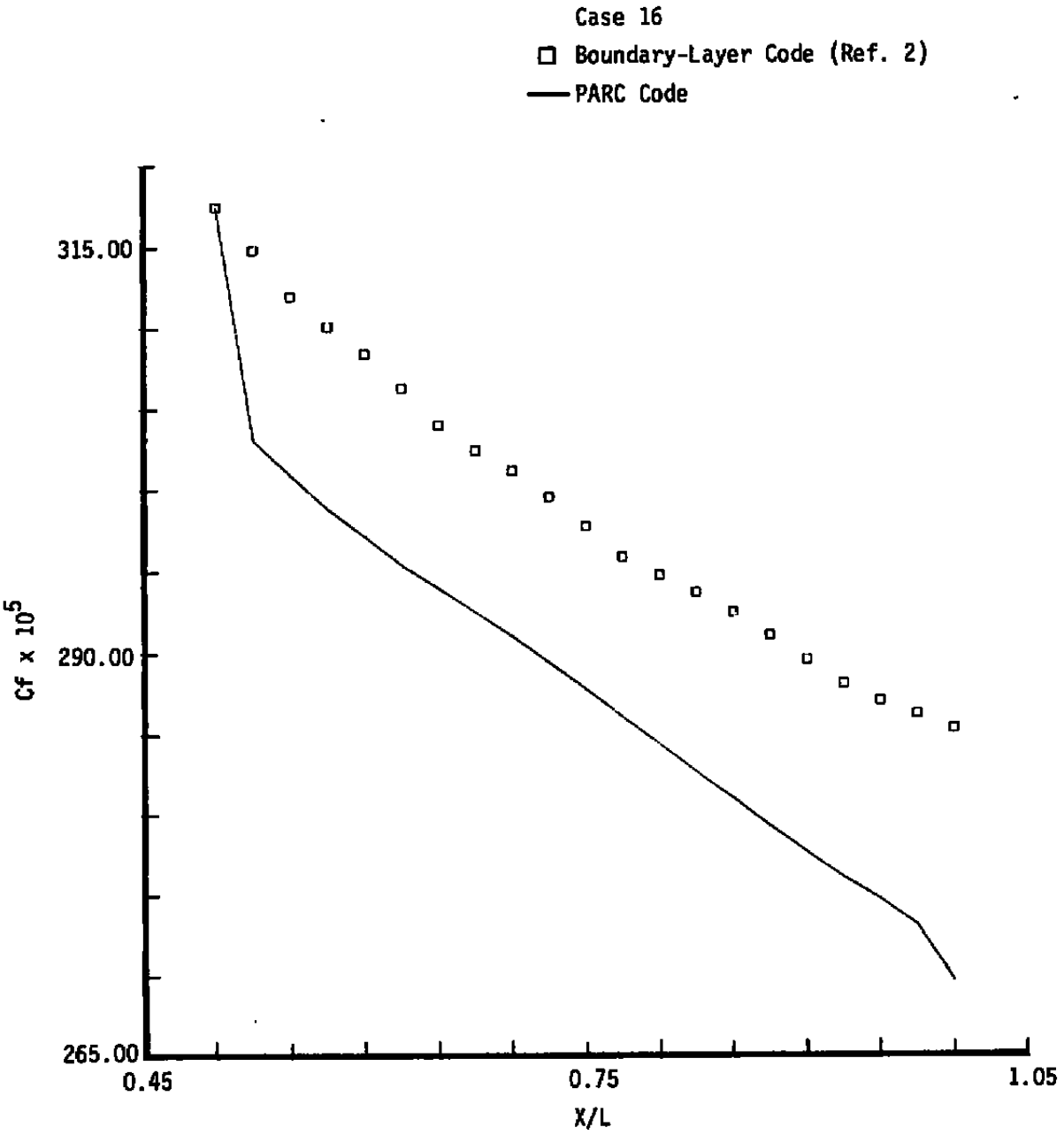

d. Skin friction streamwise variation

Figure 12. Continued.

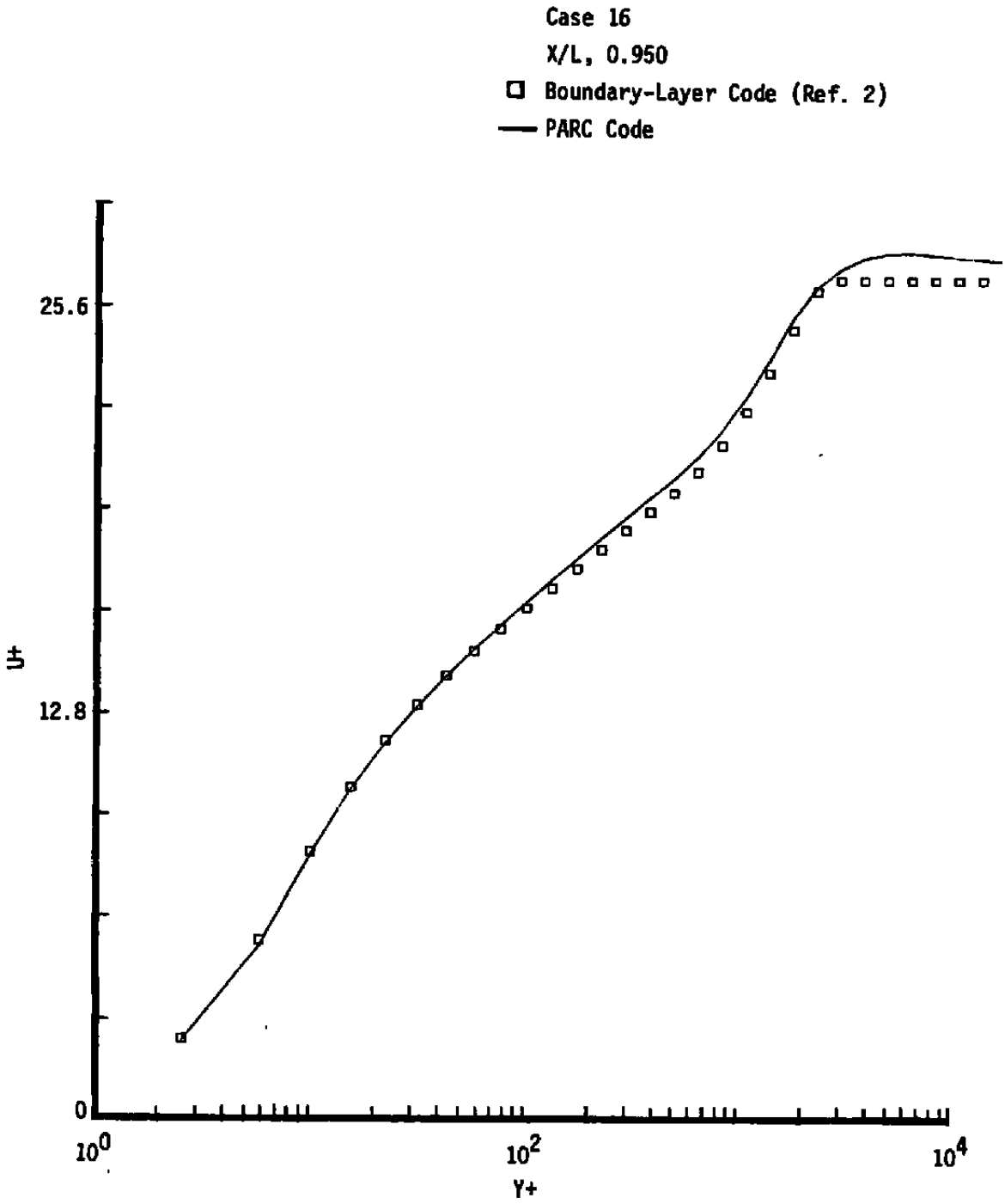

e. Velocity profile (wall scaling)
Figure 12. Continued.

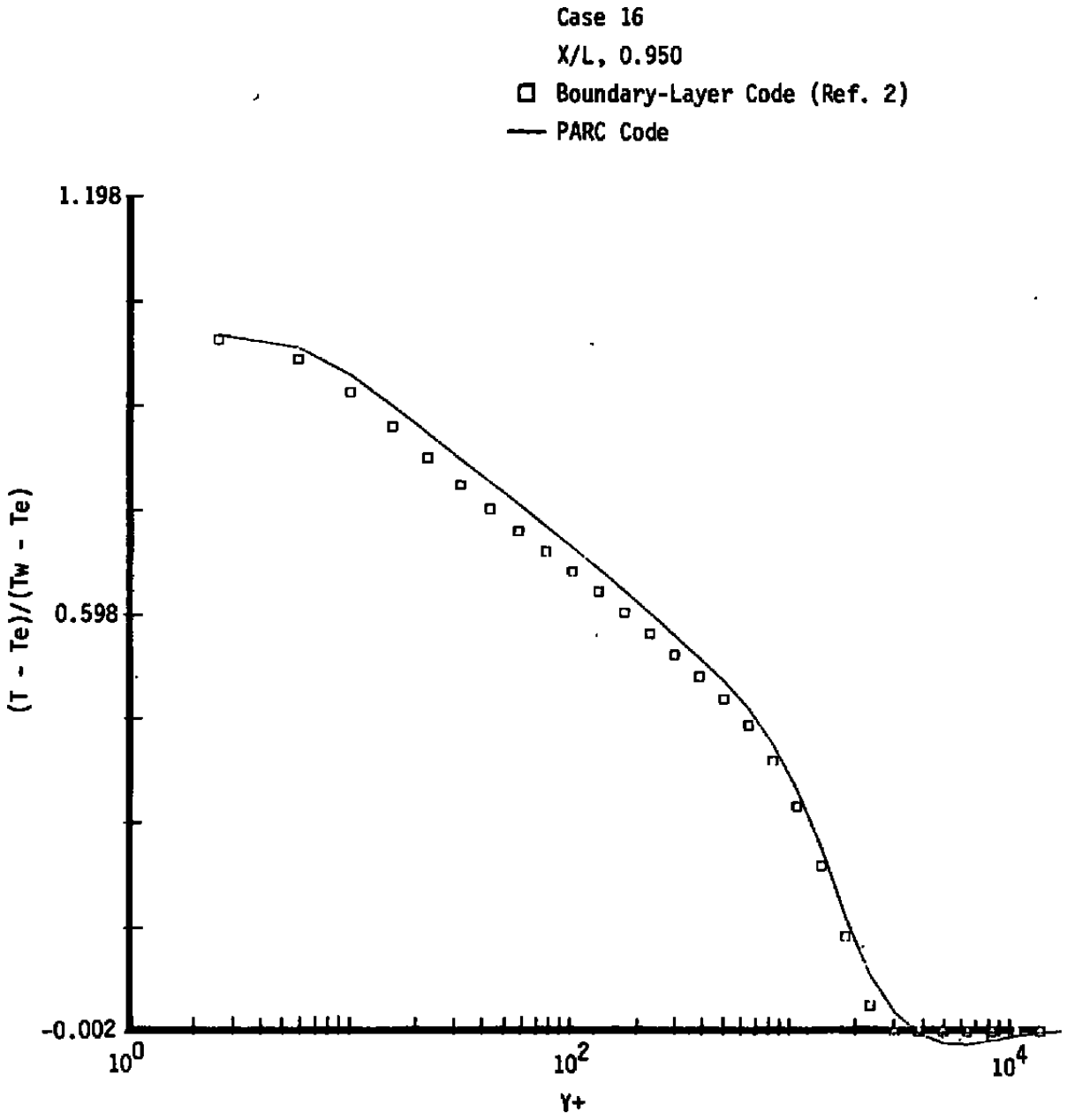

f. Temperature profile (wall scaling)
Figure 12. Concluded.

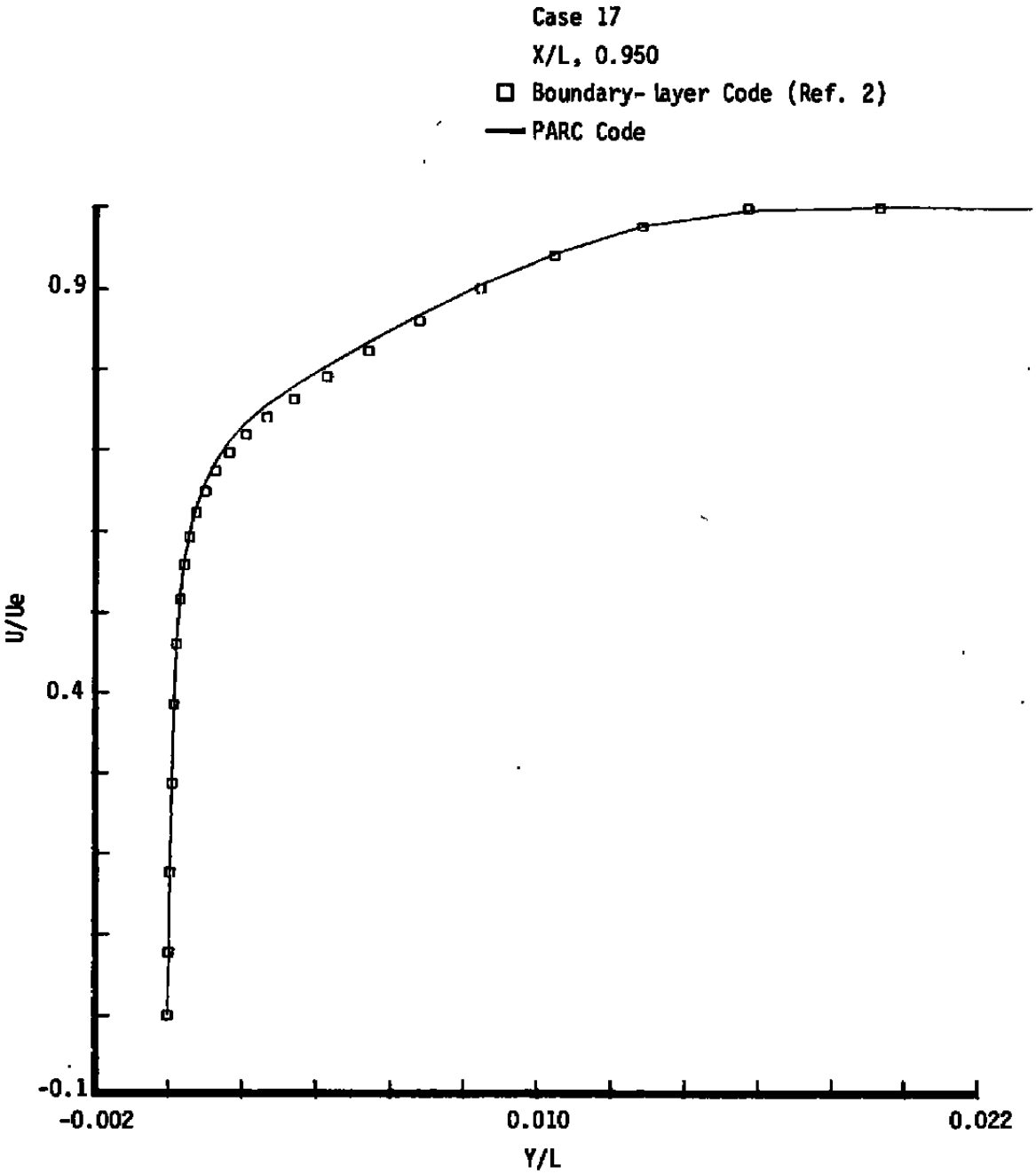

a. Velocity profile (edge scaling)

Figure 13. Supersonic turbulent flat-plate flow comparisons.

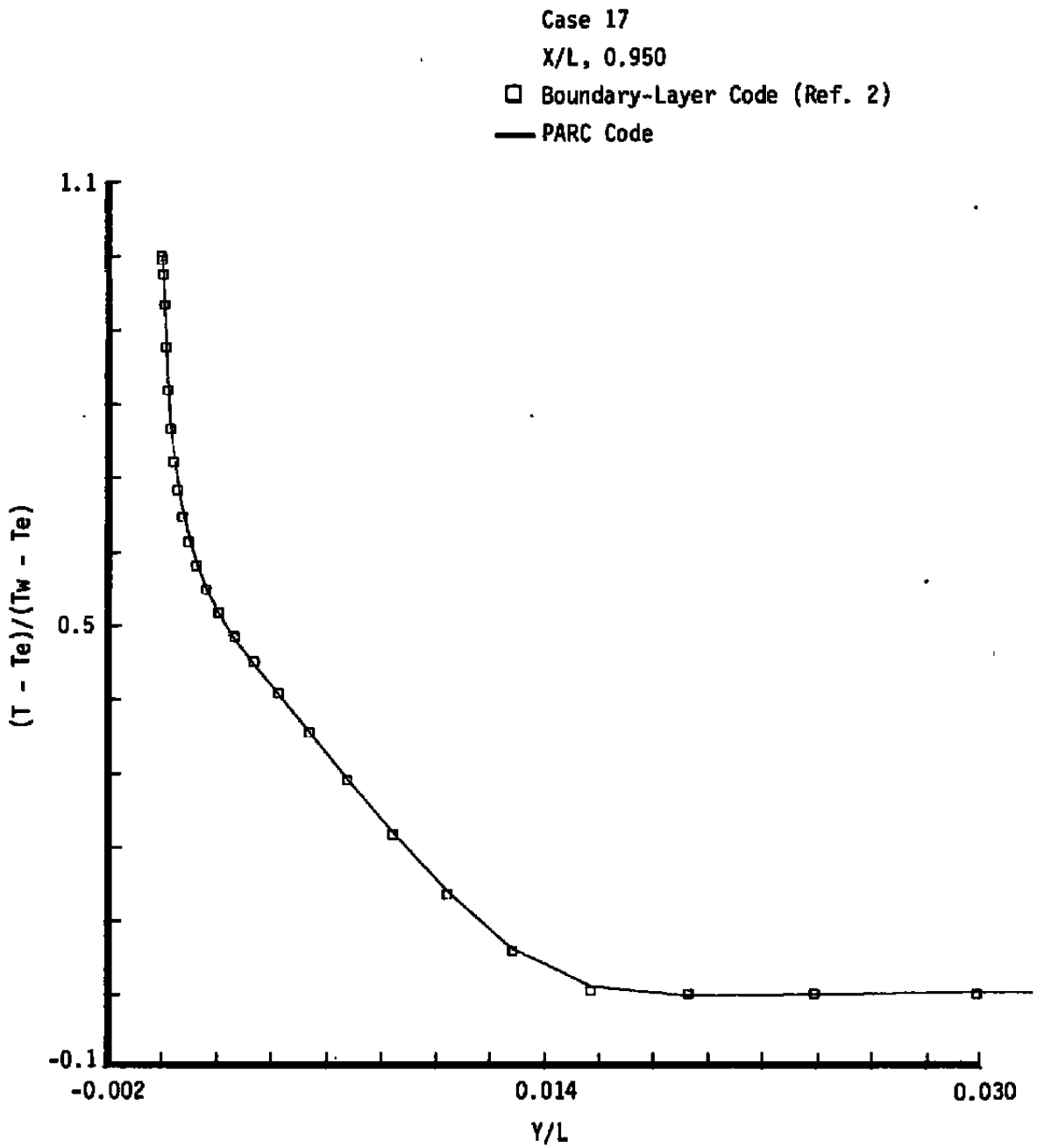

b. Temperature profile (edge scaling)
Figure 13. Continued.

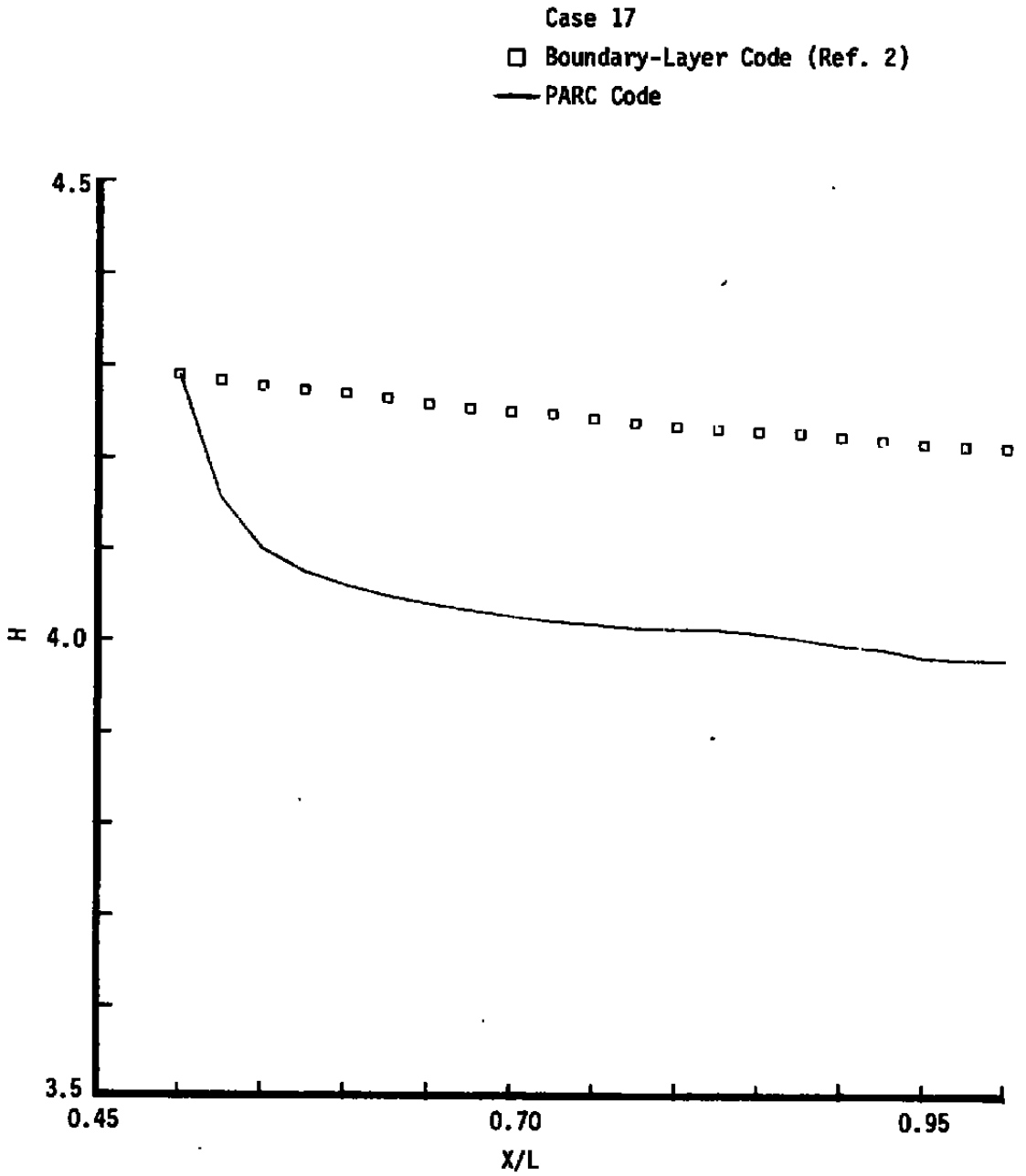

c. Shape factor streamwise variation
Figure 13. Continued.

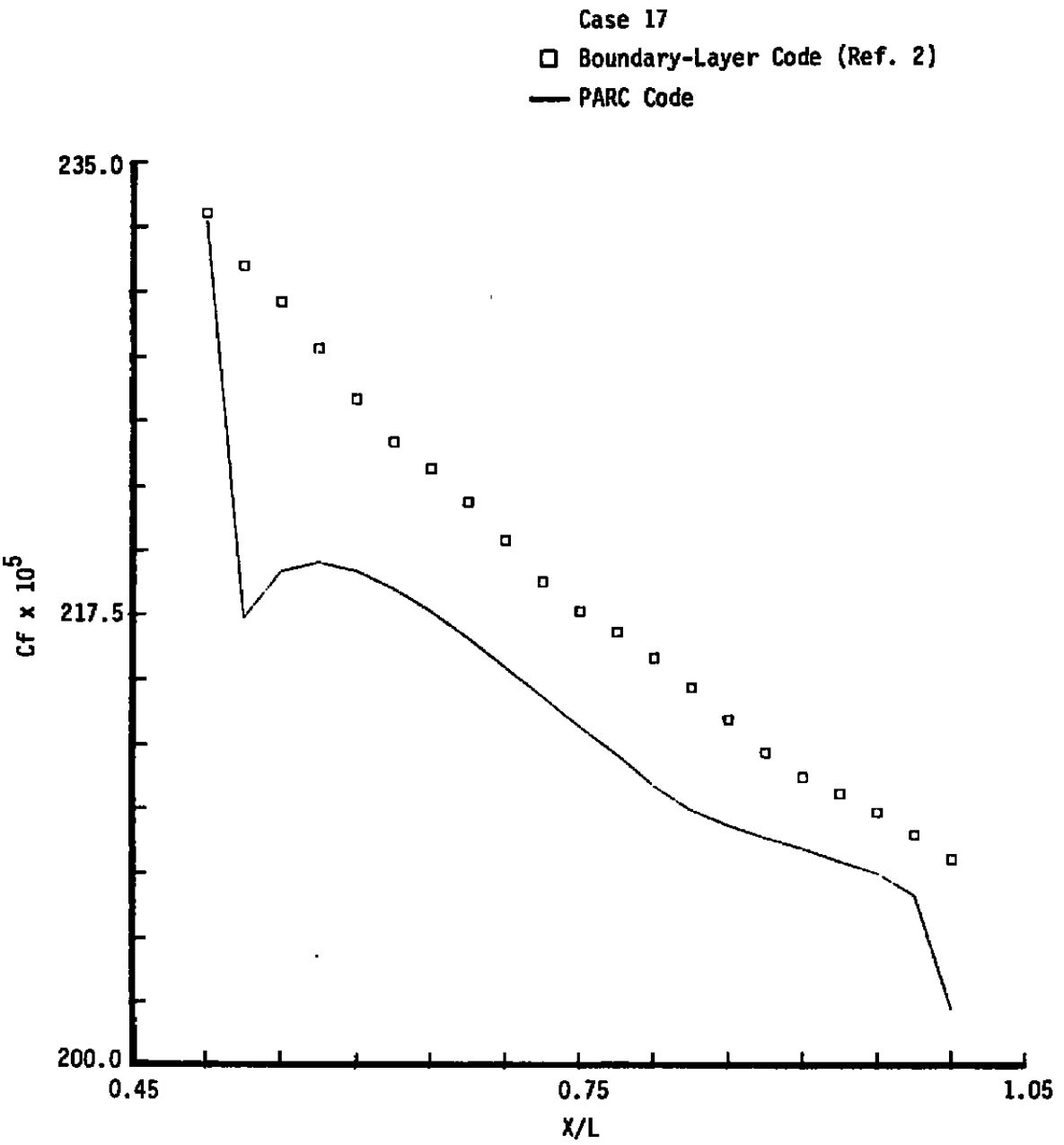

d. Skin friction streamwise variation
Figure 13. Continued.

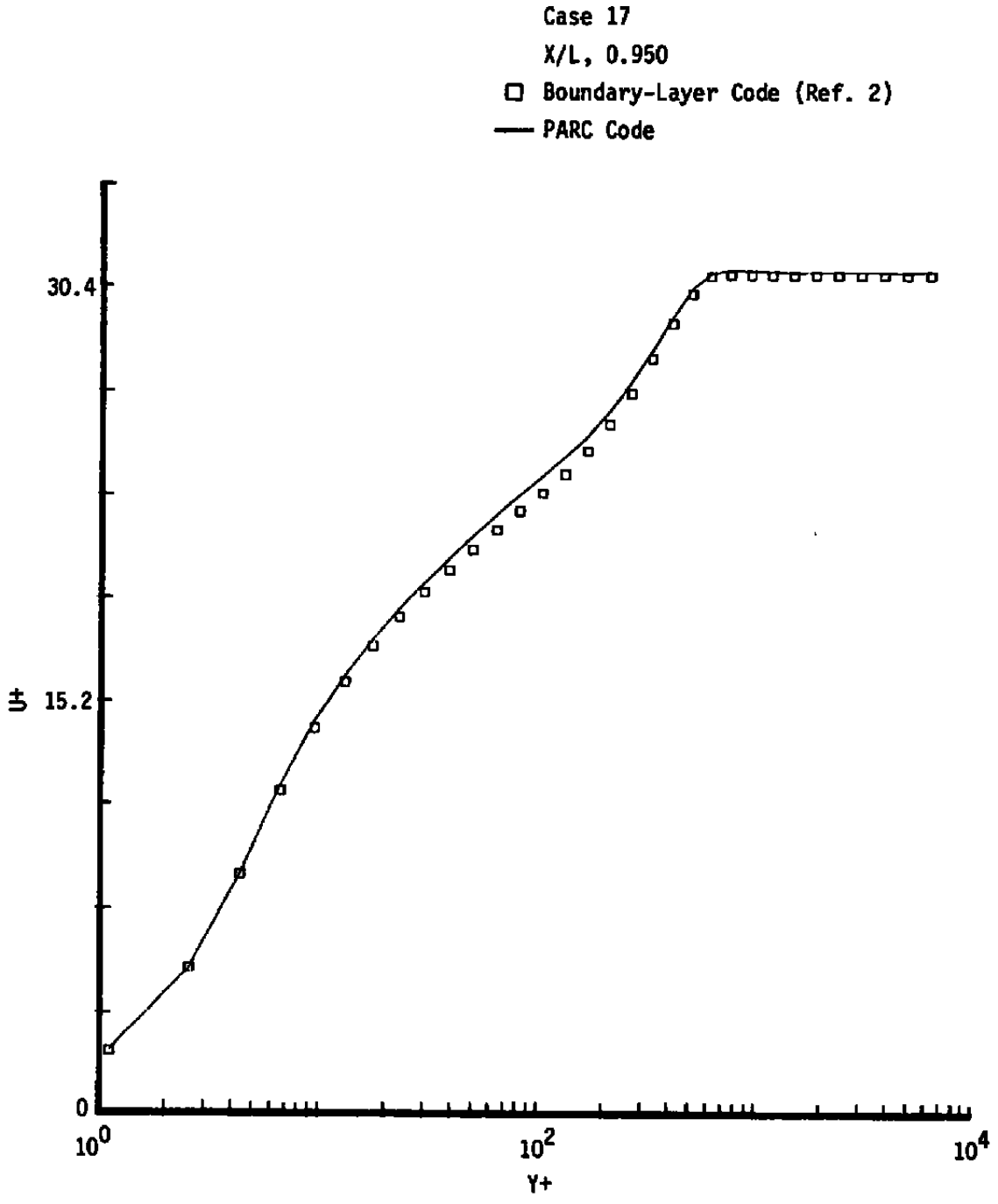

e. Velocity profile (wall scaling)
Figure 13. Continued.

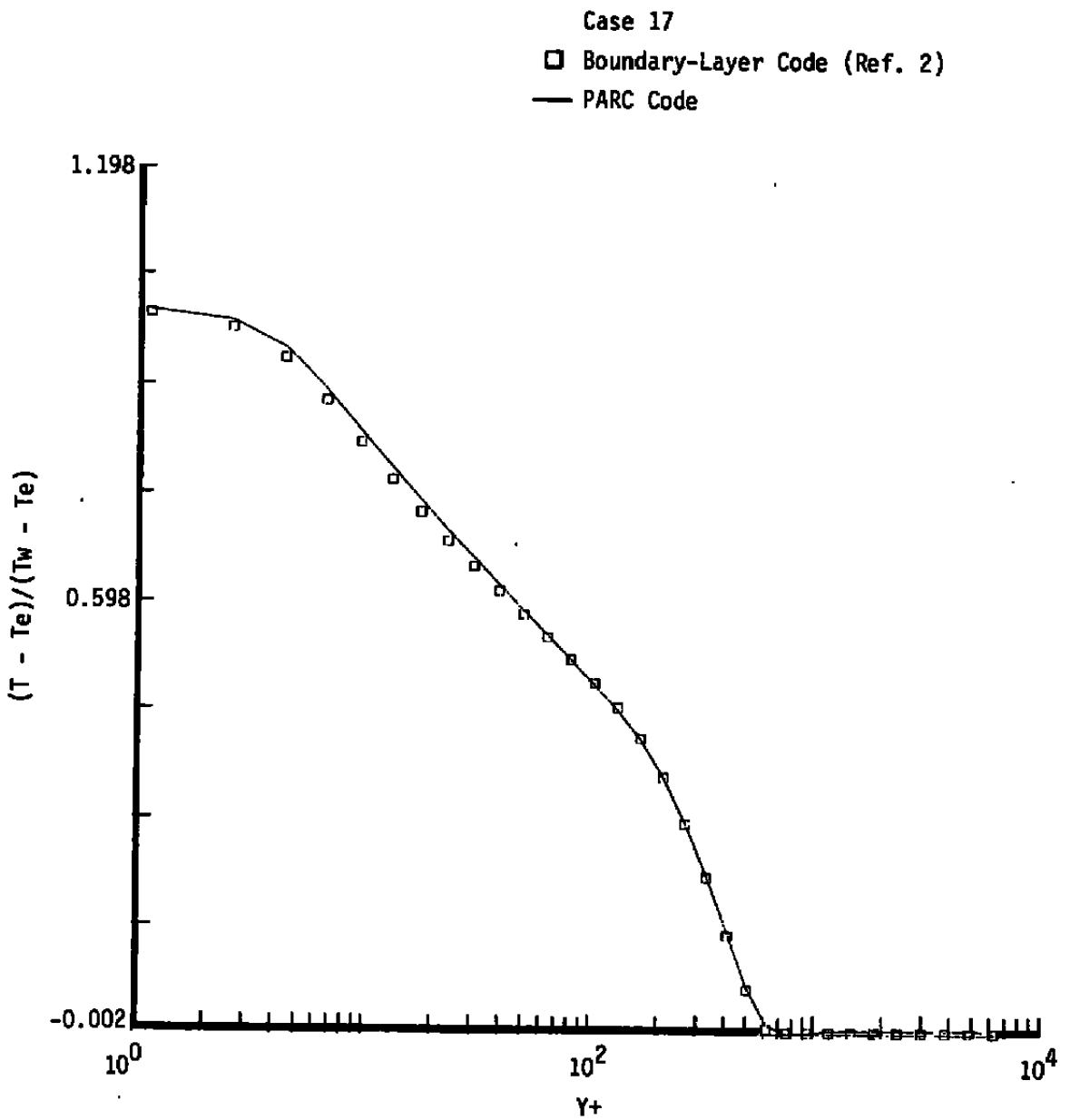

f. Temperature profile (wall scaling)
Figure 13. Concluded.

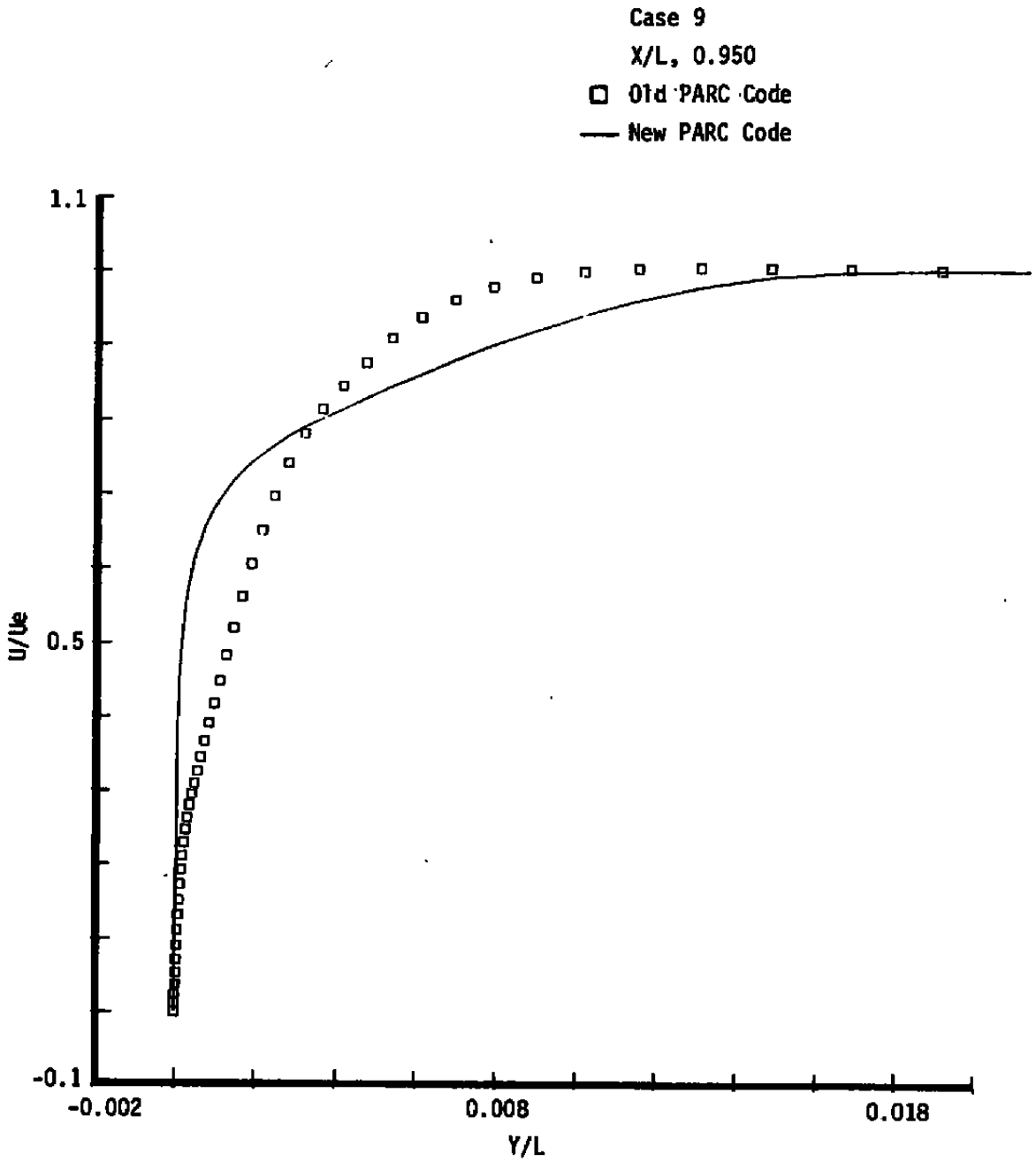

a. Velocity profiles (old versus new; edge scaling)

Figure 14. Turbulence model effects on turbulent flat-plate flow.

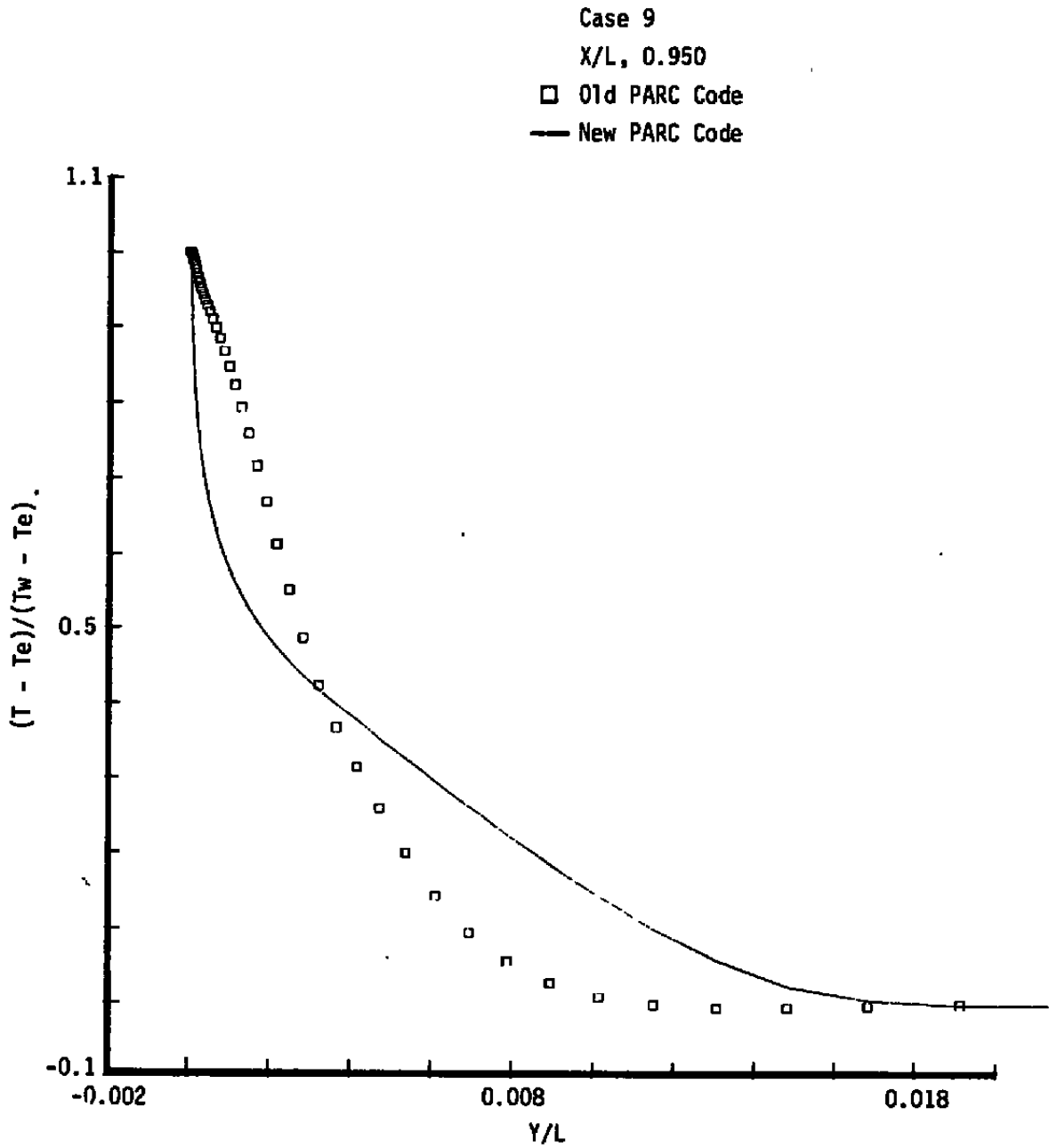

b. Temperature profiles (old versus new; edge scaling)
Figure 14. Continued.

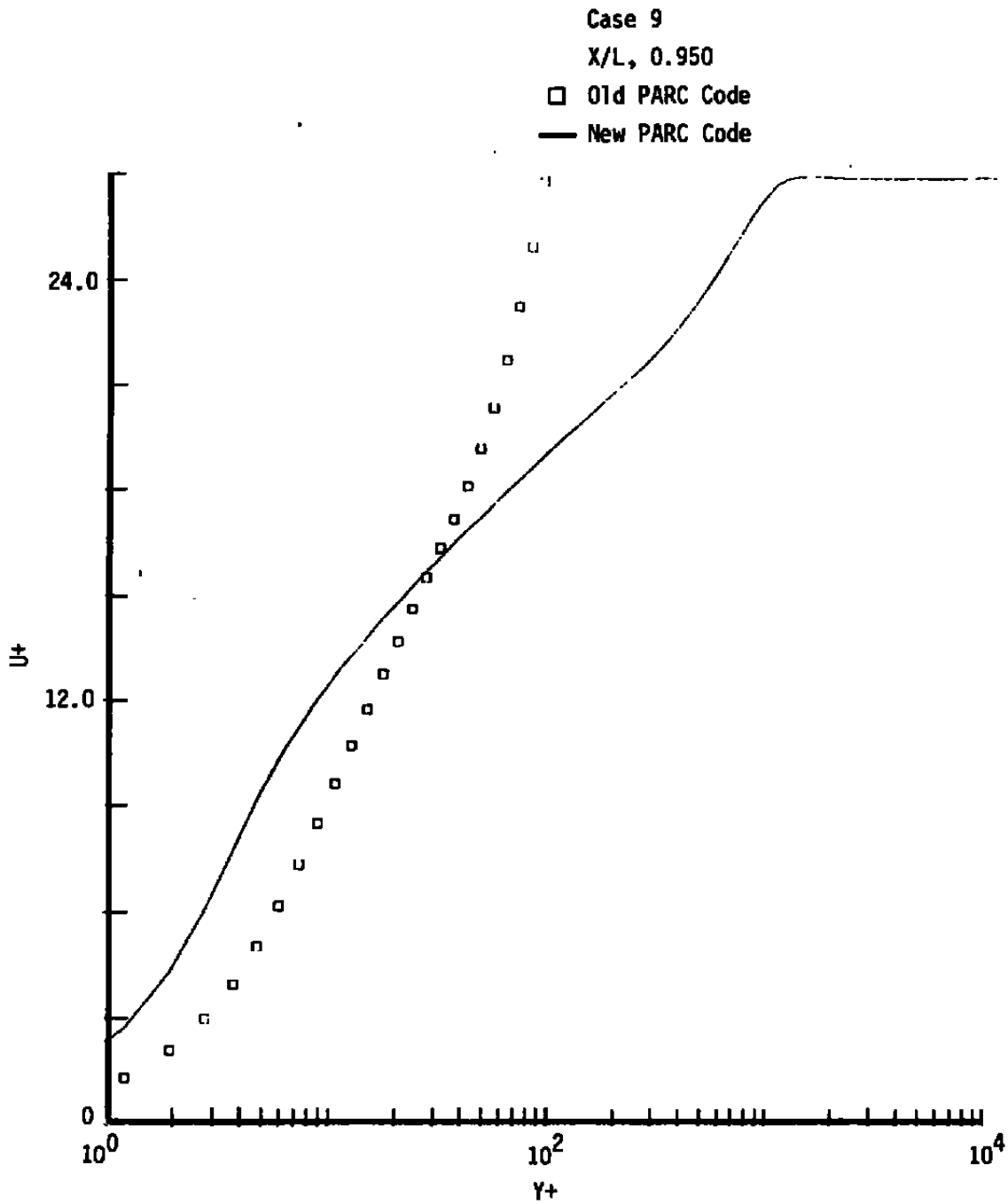

c. Velocity profiles (old versus new; wall scaling)

Figure 14. Continued.

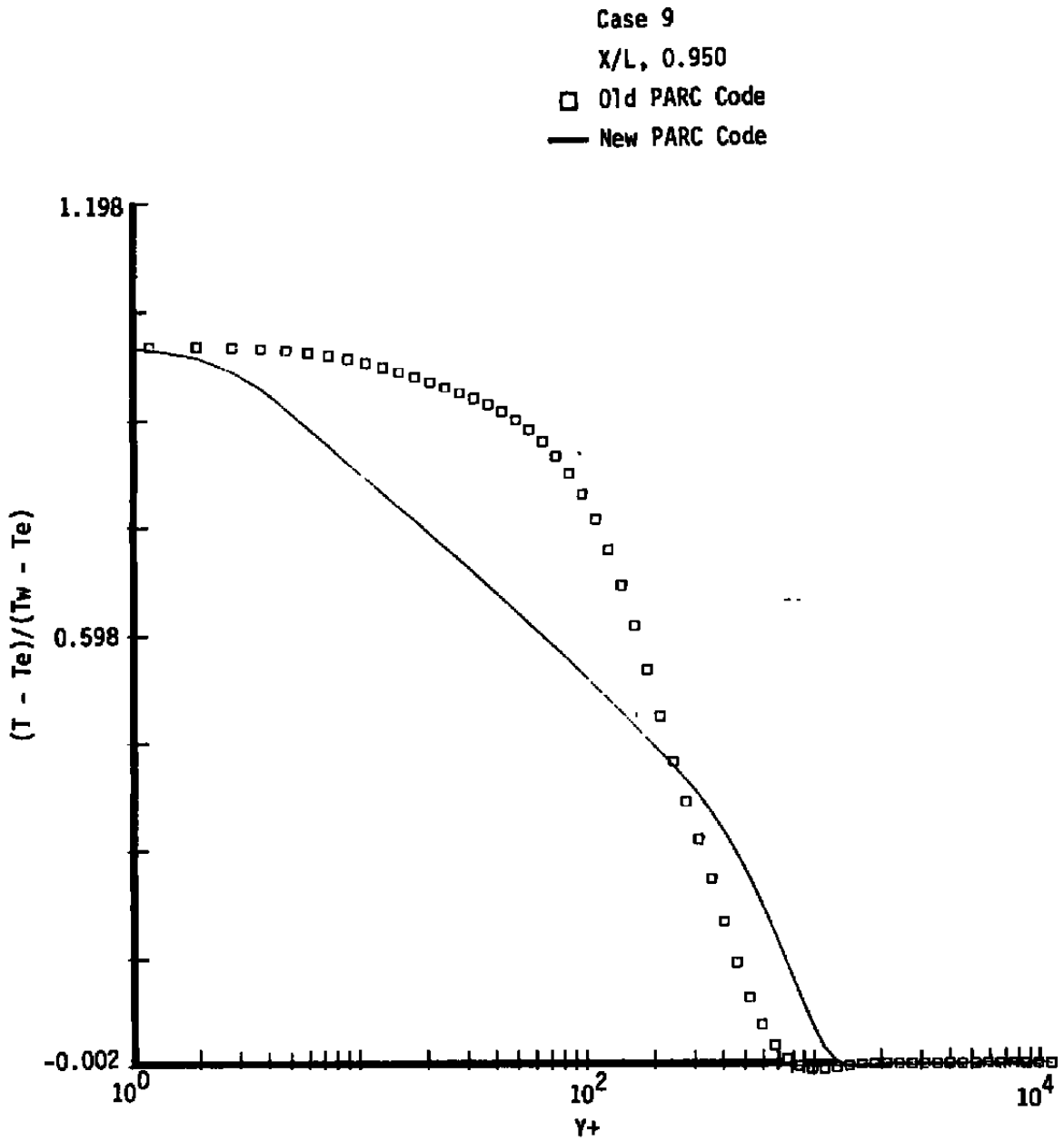

d. Temperature profiles (old versus new; wall scaling)
Figure 14. Concluded.

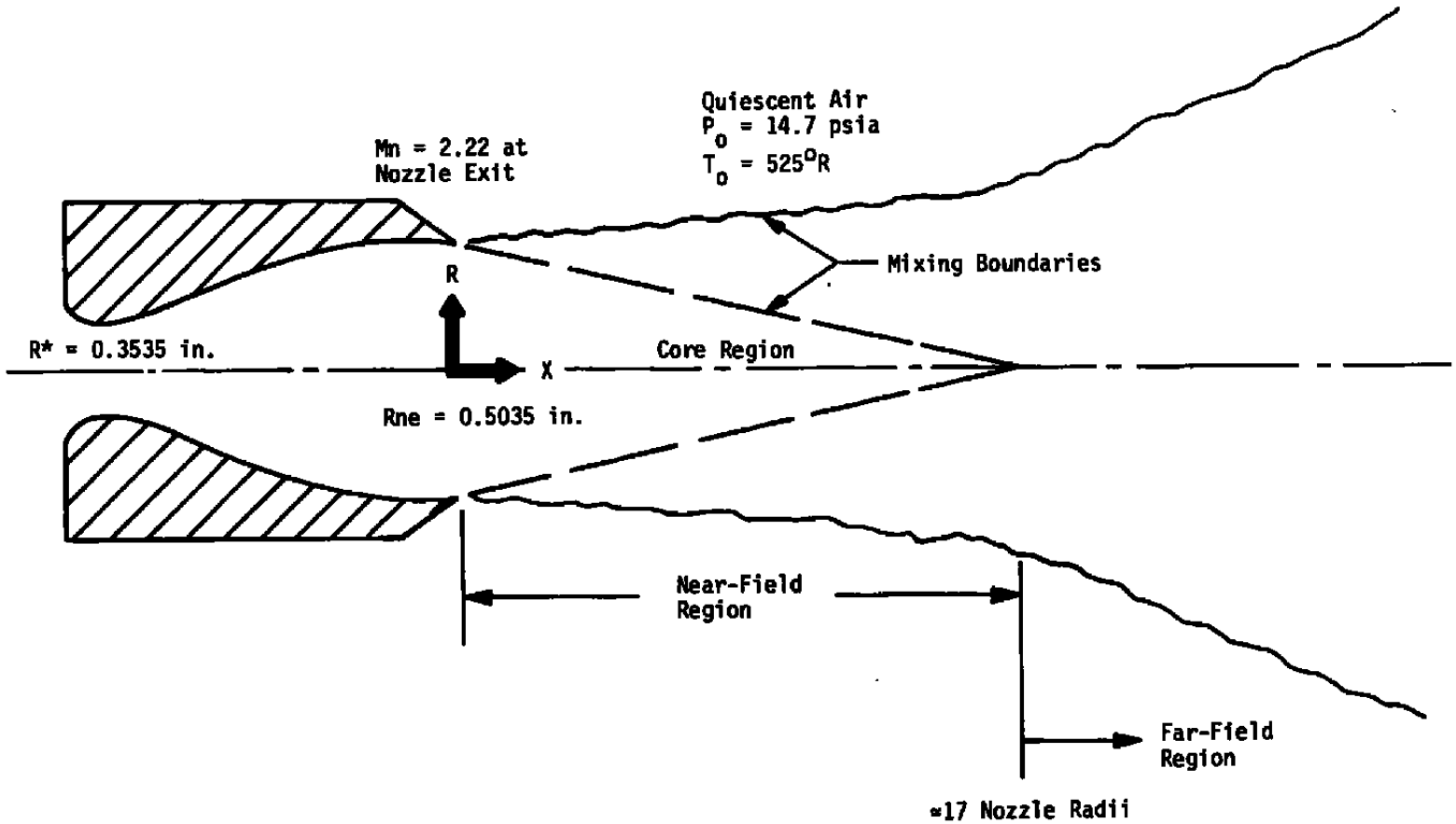

Figure 15. Supersonic free-jet basic formulation.

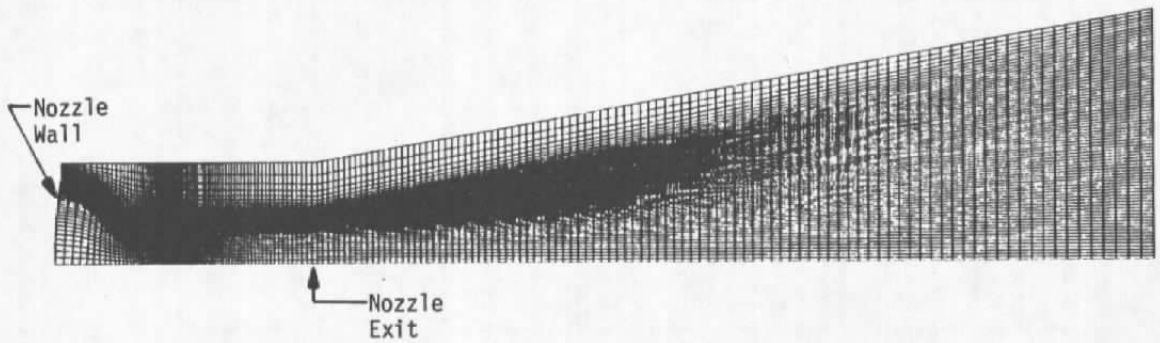

Figure 16. Near-wake grid for supersonic free jet.

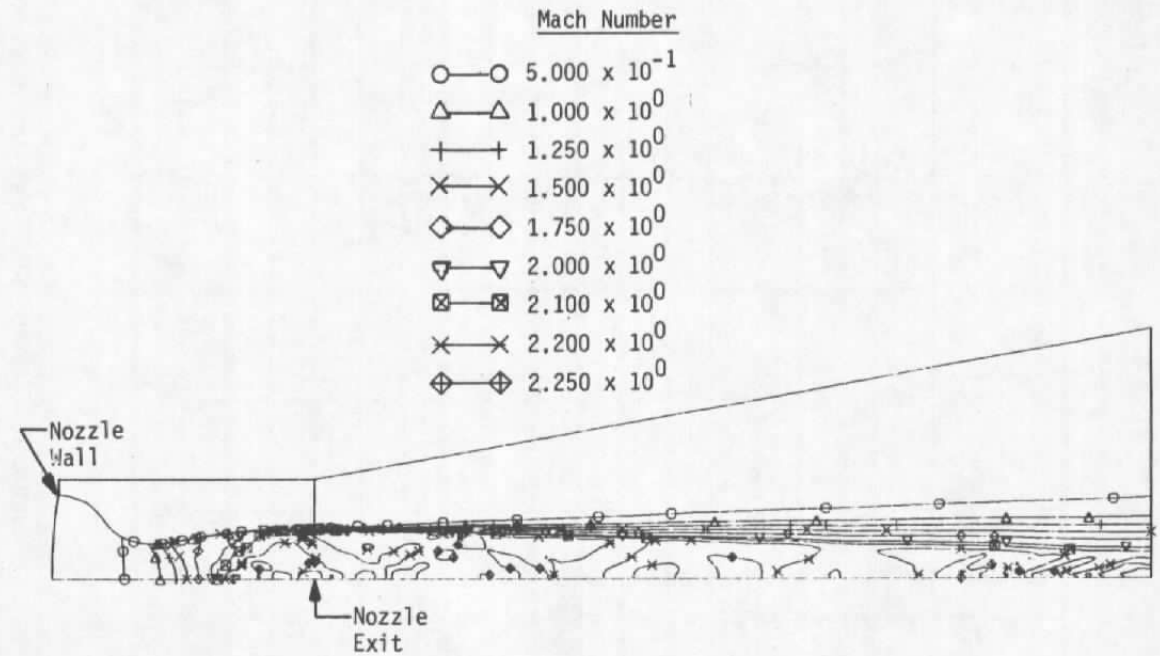

Figure 17. Calculated near-wake flow field for free jet.

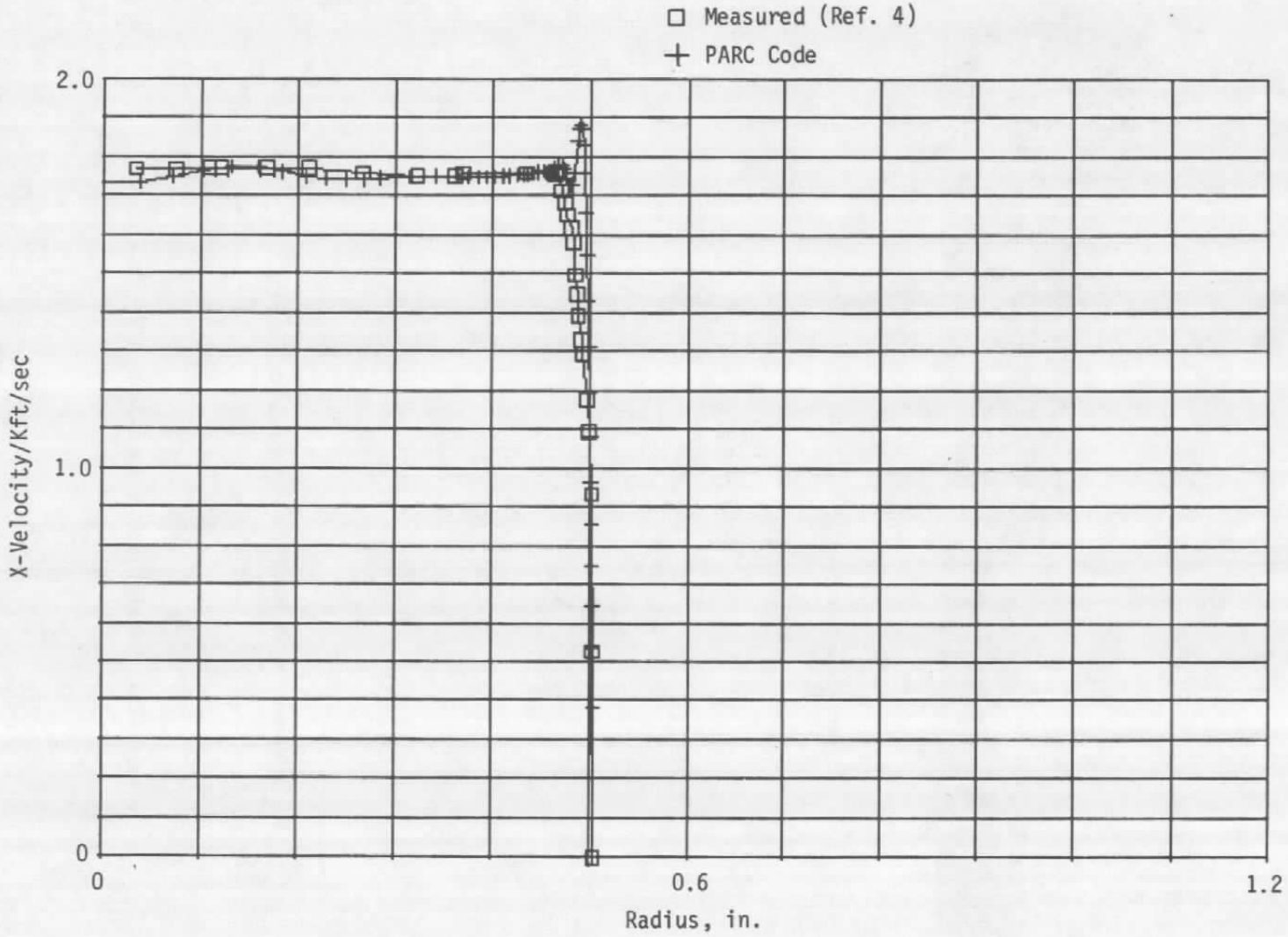

a. Nozzle exit (X/Rne = 0)

Figure 18. Velocity profile comparisons for near wake of free jet.

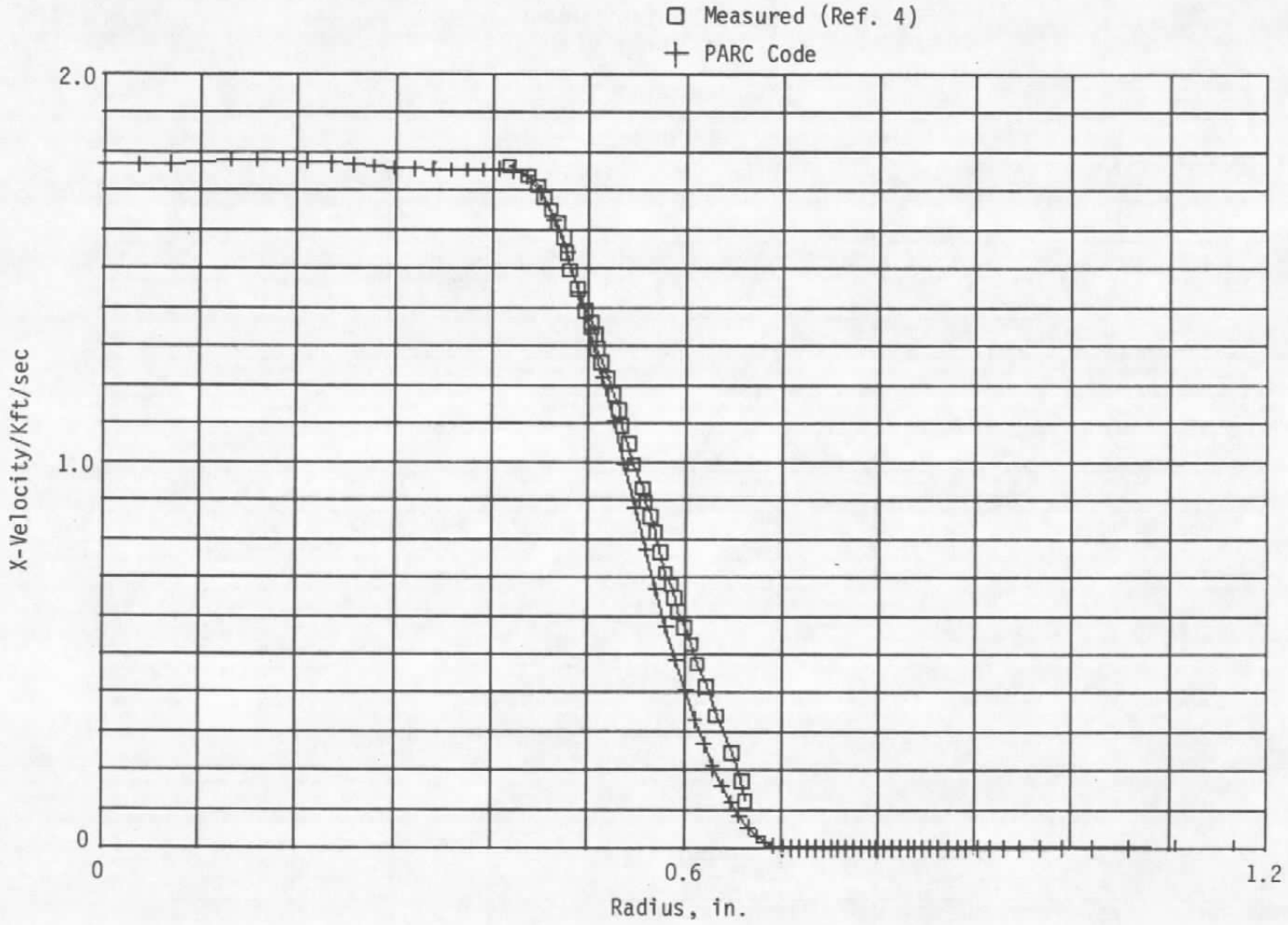

b. X/Rne = 4.0

Figure 18. Continued.

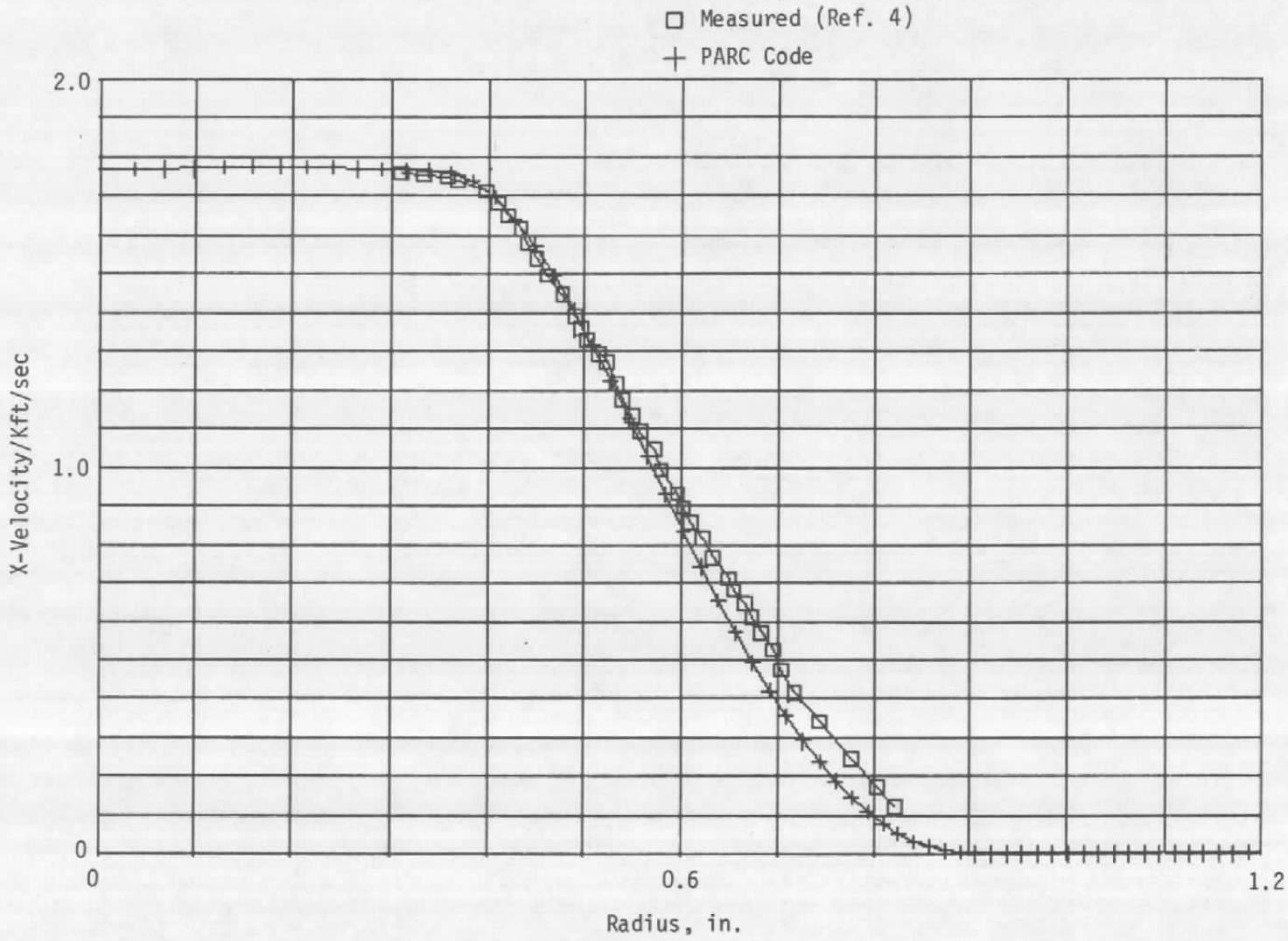

c. X/Rne = 8.0

Figure 18. Continued.

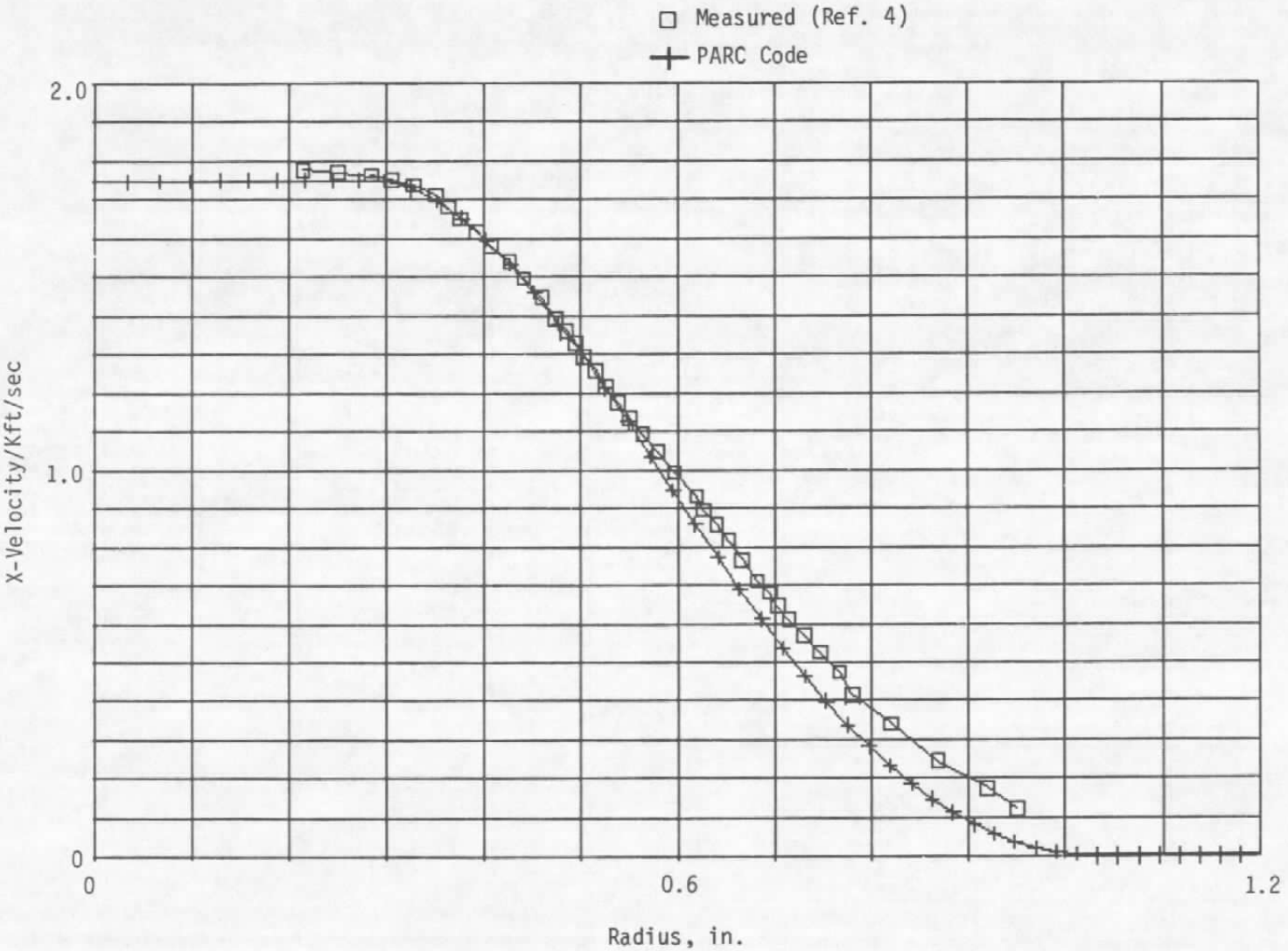

d. X/Rne = 11.0

Figure 18. Continued.

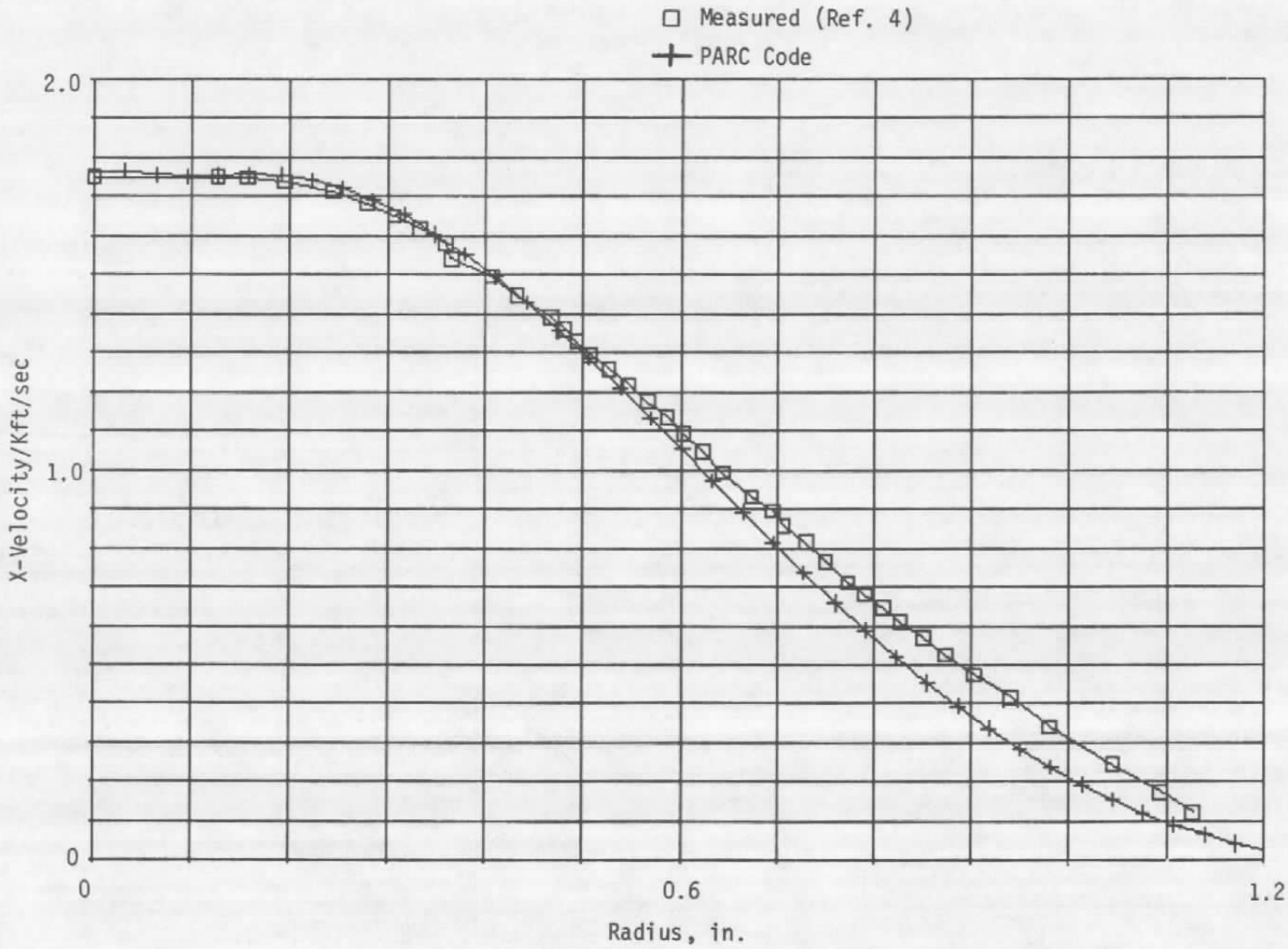

e. X/Rne = 17.0

Figure 18. Concluded.

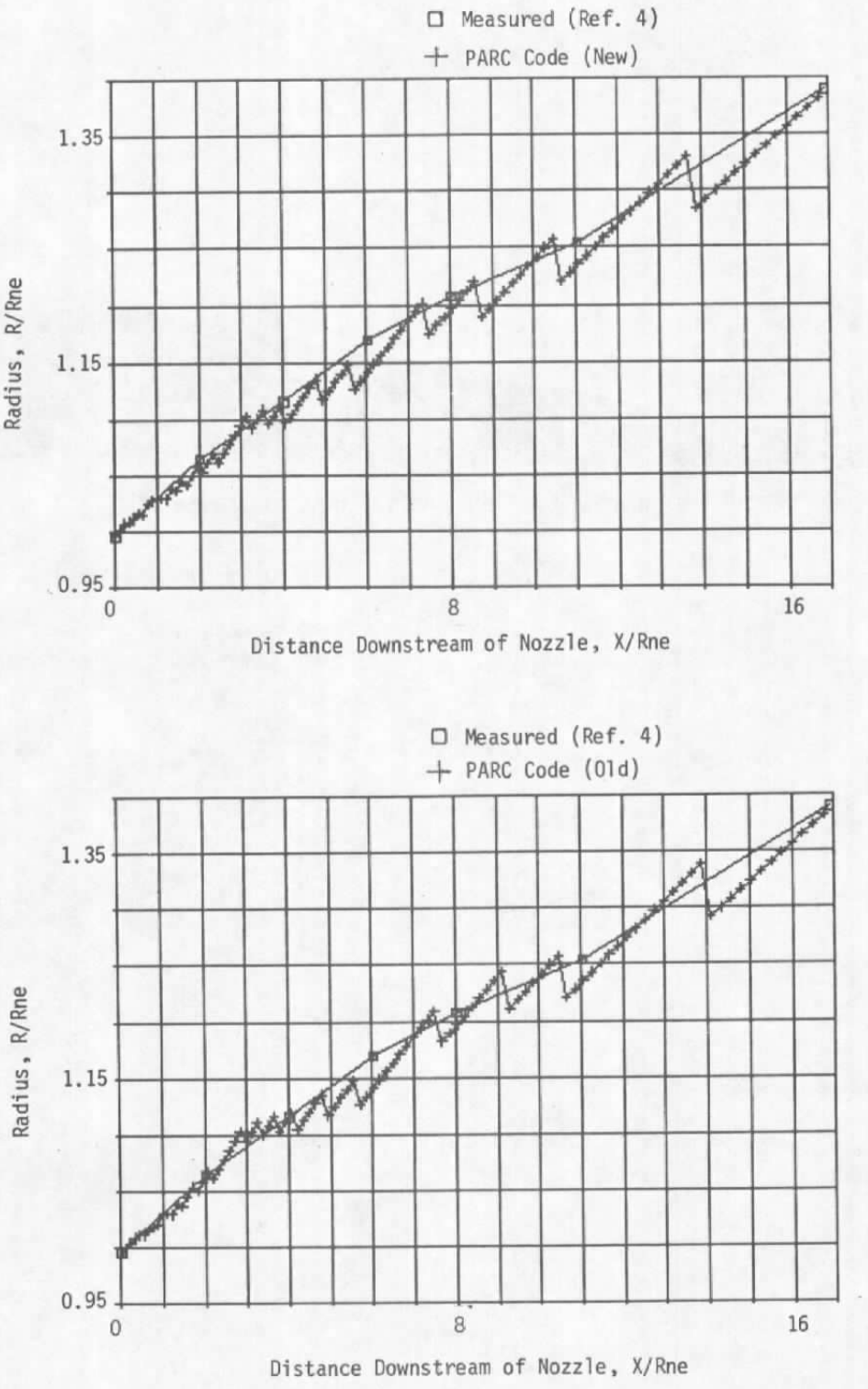

Figure 19. Spreading rate comparisons for near wake of free jet.

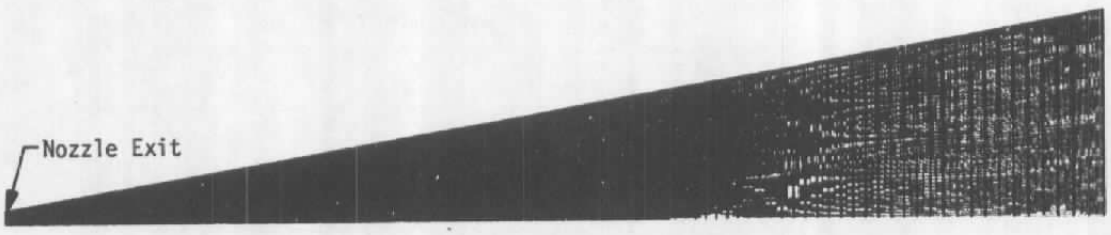

Figure 20. Far-field grid for supersonic free jet.

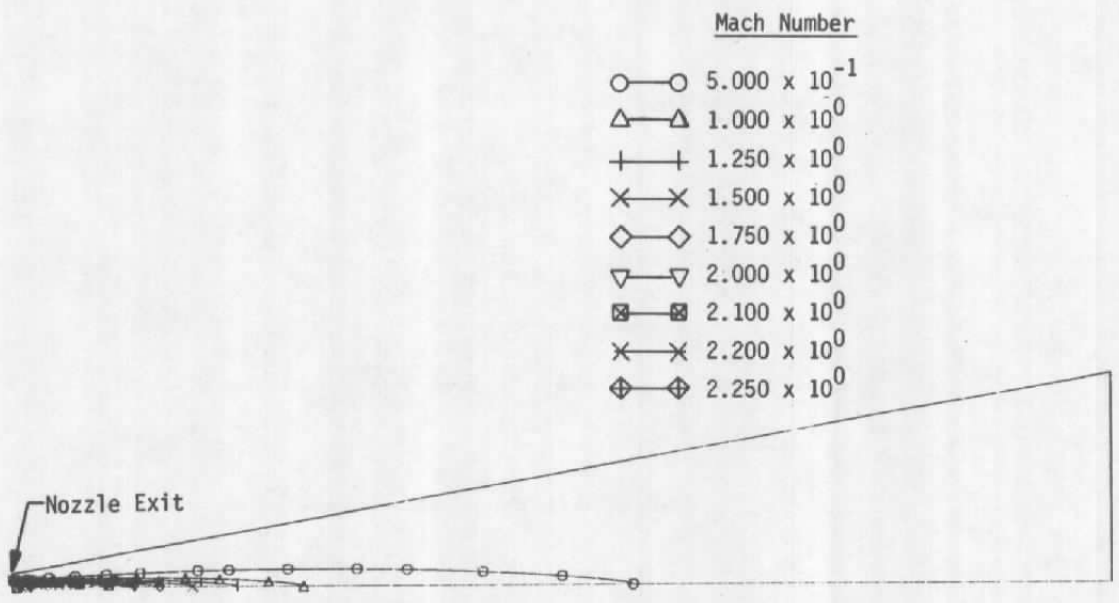

Figure 21. Calculated far-wake flow field for free jet.

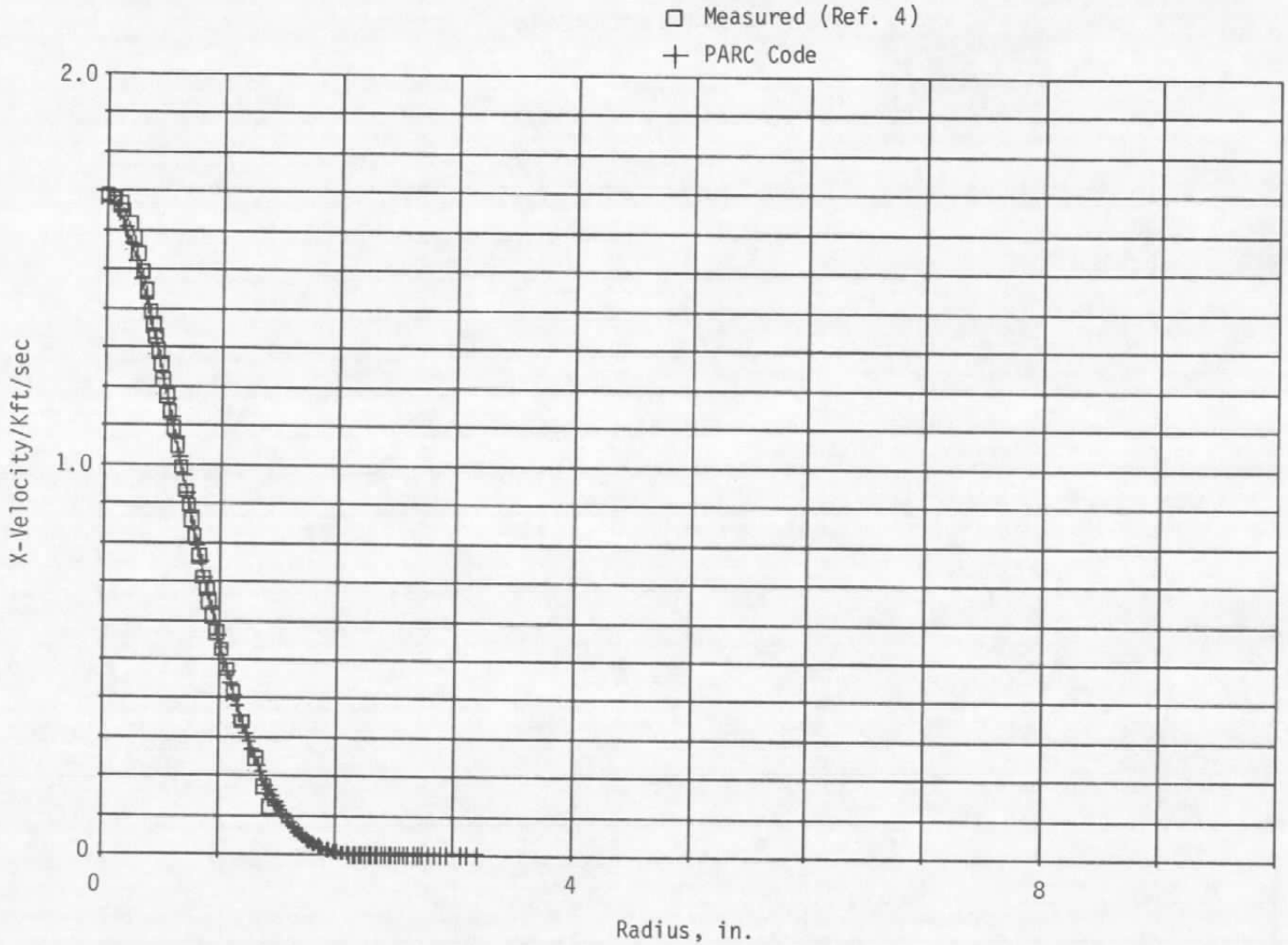

a. X/Rne = 25.0 (X/Rne = 0 at nozzle exit)

Figure 22. Velocity profile comparisons for far wake of free jet.

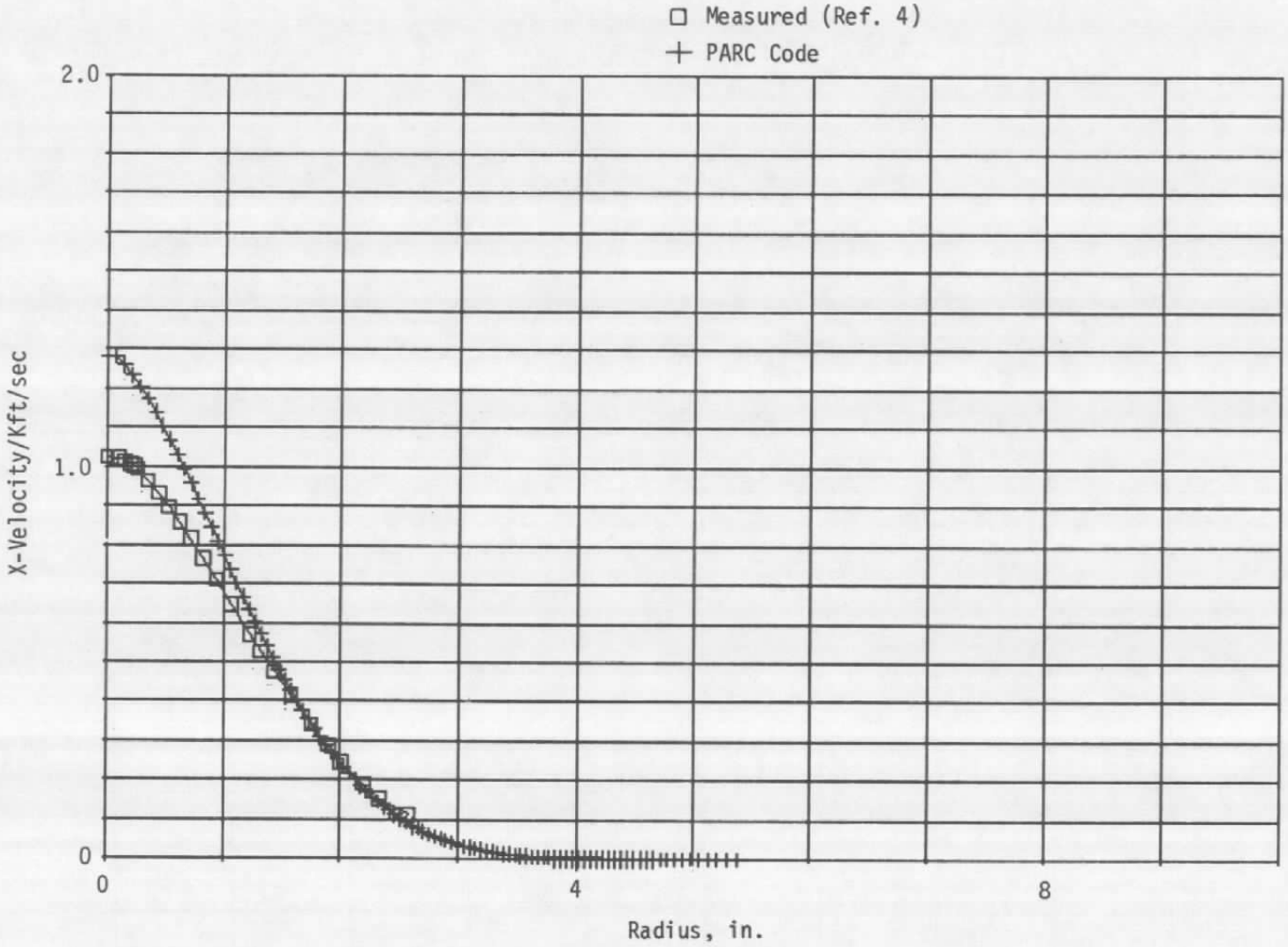

b. X/Rne = 50.0

Figure 22. Continued.

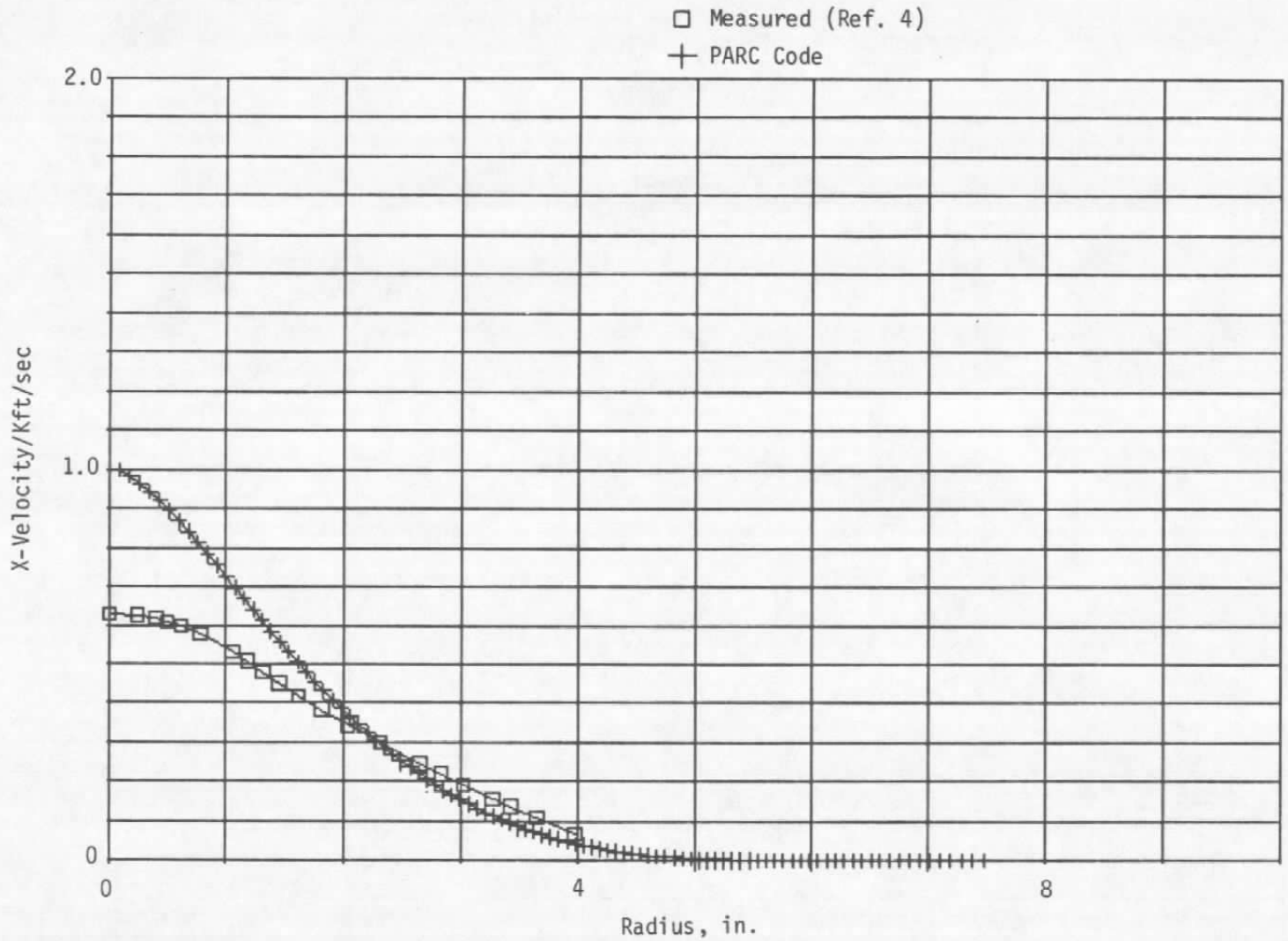

c. X/Rne = 74.0

Figure 22. Continued.

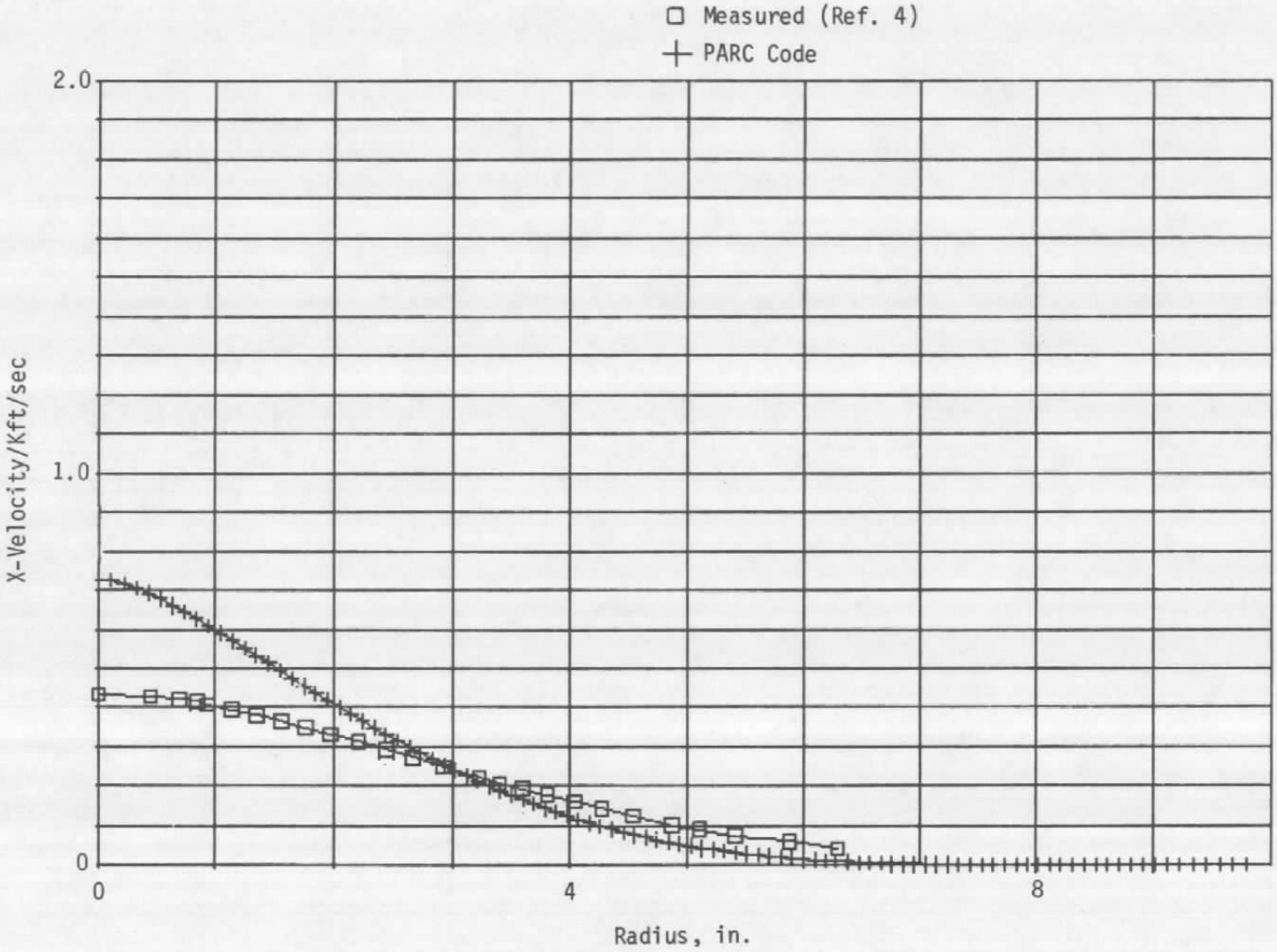

d. X/Rne = 99.0

Figure 22. Continued.

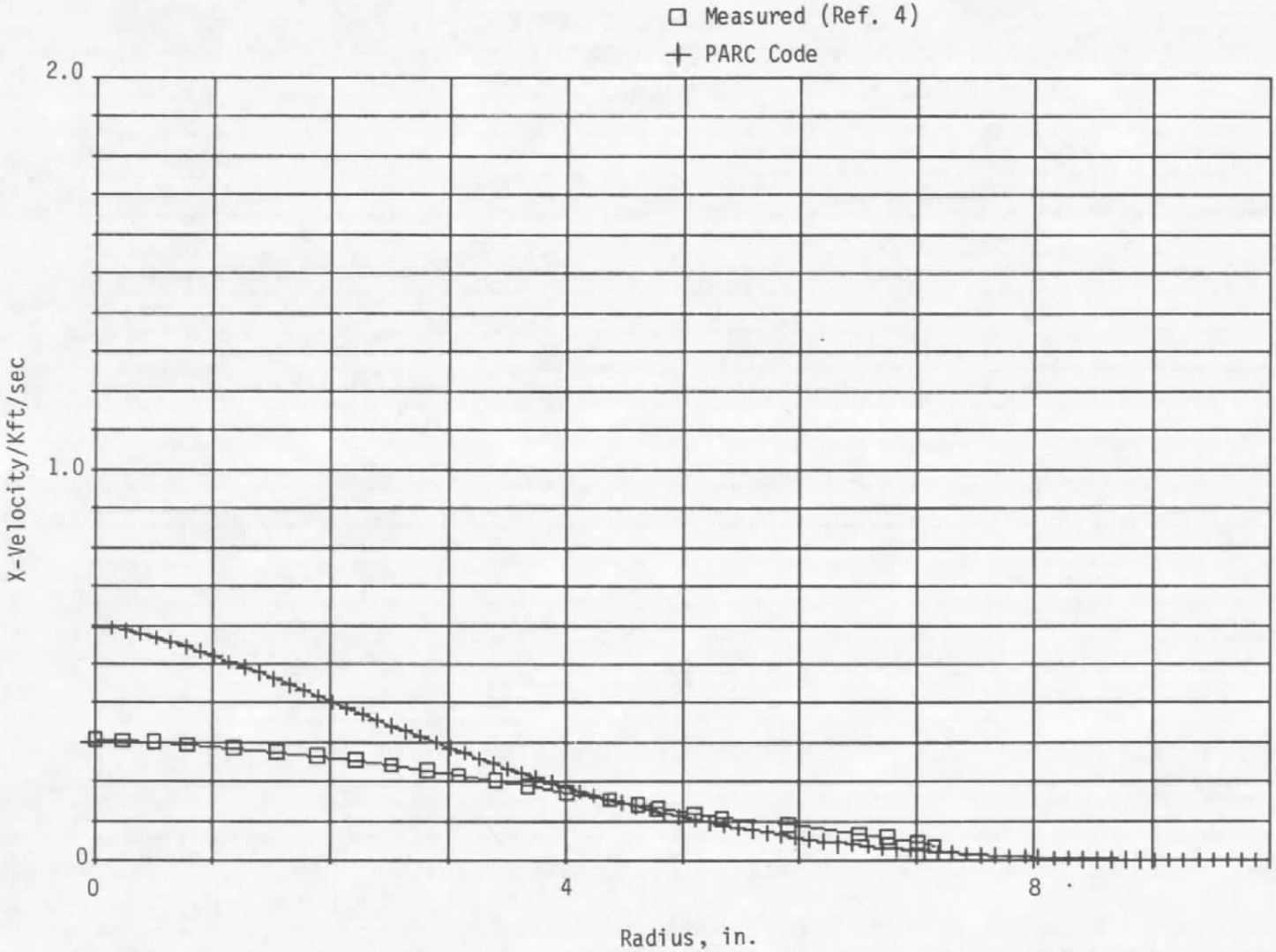

e. X/Rne = 127.0

Figure 22. Continued.

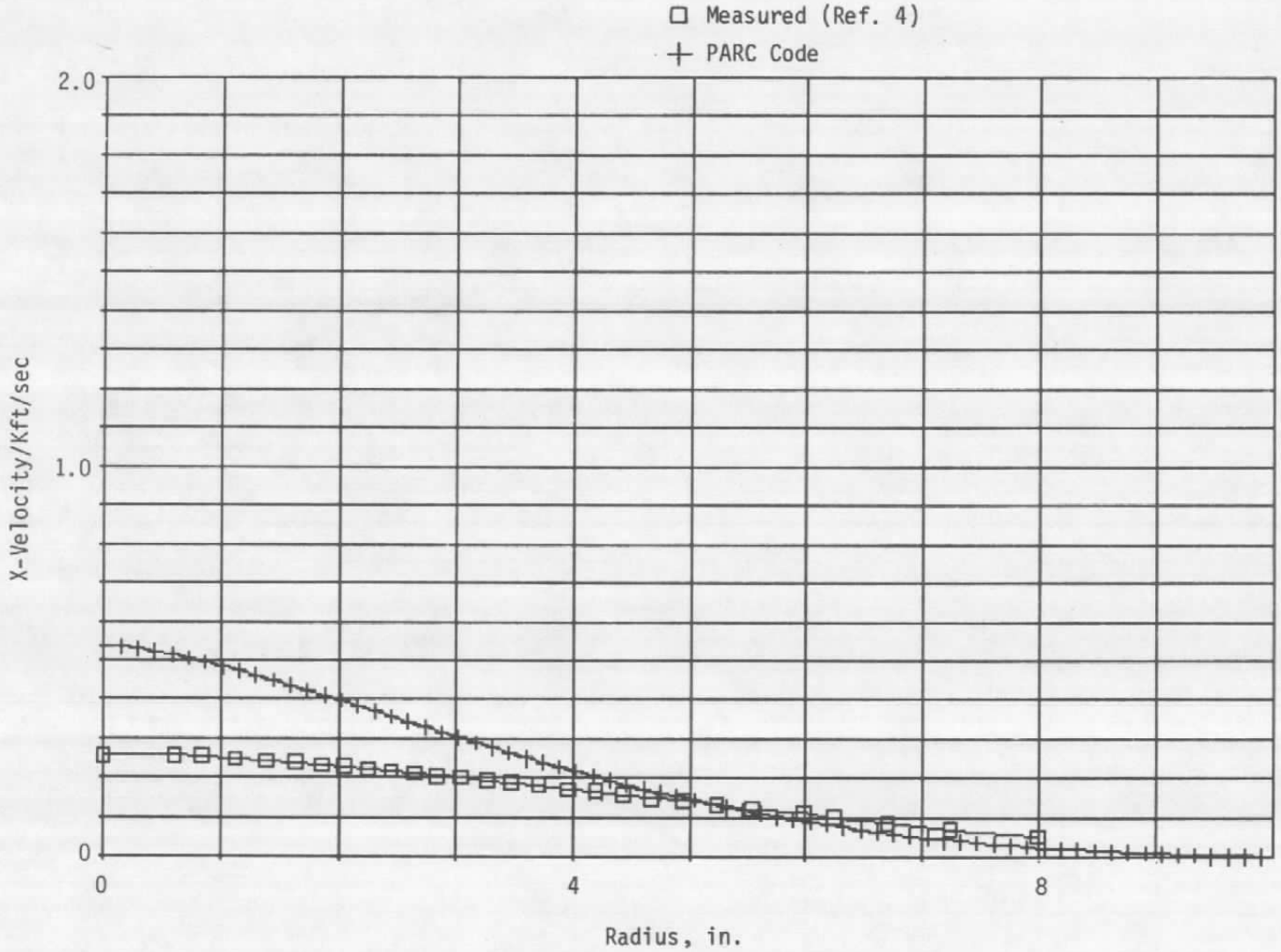

f. X/Rne = 150.0

Figure 22. Concluded.

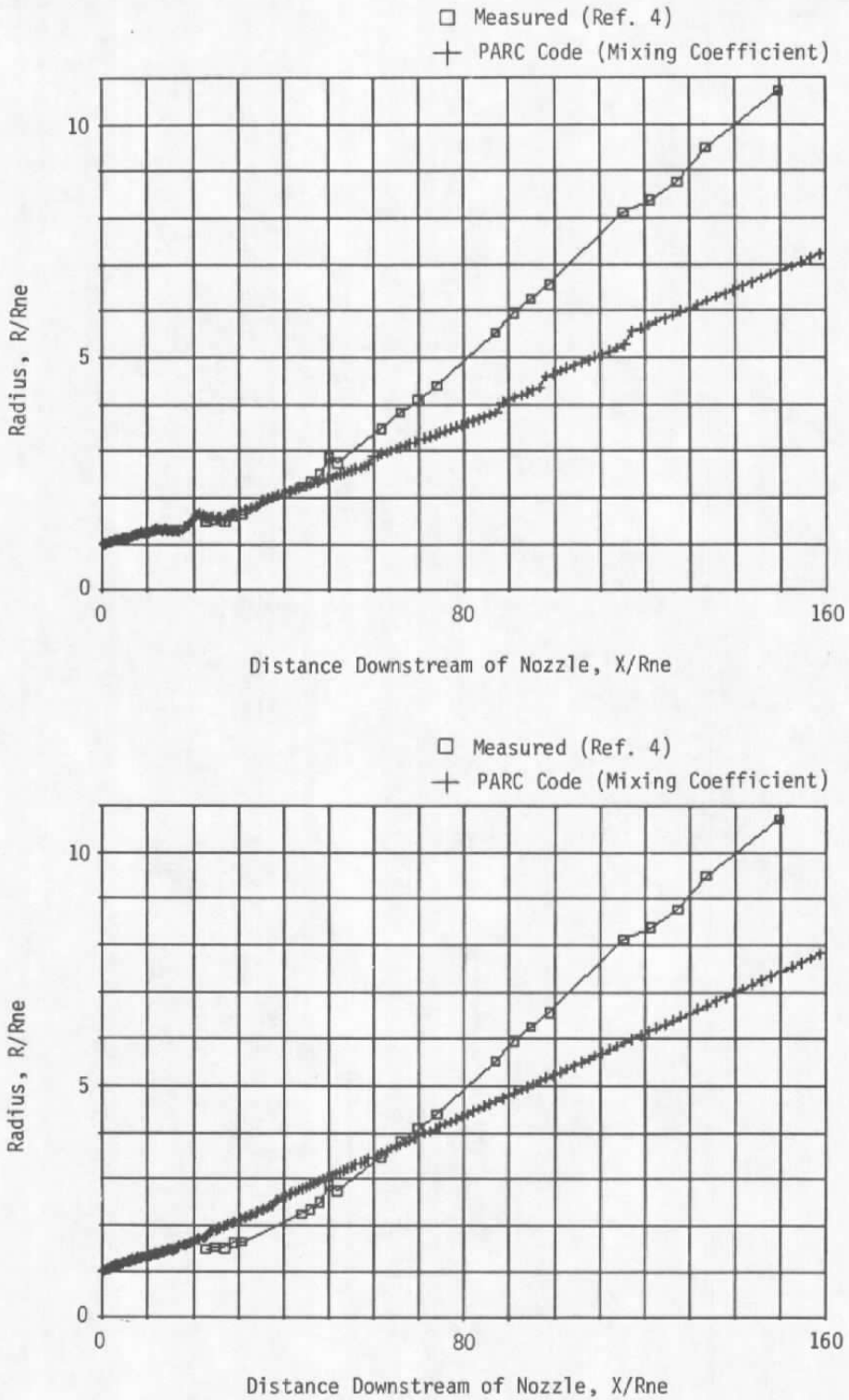

Figure 23. Spreading rate comparisons for far wake of free jet.

H = 3.79 cm M = 0.03195
ReH = 28,000 P_r = 15.033 psi
$\dot{q}''_w$ = 130 w/m T_r = 531°R

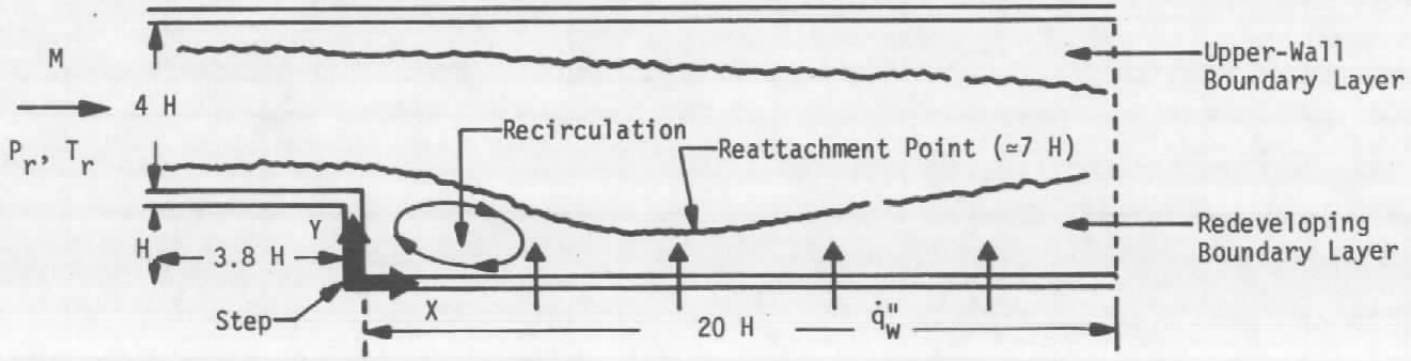

Figure 24. Backstep test case basic formulation.

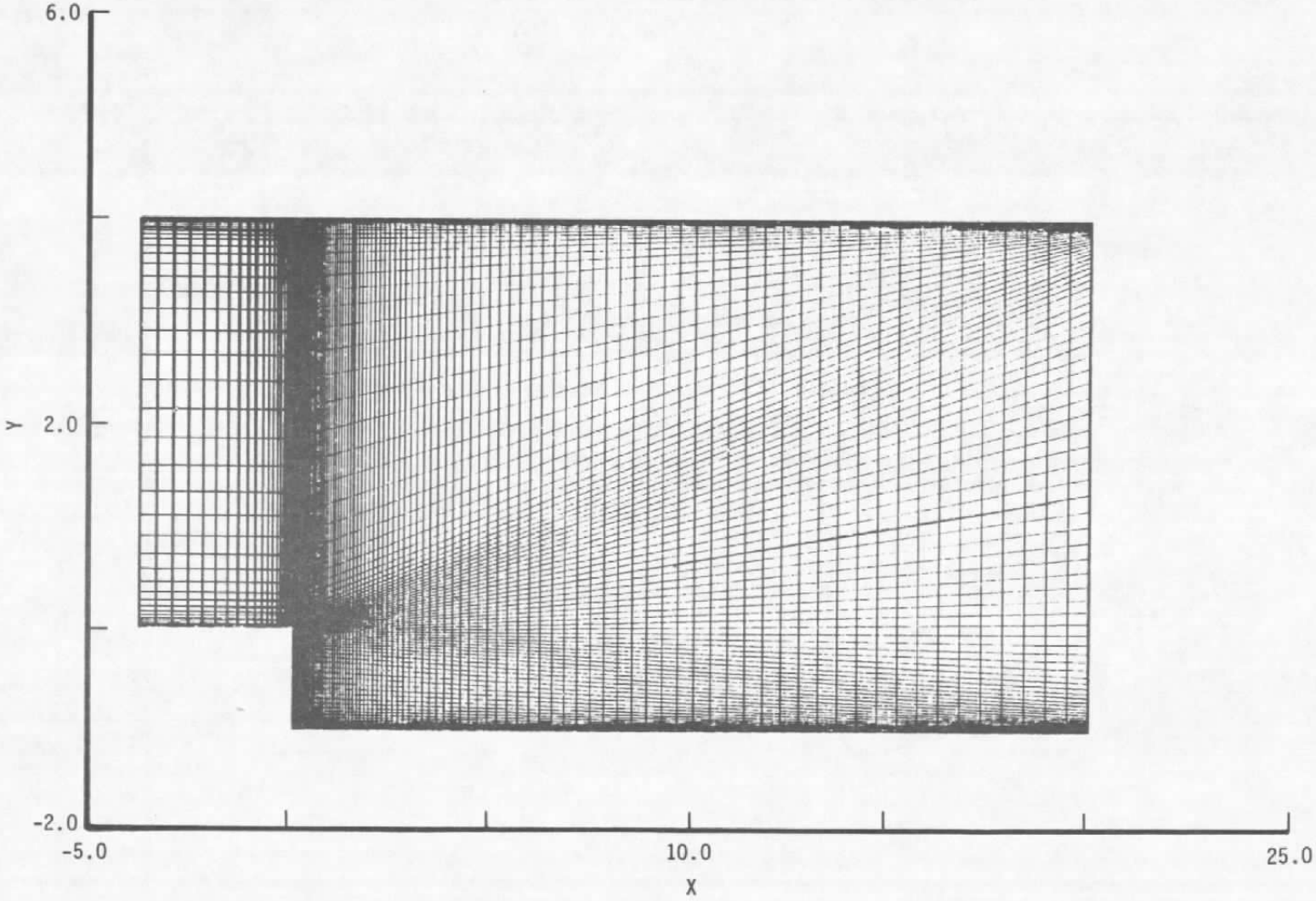

Figure 25. Grid for backstep flow simulation.

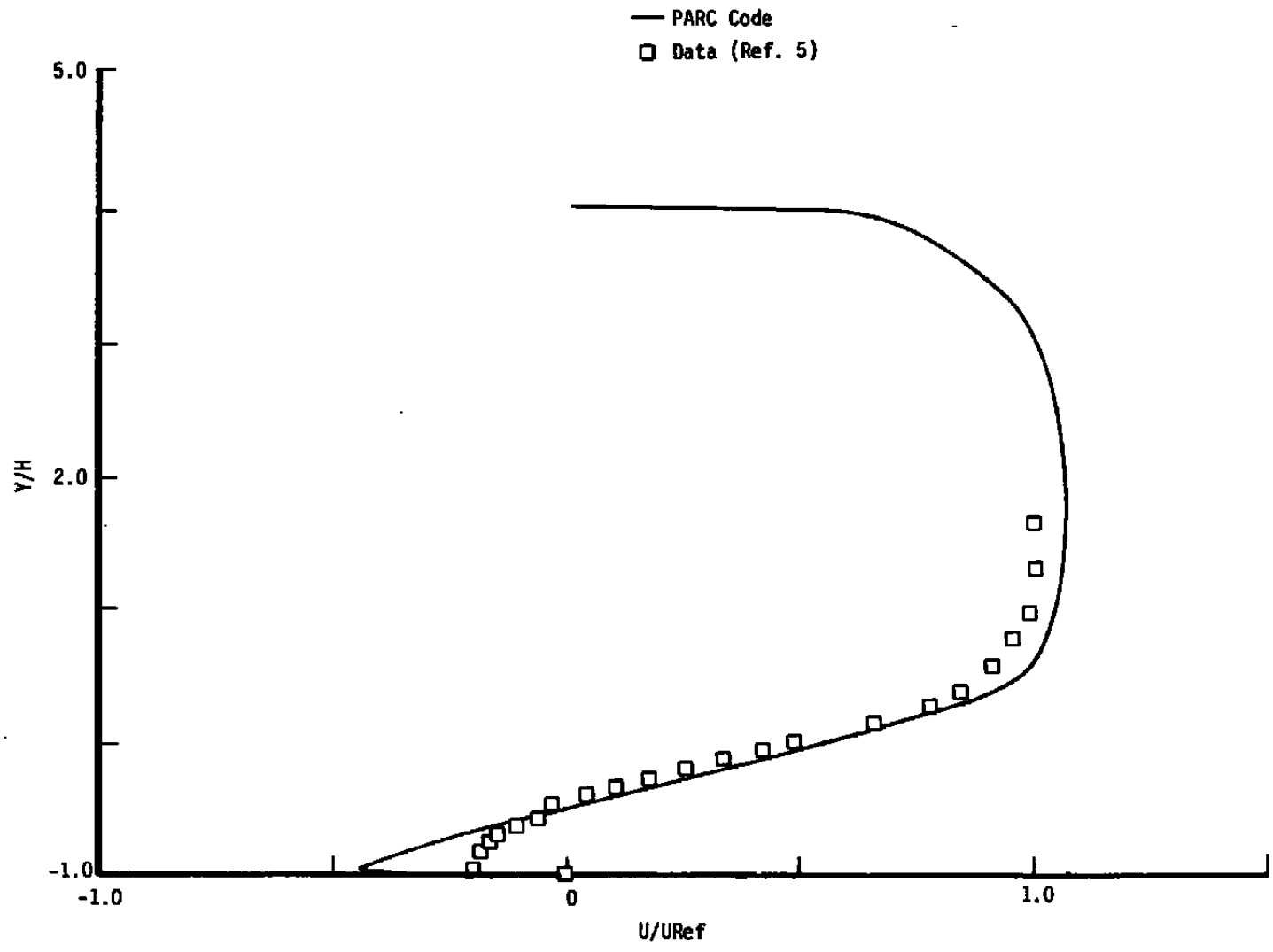

a. X/H = 3.2 (X/H = 0 at step)

Figure 26. Velocity profile comparisons for backstep flow.

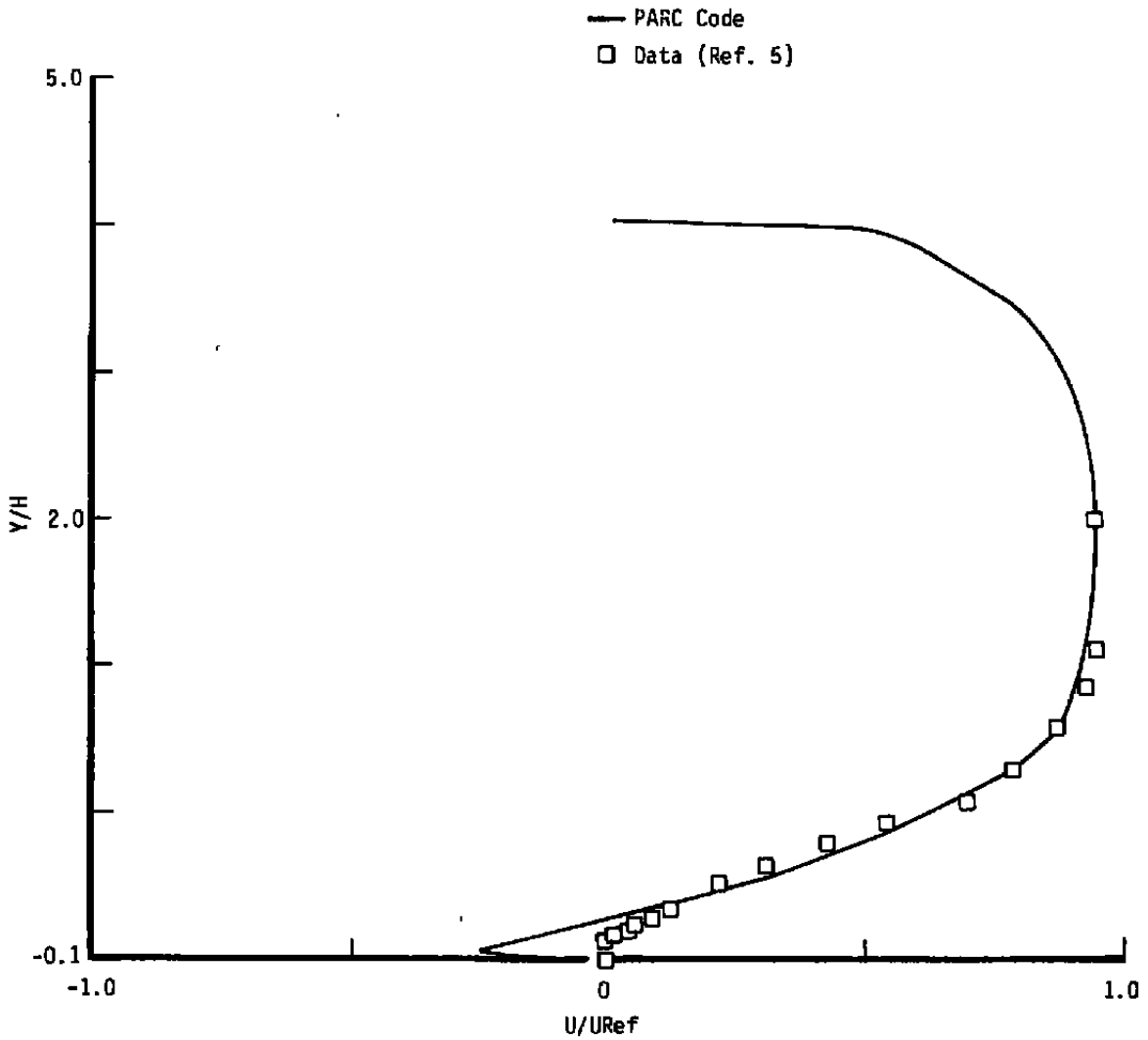

b. X/H = 5.87

Figure 26. Continued.

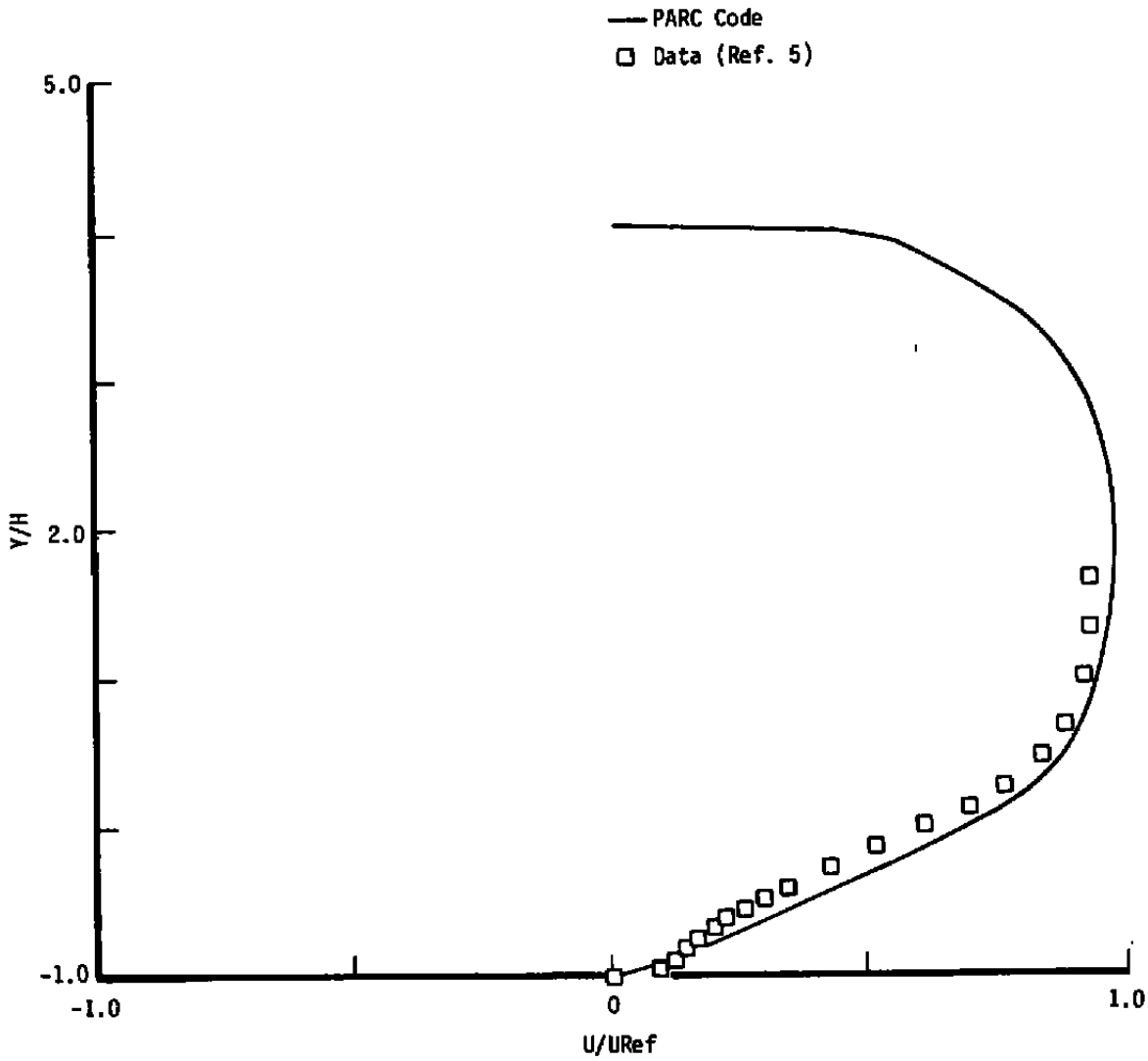

c. X/H = 7.2

Figure 26. Continued.

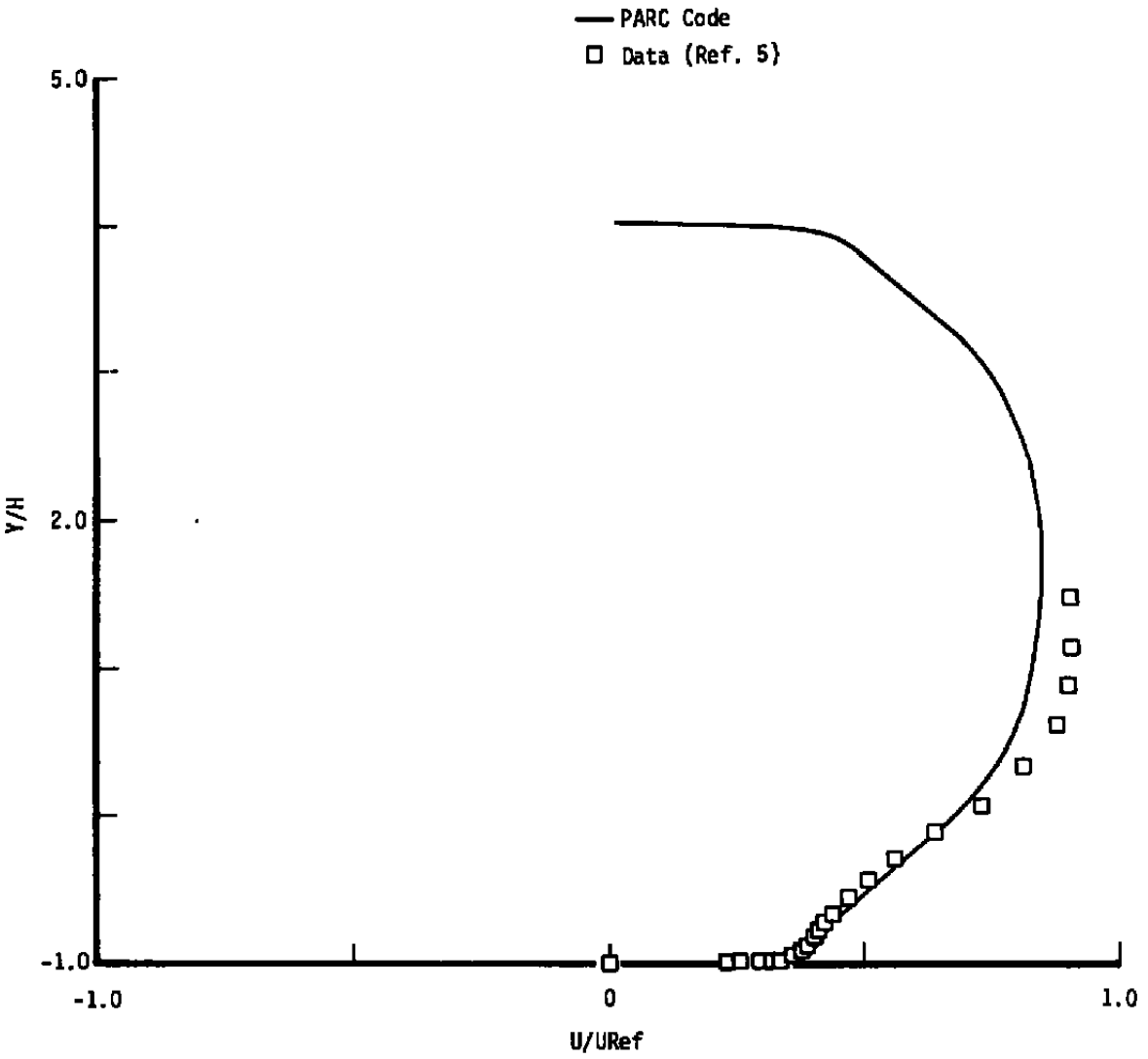

d. X/H = 12.2
Figure 26. Continued.

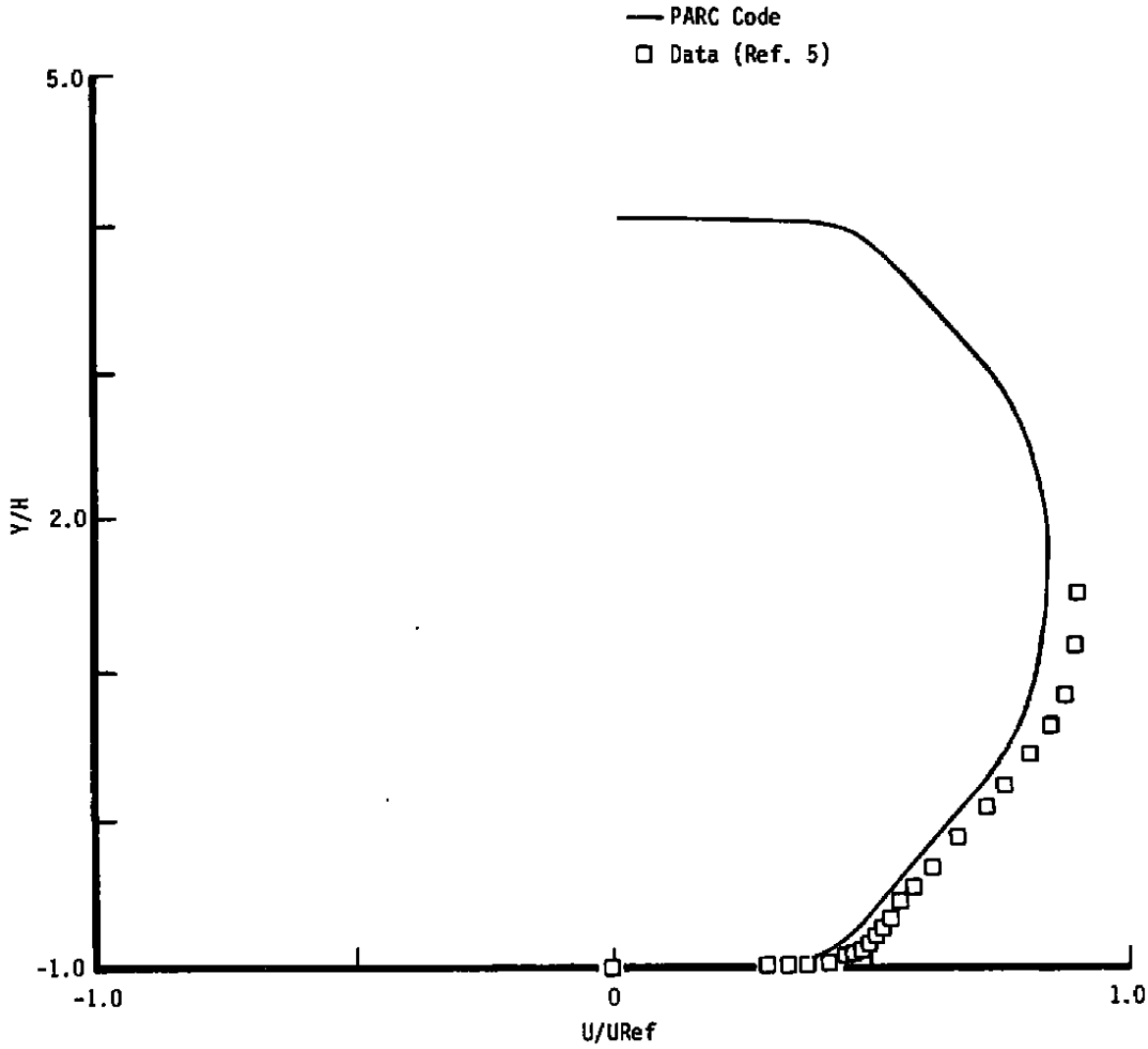

e. X/H = 17.53

Figure 26. Concluded.

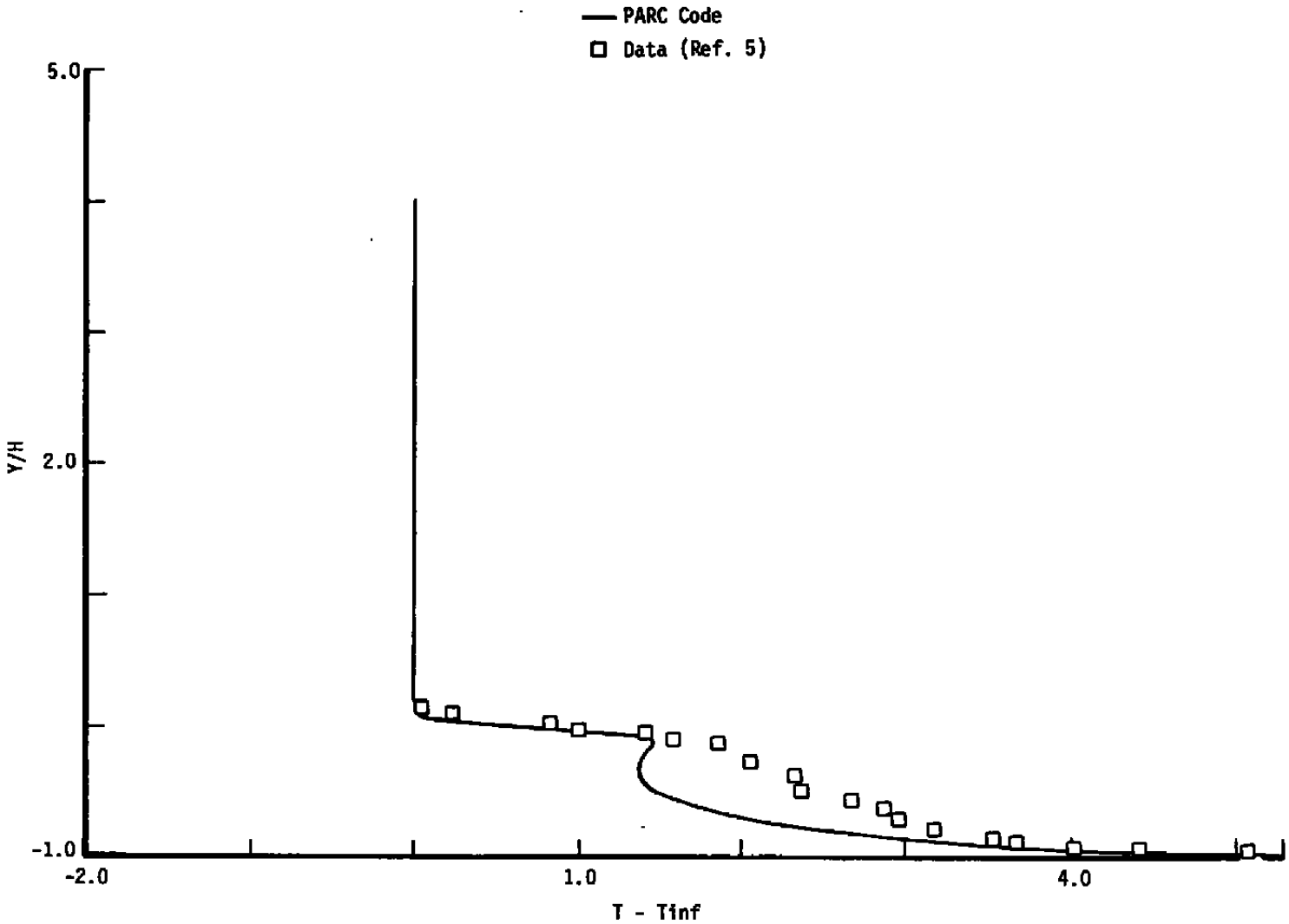

a. X/H = 0.33 (X/H = 0 at step)

Figure 27. Temperature profile comparisons for backstep flow.

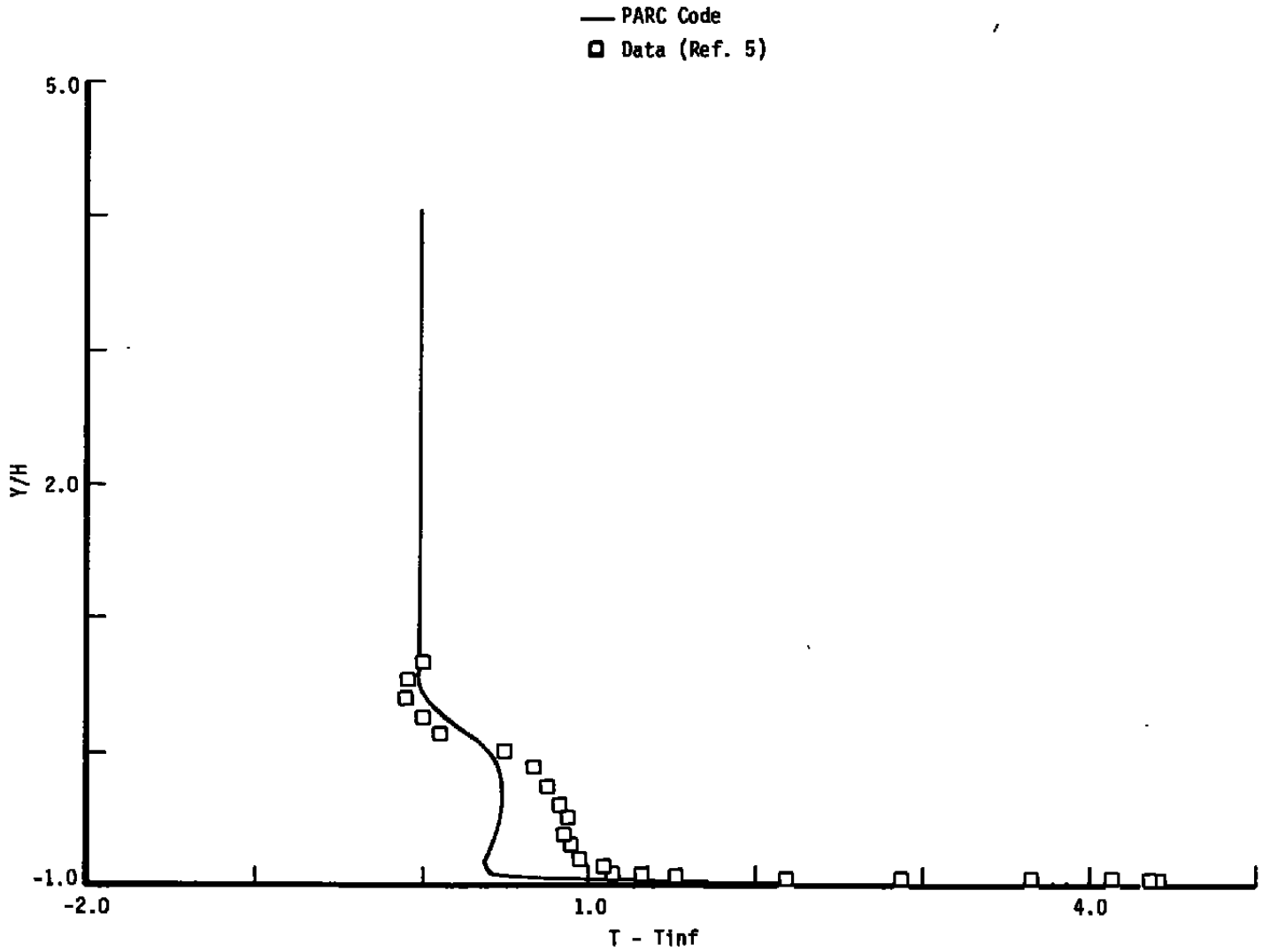

b. X/H = 3.0

Figure 27. Continued.

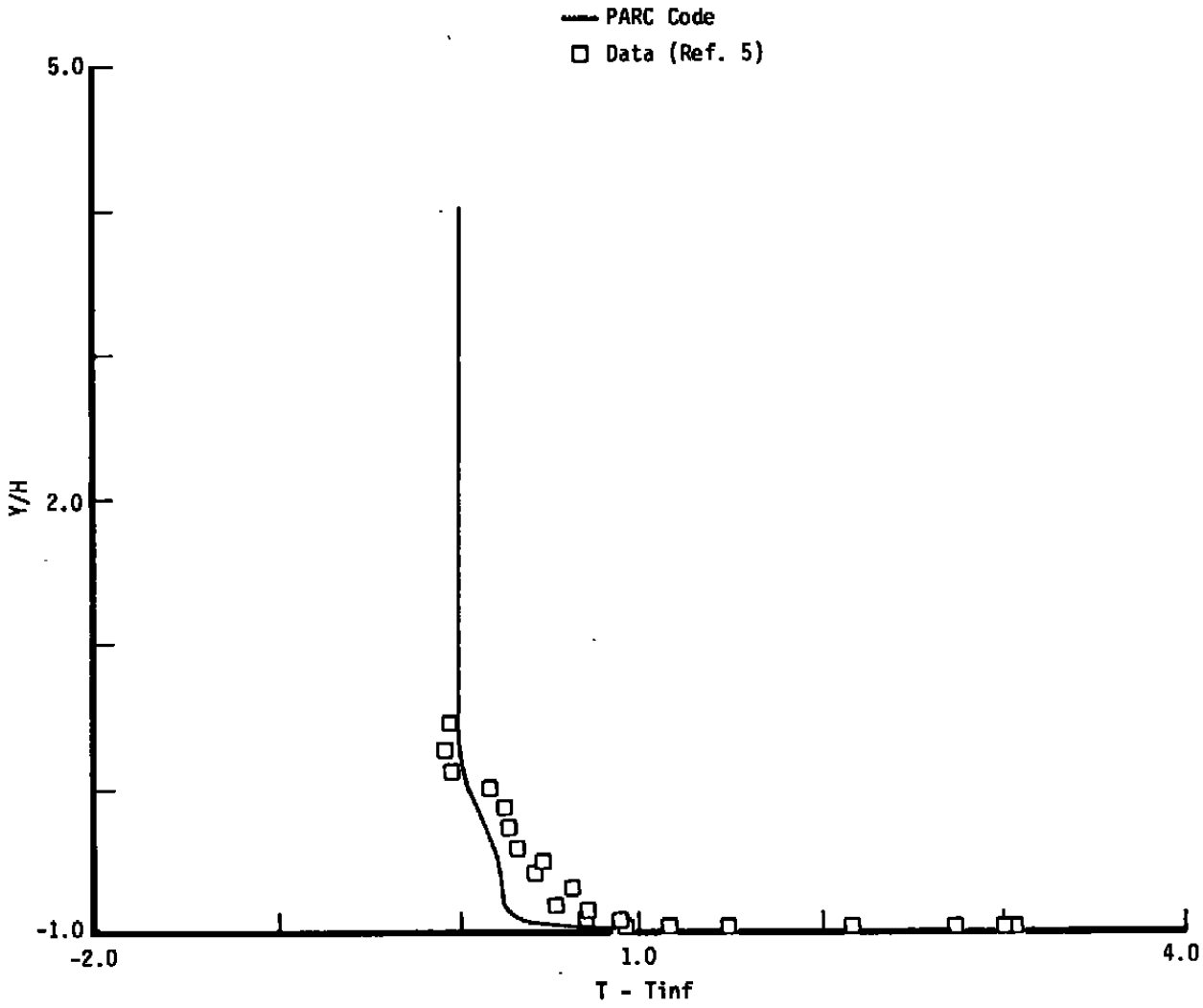

c. X/H = 7.0

Figure 27. Continued.

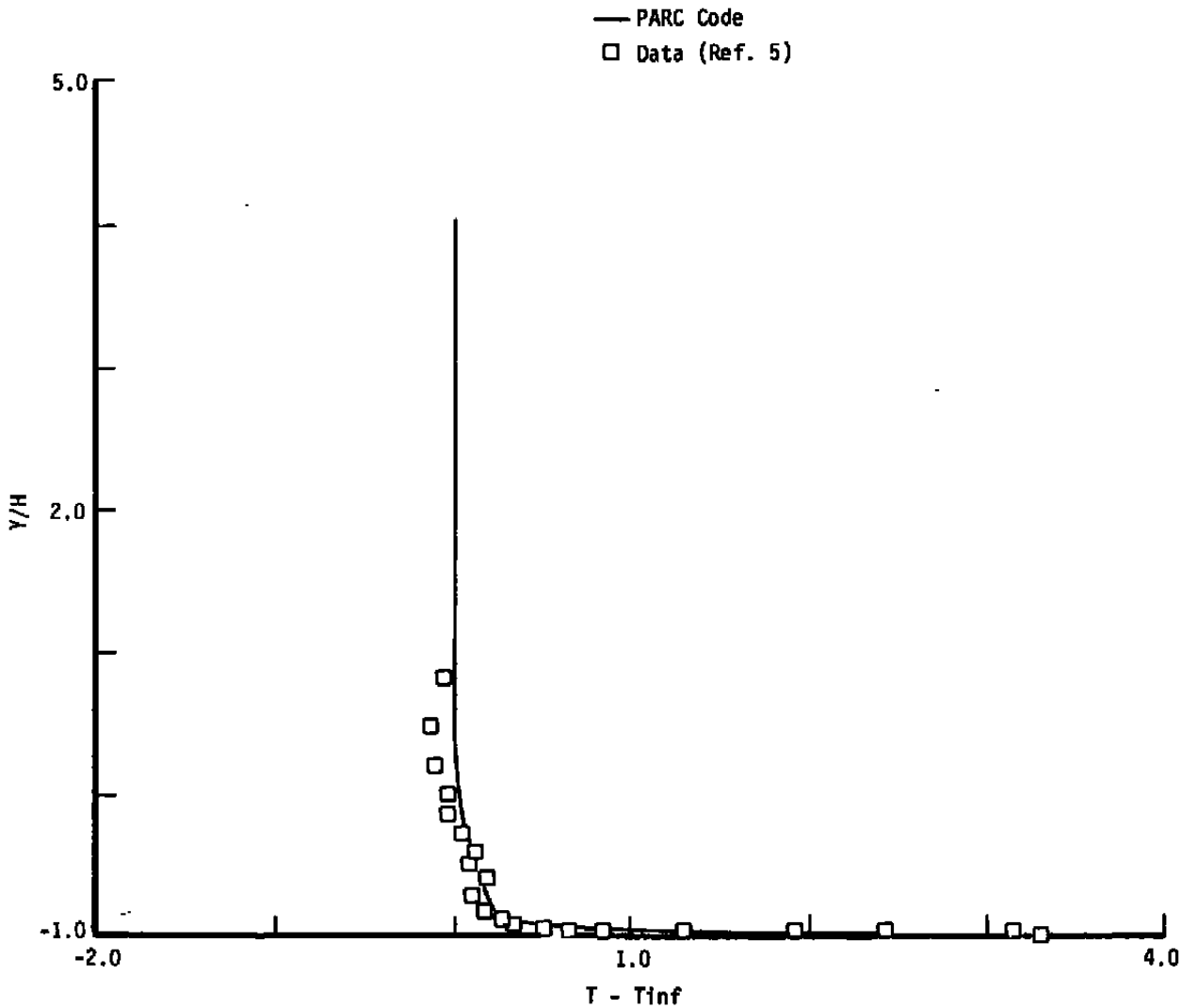

d. X/H = 11.66

Figure 27. Continued.

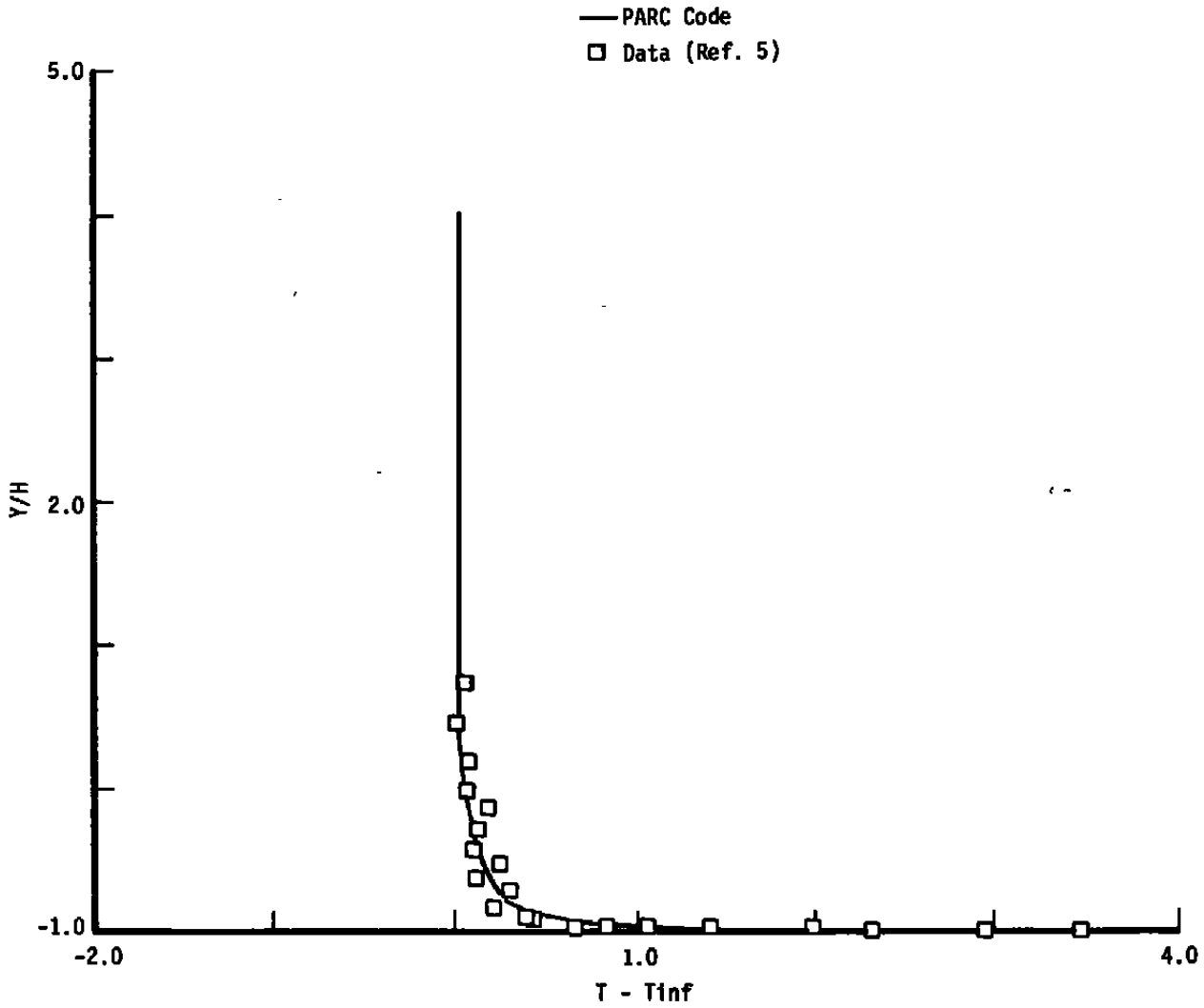

e. X/H = 15.0

Figure 27. Concluded.

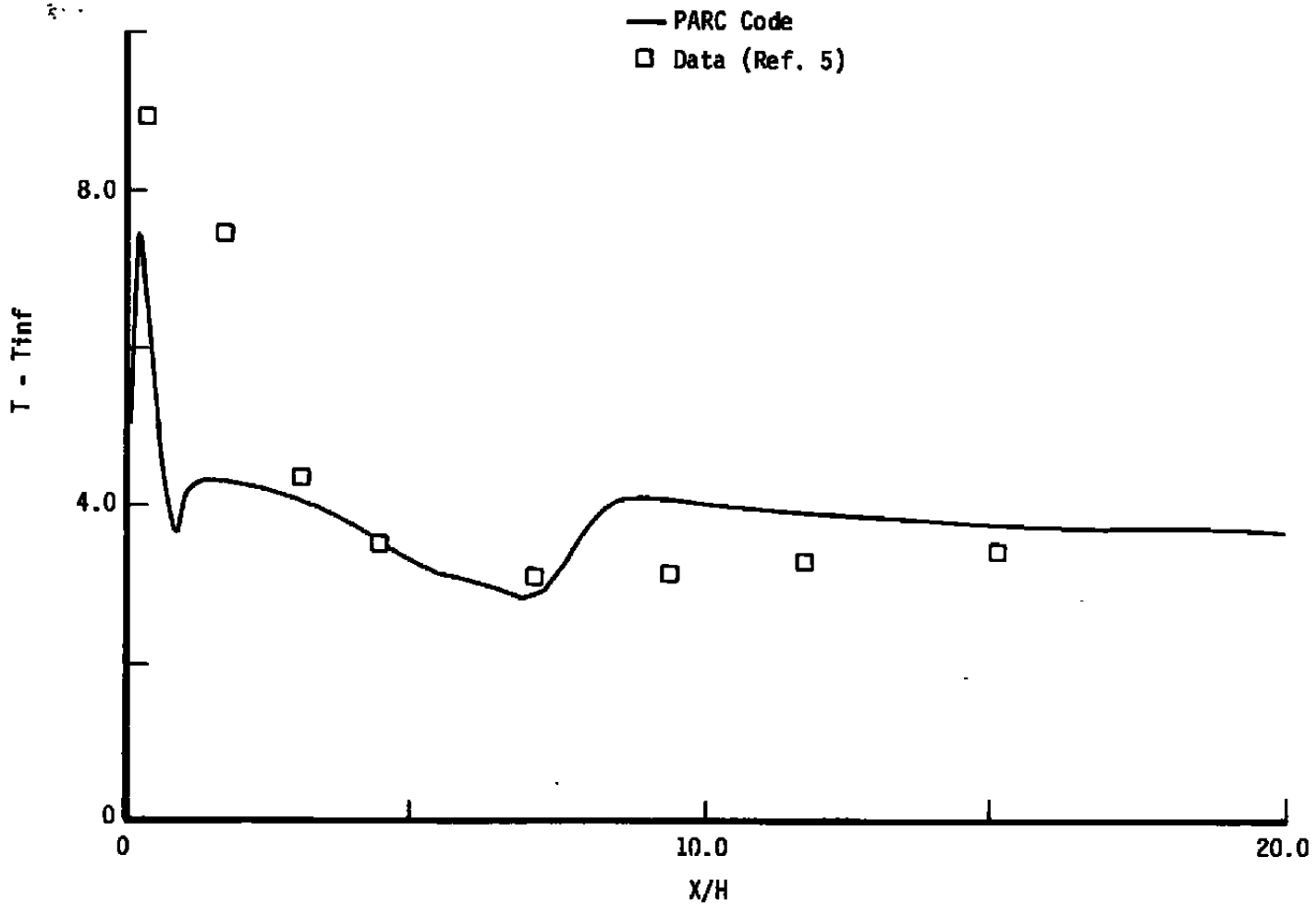

Figure 28. Wall temperature axial variation for backstep flow.

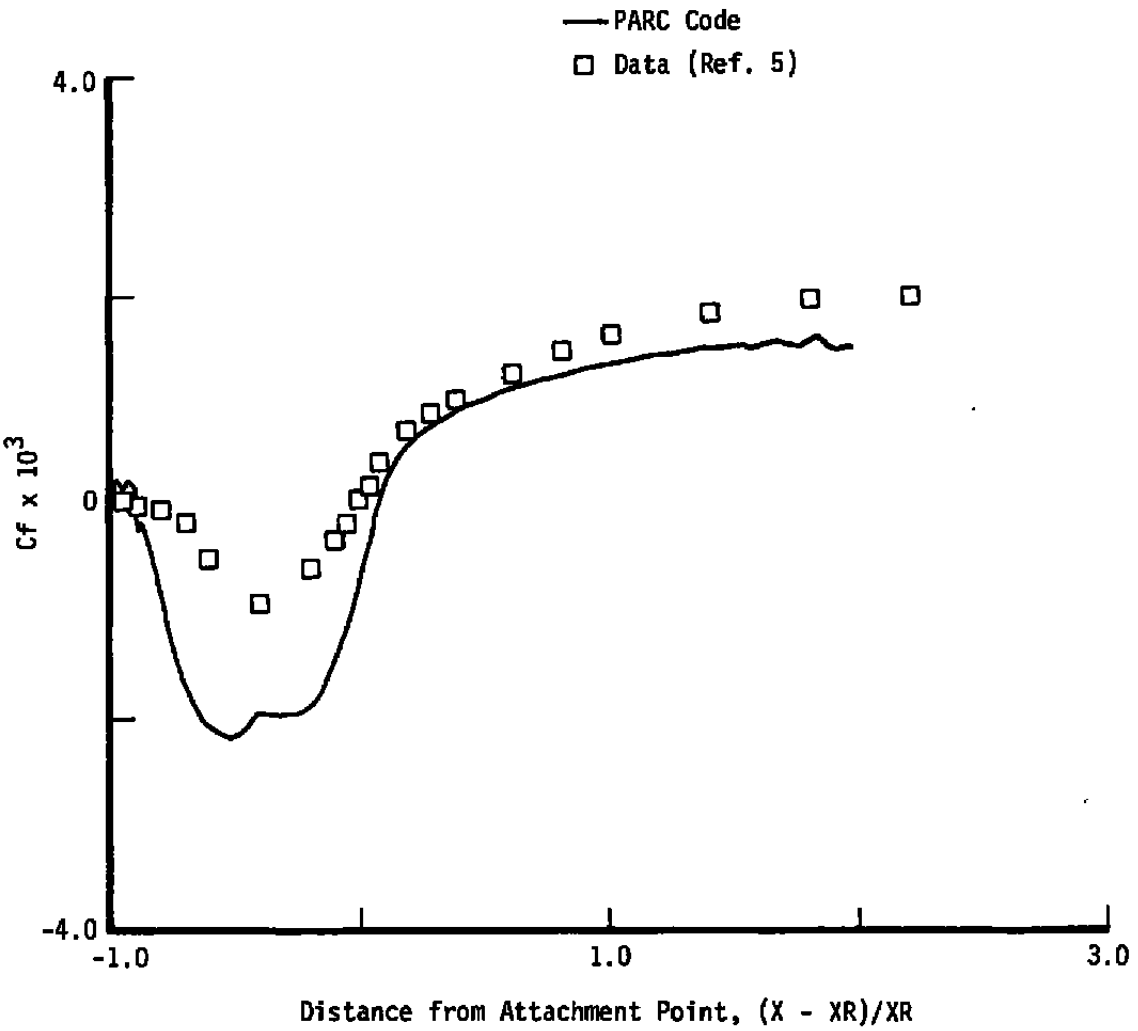

Figure 29. Skin friction axial variation for backstep flow.

Table 1. Flat-Plate Test Case Matrix for Laminar Flow

Test Case	1	2	3	4	5	6	7	8
Flow Properties								
Mach Number	0.75	0.75	0.75	0.75	0.75	0.75	0.1	2.5
Inflow Rex	50,000	50,000	50,000	50,000	50,000	50,000	50,000	50,000
Outflow Rex	200,000	200,000	200,000	200,000	200,00	200,000	200,000	200,000
Thermal, Tw/Te	Adiabatic	Adiabatic	Adiabatic	Adiabatic	Adiabatic	0.5	Adiabatic	Adiabatic
Grid Properties								
Deta	0.1065	0.1065	0.1065	0.03367	0.213	0.1065	0.1065	0.1065
alpha	1.04	1.04	1.04	1.03	1.096	1.04	1.04	1.04
Maximum. eta	35.67	35.67	35.67	35.67	39.5	35.67	35.67	35.67
Points in Boundary Layer	22	22	22	50	12	22	22	22
Total Points	69	69	69	119	33	69	69	69
Streamwise Spacing, Dx	0.005	0.01	0.025	0.01	0.01	0.01	0.01	0.01
Total Points	151	76	31	76	76	76	76	76

Table 2. Flat-Plate Test Case Matrix for Turbulent Flow

Test Case	9	10	11	12	13	14	15	16	17
Flow Properties									
Mach Number	0.75	0.75	0.75	0.75	0.75	0.75	0.75	0.1	2.5
Inflow Rex	2,500,000	2,500,000	2,500,000	2,500,000	2,500,000	2,500,000	2,500,000	2,500,000	2,500,000
Outflow Rex	5,000,000	5,000,000	5,000,000	5,000,000	5,000,000	5,000,000	5,000,000	5,000,000	5,000,000
Thermal, Tw/Te	Adiabatic	Adiabatic	Adiabatic	Adiabatic	Adiabatic	0.5	2.0	Adiabatic	Adiabatic
Grid Properties									
Deta	0.011	0.011	0.011	0.00348	0.022	0.022	0.022	0.022	0.022
alpha	1.138	1.138	1.138	1.07134	1.28845	1.138	1.138	1.28845	1.28845
Maximum eta	250	250	250	250	250	250	250	250	250
Points in Boundary Layer	45	45	45	90	24	45	45	24	24
Total Points	63	63	63	125	33	63	63	33	33
Streamwise Spacing, Dx	0.01	0.025	0.05	0.025	0.025	0.025	0.025	0.025	0.025
Total Points	51	21	11	21	21	21	21	21	21

APPENDIX A

NEW ARTIFICIAL VISCOSITY MODEL

The new artificial viscosity model that was used in this validation effort is basically the same as the old model, except for the details of the formulation of the coefficients.

$$\nabla_\xi\left[C_\xi\left(\epsilon_\xi^{(2)}\Delta_\xi - \epsilon_\xi^{(4)}\Delta_\xi\nabla_\xi\Delta_\xi\right)\right](J\hat{Q}) + \nabla_\eta\left[C_\eta\left(\epsilon_\eta^{(2)}\Delta_\eta - \epsilon_\eta^{(4)}\Delta_\eta\nabla\,\Delta_\eta\right)\right](J\hat{Q})$$

where the forward and backward difference operators are

$$\Delta_\xi Q = Q(\xi+1,\eta) - Q(\xi,\eta) \qquad \Delta_\eta Q = Q(\xi,\eta+1) - Q(\xi,\eta)$$
$$\nabla_\xi Q = Q(\xi,\eta) - Q(\xi-1,\eta) \qquad \nabla_\eta Q = Q(\xi,\eta) - Q(\xi,\eta-1)$$

with the obvious extension to 3-D. The nonlinear coefficients are given by

$$C_\xi = \mu_\xi\left[\frac{1}{J}\left(\left|U\right| + a\sqrt{\xi_x^2 + \xi_y^2 + \xi_z^2}\right)\right] \qquad C_\eta = \mu_\eta\left[\frac{1}{J}\left(\left|V\right| + a\sqrt{\eta_x^2 + \eta_y^2 + \eta_z^2}\right)\right]$$

where the average operators are

$$\mu_\xi Q = Q(\xi+1,\eta) + Q(\xi,\eta) \qquad \mu_\eta Q = Q(\xi,\eta+1) + Q(\xi,\eta)$$

The second- and fourth-order coefficients are defined as

$$\epsilon_\xi^{(2)} = K_2\Delta t f_\xi$$

$$\epsilon_\xi^{(4)} = \text{Max}\,[0,\ K_4\Delta t - \epsilon_\xi^{(2)}]$$

and the "switch" function "f" has the basic form

$$f_\xi = \text{Max}\left[g_\xi(\xi+1,\eta),\ g_\xi(\xi,\eta)\right]$$

where

$$g_\xi = \left|P(\xi+1,\eta) - 2P(\xi,\eta) + P(\xi-1,\eta)\right| \Big/ \left|P(\xi+1,\eta) + 2P(\xi,\eta) + P(\xi-1,\eta)\right|$$

with analogous formulas for the η coefficients.

In the previous equations, all quantities are nondimensional and

U = $\xi_x u + \xi_y v$

V = $\eta_x u + \eta_y v$

u = x-velocity component

v = y-velocity component

a = speed of sound

P = pressure

$\hat{Q}$ = conservation variable (e.g., ρ/J)

J = Jacobian of coordinate transformation

Δt = time-step size

K_2, K_4 = fixed coefficients (i.e. DIS2 and DIS4)

APPENDIX B

NEW ALGEBRAIC TURBULENCE MODEL

The new algebraic turbulence model that was used in this validation effort is basically the same as the old model except that the wall-bounded flow formulation is a purer implementation of the Baldwin and Lomax turbulence model. The wall-bounded part of the algorithm is applied near no-slip boundary surfaces and replaces the unbounded flow values with bounded flow values of the turbulent viscosity between the boundary and the edge of the boundary layer.

$$\mu_T = \mathrm{Re}\ \varrho\ \ell\ V$$

$$V = \ell\ \omega$$

$$\ell = \mathrm{Min}\ (l_i, l_o)$$

$$\ell_i = \frac{\mu_w}{\mathrm{Re}} \frac{1}{\varrho_w u_\tau} \sqrt{\bar{\mu}_T\ (\bar{\mu}_T + \mu/\mu_w)} \qquad \ell_o = C_{Mix}\ (Y_{Max}/Y_{ref})$$

$$\bar{\mu}_T = K\ e^{-KB} \sqrt{\varrho/\varrho_w}\ [e^{\bar{u}} - 1 - \bar{u} - \frac{1}{2}\bar{u}^2 - \frac{1}{6}\bar{u}^3] \qquad Y_{Max} = \text{Y at point where F = } F_{Max}$$

$$\bar{u} = K\ u/u_\tau \qquad F = Y\omega$$

$$u_\tau = \sqrt{\mu_w \omega_w / \varrho_w}$$

Where all quantities are nondimensional and

ω = vorticity

μ = viscous coefficient

Re = PARC Reynolds number

u = velocity component tangent to wall

ϱ = density

Y = distance from wall

Subscripts

w = evaluated at wall

T = turbulent parameter

Constant:

$K = 0.41$, $B = 5.0$, $C_{Mix} = 0.09$, $Y_{ref} = 0.64577$

NOMENCLATURE

Cf	Skin friction coefficient, $\tau_w/(1/2\ \varrho_e U_e^2)$
H	Shape factor (ratio of displacement thickness to momentum thickness)
L	Flat-plate length from leading edge
M	Mach number
Rne	Nozzle exit radius
St	Stanton number
Te	Static temperature at outer edge of boundary layer
Tinf	Reference static temperature for backward-facing step
Tw	Wall temperature
U	Velocity component tangent to the wall
Ucl	Centerline velocity at a given axial location downstream from the free-jet nozzle
Ue	Velocity component tangent to the wall at the outer edge of boundary layer
Utau	Friction velocity, $\sqrt{\tau_w/\varrho_w}$
U+	Ratio of tangential velocity to friction velocity
X	Coordinate along body surface or axial length
Y	Coordinate normal to body surface or radial length
Y+	Reynolds number based on wall properties, friction velocity and distance from the wall
τ_w	Wall shear stress, $\mu_w \frac{\partial U}{\partial Y}\Big\|_w$
ϱ_w	Density at wall
μ_w	Molecular viscosity at wall